

REPORT DOCUMENTATION PAGE			Form Approved OMB No. 0704-0188		
Public reporting burden for this collection of information is estimated to average 1 hour per response, including the time for reviewing instructions, searching existing data sources, gathering and maintaining the data needed, and completing and reviewing this collection of information. Send comments regarding this burden estimate or any other aspect of this collection of information, including suggestions for reducing this burden to Department of Defense, Washington Headquarters Services, Directorate for Information Operations and Reports (0704-0188), 1215 Jefferson Davis Highway, Suite 1204, Arlington, VA 22202-4302. Respondents should be aware that notwithstanding any other provision of law, no person shall be subject to any penalty for failing to comply with a collection of information if it does not display a currently valid OMB control number. <b>PLEASE DO NOT RETURN YOUR FORM TO THE ABOVE ADDRESS.</b>					
1. REPORT DATE (DD-MM-YYYY) 10-08-2012		2. REPORT TYPE Final		3. DATES COVERED (From - To) 1/6/2009 to 05/31/2012	
4. TITLE AND SUBTITLE (DCT) A RECONFIGURABLE RF PHOTONICS UNIT CELL FOR INTEGRATED CIRCUITS			5a. CONTRACT NUMBER FA9550-09-1-0490		
			5b. GRANT NUMBER FA9550-09-1-0490		
			5c. PROGRAM ELEMENT NUMBER		
6. AUTHOR(S) Christos Christodoulou			5d. PROJECT NUMBER		
			5e. TASK NUMBER		
			5f. WORK UNIT NUMBER		
7. PERFORMING ORGANIZATION NAME(S) AND ADDRESS(ES) University of New Mexico			8. PERFORMING ORGANIZATION REPORT NUMBER		
9. SPONSORING / MONITORING AGENCY NAME(S) AND ADDRESS(ES) AFOSR/RSE 875 N Randolph St Arlington, VA 22203			10. SPONSOR/MONITOR'S ACRONYM(S)		
			11. SPONSOR/MONITOR'S REPORT NUMBER(S) AFRL-OSR-VA-TR-2012-1195		
12. DISTRIBUTION / AVAILABILITY STATEMENT Distribution A: Approved for Public Release					
13. SUPPLEMENTARY NOTES					
14. ABSTRACT <p>In this work, the integration of a Quantum Dot Mode Locked Laser, that acts as a microwave and millimeter wave source, with a wideband antenna is presented. Two aspects of research are discussed. The first aspect deals with a Mode Locked Laser (MLL) based on quantum dot (QD) materials. Due to the unique properties of the QDs, the QDMLL can expand the range of stable mode-locking operation. The details of the MLL structure and its operation mechanism are discussed by experimenting on a two-section QDMLL.</p> <p>The second aspect of this work is the realization of a compact transmitting antenna integrated to a QDMLL. For this purpose, several antenna prototypes were designed by using the two-port microwave approach. The designed antennas were integrated with laser chips using the lithographic method. The challenges of designing this wideband antenna that can operate at multiple QDMLL harmonics are presented in detail. Moreover, an example of achieving beam-steering using a two-element QDMLL-LTSA phased array by manipulating the laser bias condition is also discussed. The proposed RF/Photonic antenna is a good candidate in realizing a compact phased antenna array system without the use of phase shifters.</p>					
15. SUBJECT TERMS Reconfigurable, Quantum Dot Mode Locked Lasers, antennas, RF/Photonics					
16. SECURITY CLASSIFICATION OF:			17. LIMITATION OF ABSTRACT	18. NUMBER OF PAGES	19a. NAME OF RESPONSIBLE PERSON
a. REPORT	b. ABSTRACT	c. THIS PAGE			19b. TELEPHONE NUMBER (include area code)



THE UNIVERSITY of  
NEW MEXICO SCHOOL of ENGINEERING

*Department of Electrical & Computer Engineering*

# **“(DCT) A RECONFIGURABLE RF PHOTONICS UNIT CELL FOR INTEGRATED CIRCUITS”**

**Final Technical Report**  
**Contract/Grant #: FA9550-09-1-0490**

**1 June 2009 – 31 May 2012**

**10 August 2012**

**Submitted by:**

Christos Christodoulou— Principal Investigator and Professor  
Department of Electrical and Computer Engineering  
University of New Mexico  
Albuquerque, NM 87131  
Tel. (505) 277-6580  
Fax: (505) 277-1439  
e-mail: [christos@ece.unm.edu](mailto:christos@ece.unm.edu)

# TABLE OF CONTENTS

<b>TABLE OF CONTENTS .....</b>	<b>2</b>
<b>1. Introduction.....</b>	<b>4</b>
1.1 Quantum Dots .....	5
1.2 Mode locking technique.....	8
1.3 Laser-integrated antenna .....	9
<b>2. Quantum Dot Passively Mode-locked Laser .....</b>	<b>11</b>
2.1 Background .....	11
2.2 Device Structure.....	11
2.3 QDMLL Processing .....	12
2.4 Device characterization.....	13
2.5 Reconfigurable microwave pulse generator.....	19
2.6 Emission measurement of the QDMLL integrated bow-tie antenna .....	21
<b>3. Antennas for Hybrid Integration with a QDMLL.....</b>	<b>22</b>
3.1 Antenna Design.....	22
3.2 Two-port simulation technique into an antenna design .....	26
3.3 Fabrication process and hybrid integration with a QDMLL.....	30
3.4 Characterization of the QDMLL-integrated-Antenna.....	31
3.5 Pattern estimation of a microstrip antenna integrated with QDMLL .....	34
3.6 Summary .....	38
<b>4. Integration with a Bowtie Slot Antenna at 10 and 20 GHz and Antenna Array Beam steering by Biasing the QDMLL.....</b>	<b>39</b>
4.1 Multi-resonance bow-tie slot antenna .....	39
4.2 Antenna fabrication and measurement.....	45
4.3 Impedance Matching.....	47
4.4 Tapered slot antenna (TSA) design using the ideal transmission line .....	52
4.5 Tapered slot antenna (TSA) with biasing lines.....	57
4.6 2 Element TSA array.....	60
4.7 Beam-steering experiment .....	62
4.8 Summary .....	65
<b>5. Conclusions and Future work.....</b>	<b>66</b>
5.1 Summary and Conclusions.....	66
5.2 Future work and recommendation .....	67
<b>References.....</b>	<b>69</b>
<b>6. Personel, Publications, Interactions, .....</b>	<b>72</b>
Personell.....	72
Publications .....	72
Interactions.....	73
Recognition .....	74
New Discoveries, Inentions, Patents.....	74
<b>7. Appendix A (Selected publications) .....</b>	<b>75</b>
I. Characterization of timing jitter in a 5 GHz quantum dot passively mode-locked laser .....	75
II. Microwave characterization and stabilization of timing jitter in a quantum dot .....	

passively mode-locked laser via external optical feedback .....	81
---	----



## 1. Introduction

Research in higher frequency is reaching the terahertz domain as the speed of microprocessors using electrical clock distribution increases. However, current microelectronic technology is limited by the copper interconnects used because the resistive and associated power loss increase as the size of a device becomes compact. In addition to that, the available power from solid state devices decreases as the operating frequency increases. In order to resolve these limitations, optical interconnects and semiconductor mode-locked Lasers (MLLs) are suggested as an ideal source for the ultra-short optical pulse generation. Compared to other competing approaches such as the heterodyning technique of two lasers [1-2], this method is able to obtain higher optical-to-electrical conversion efficiency. Additionally, due to this technique, stabilization of the generated frequency is easier by removing the uncorrelated phase noise [3]. Therefore, the pulsed mm-wave generation using MLLs has attracted interest for various applications e.g. optical clock recovery, optical time multiplexing and switching [4-7].

We start with an array of quantum dot diode cells configured to emit mode-locked laser pulses. By manipulating the biasing of the saturable absorber (SA) section of a quantum dot mode-locked laser (QDMLL), the resonance frequency generation can be controlled. The optically generated microwave signals are then transported to broad-band lithographic antennas. Thus the MLLs-integrated-active antennas are accomplished. The resonance frequency of the proposed antennas is determined by the repetition rate of the MLL. When the saturable absorber of the MLL is reversely biased, longitudinal modes in the laser cavity are synchronized and the light becomes pulsed emission. Its repetition rate is determined by cavity round-trip time which is determined by  $f_R = c/2nL$ . Here  $c$  is the speed of light,  $n$  is the group index of refraction,  $L$  is the cavity length and  $f_R$  is the repetition rate. For this research, the 4.1-mm long QDMLL is used to obtain the hybrid integration with wireless RF modules and its estimated repetition rate can be computed to be 10 GHz.

Of particular interest in many applications are lithographic antennas because of their simple designs and broad-band impedance characteristics. Various prototypes of broad band antennas are designed and integrated with a QDMLL.

The measured results indicate that the proposed QDMLL is an excellent candidate for the compact microwave source. The repetition rate of a single MLL can be tuned by changing the locations of the applied voltage bias.

This research report contains the description of the basic building blocks :

- A reconfigurable Quantum Dot (QD)
- A reconfigurable antenna (RF sensor)
- The integration of the RF/Quantum Dot circuit.
- Other reconfigurable or distributed array configurations

## 1.1 Quantum Dots

Quantum dot (QD) materials are unique, due to their ultra-broad bandwidth, ultra-fast gain dynamics, and easily saturated gain and absorption, which make them an ideal choice for monolithic semiconductor MLLs [4]. These characteristics give MLLs the advantage of stability over a wider power range compared to the standard quantum well (QW). With this increased range of operation, higher microwave power can be extracted from the device with lower phase noise [3].

In our research, a two-section passive QDMLL in 4.1 mm length demonstrated higher optical-to-electrical conversion efficiency than the optical heterodyning technique of two lasers [8]. By comparing the density states for bulk, quantum well (QW), quantum wire (QWire) and quantum dot (QD), new properties of QDs are described. Figure 1.1 shows the state density for different materials [9]. The bulk material is a 0-dimension of confinement. Its state density is continuous and proportionally related to the square root of the energy. Compared to the bulk, the state density in QWs (1-dimension) decays so that its density forms a step function. In 2-dimensions, the density of the quantum wire's state further decreases compared to the QWs. Finally, the state density in QDs (3-dimensions) is a  $\delta$ -function in energy. Although the state density of the real QD-materials has a line expansion resulted from fluctuations in the quantum dot sizes, the state density is still attenuated compared to the quantum wire. By taking advantage of the small size of QDs, the fundamental benefits of QD-lasers are an ultra-low threshold current, temperature-insensitive

operation, high material gain and differential gain, a decreased line width enhancement factor, an ultra-broad bandwidth, easily saturated gain and absorption, and a larger tuning range of the lasing wavelength. The structure of InAs on GaAs Quantum Dots is shown in Figure 1.2.

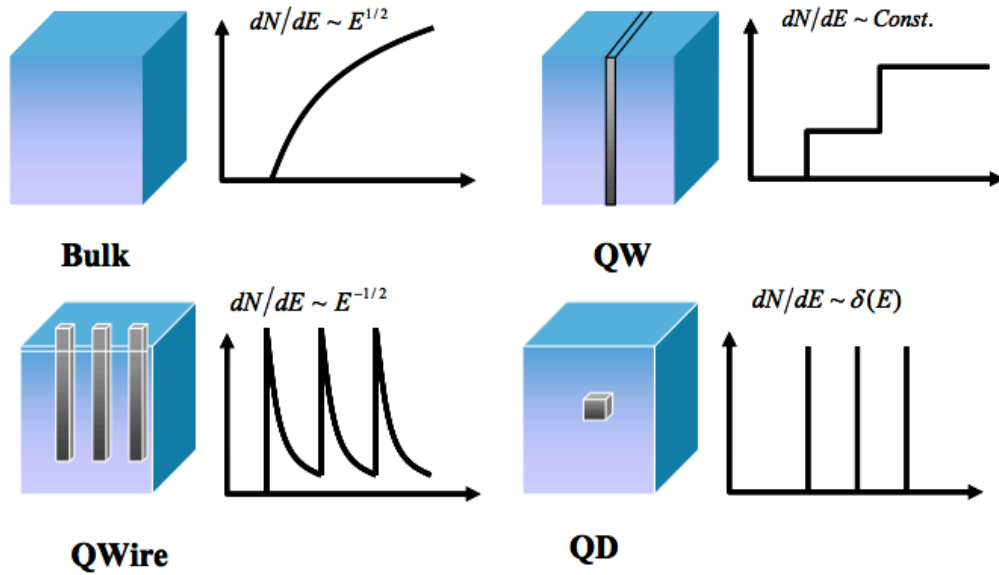


Figure 1.1 Density of state functions for bulk, quantum well, quantum wire and quantum dot

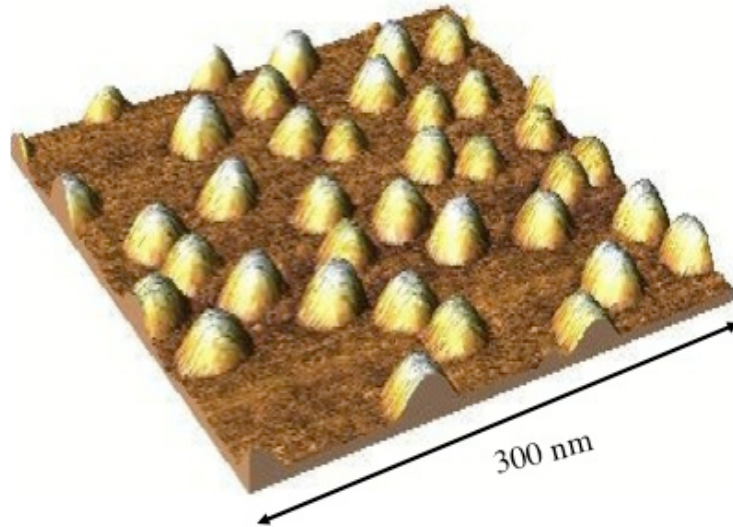


Figure 1.2 The structure of InAs on GaAs Quantum Dots

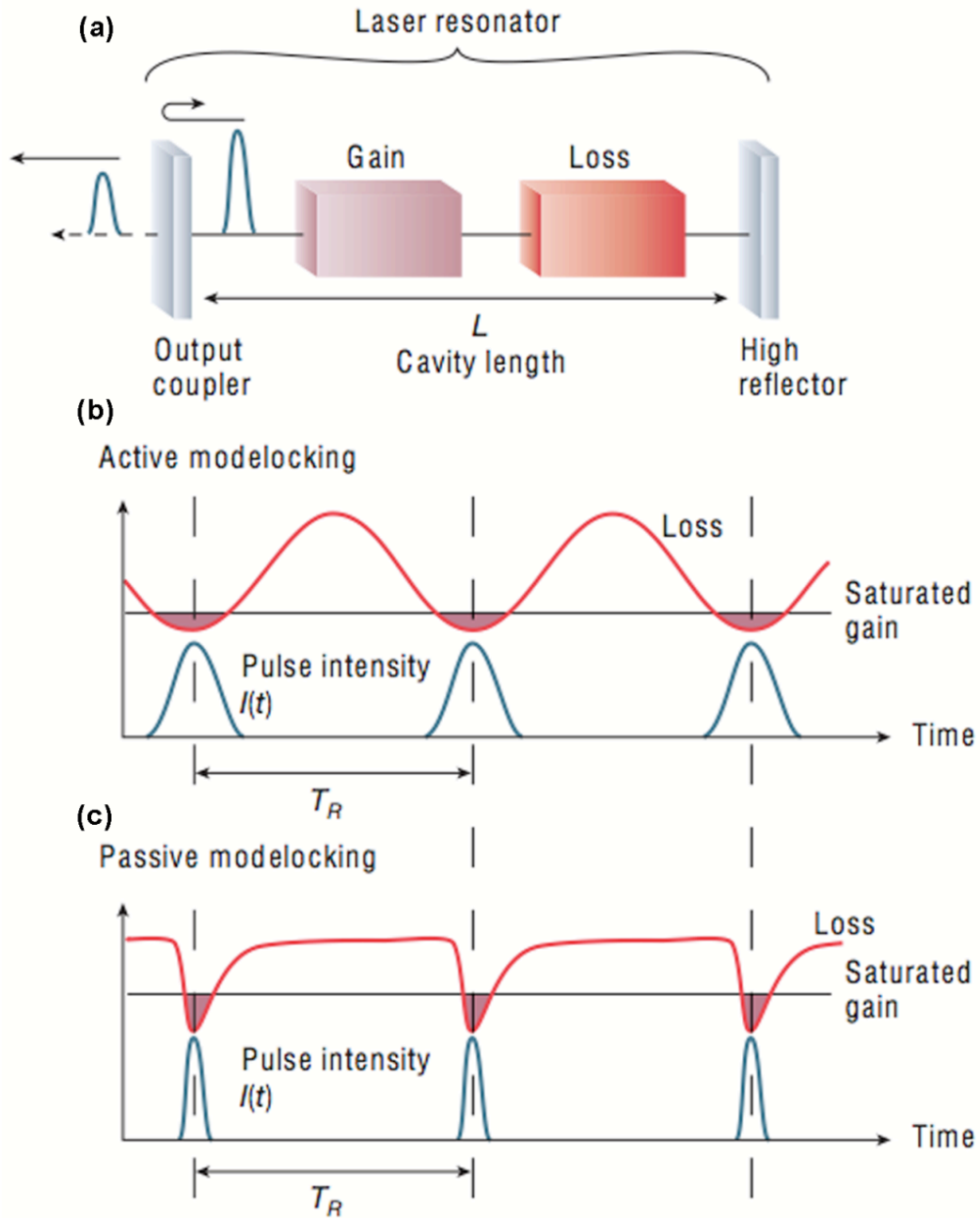


Figure 1.3 (a) A simplified concept of a mode-locked laser resonator. (b) The pulse generation of an actively mode-locked laser. (c) The pulse generation of a passively mode-locked laser with a fast saturable absorber [9].

## 1.2 Mode locking technique

The mode-locking technique is a method of generating ultrashort pulses from lasers. The mode-locked laser (MLL) consists of a gain and a saturable absorber which is a nonlinear passive element [10]. Due to the nonlinear effects of absorbers in MLLs, the formation of ultrashort pulses circulating in the laser cavity is possible. When it is in the steady state condition, the various effects influencing the circulating pulse are in a balance so that the pulse parameters are unchanged after each completed round trip. Every time the pulse inside the laser cavity hits the output coupler's mirror, a pulse is emitted. As previously mentioned in section 1.1, the pulse repetition rate corresponds to the resonator round-trip time. Because of the fast recovery time of the absorber, the pulse can be trimmed to a very short pulse width of picoseconds order. In this way, the peak power of the MLL can be much higher than the average power.

MLLs can be either actively or passively mode locked. The active mode locking approach uses an external signal in order to induce a modulation of the light inside the cavity. If the modulation is synchronized with the resonator round trips, ultrashort pulses are generated. The passive mode locking method uses the nonlinear passive element to form an ultrashort pulse circulating in the laser cavity. In this research, we used the passive mode locking approach by implementing a saturable absorber causing self-modulation of light. In Figure 1.3, much shorter pulse signals can be obtained by the passive mode-locking approach, compared to the active mode-locking approach. This occurs because a saturable absorber modulates the resonator losses much faster than an electronic modulator.

In conclusion, the result in the frequency domain is given as a phase-locked frequency comb containing a constant mode spacing of the pulse repetition rate. The spectral width of the envelope of this frequency comb is inversely proportional to the pulse duration. Here a 4.1mm long QDMLL device is used. Figure 1.4 depicts the 2-section QDMLL composed of a 3.8-mm long gain-section and a 0.3-mm long SA. The gain and SA are electrically isolated. The details on the passive QDMLL are introduced in Section 2. As an alternative method, the hybrid mode-locked technique is used in which active and passive mode locking are applied at the same time. The key advantage of it is an externally controlled pulse repetition rate.

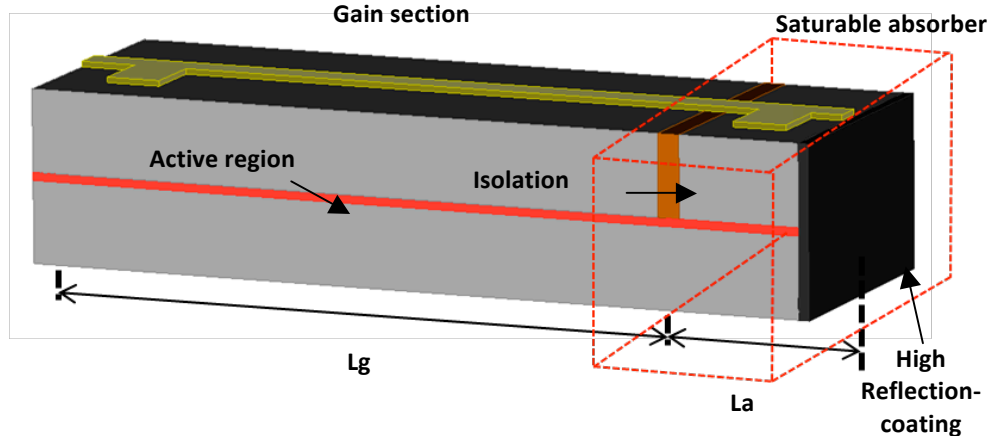


Figure 1.4 A two-section QDMLL

### 1.3 Laser-integrated antenna

To radiate energy from the QDMLL, an antenna must be integrated to it lithographically. Various prototypes of lithographic antennas (see Figure 1.5) were designed and integrated with QDMLLs. First, a bow-tie antenna was tried. The bow-tie antenna was chosen due to its broadband bandwidth and its simplicity of integrating with a laser chip [11]. A semi-insulating GaAs was used as a substrate not only to achieve the monolithic integration with a QDMLL, but also to reduce the undesirable loss induced by mismatches among different materials. The idea of using a QDMLL as a compact microwave source is verified by measuring the estimated emitting power intensity patterns of the QDMLL-integrated-active antenna. For the estimated radiation pattern, a rectangular microstrip antenna was used. By the existence of an infinite ground plane, the microstrip antenna can accommodate the environmental limitation where a metallic sub-mount is required underneath an antenna substrate to operate a QDMLL. We discuss the antenna design and radiation pattern measurement in Section 3.

Since a single QDMLL can produce the multiple harmonics of the fundamental repetition rate, new types of broad band antennas are required to carry out the higher orders of repetition rates out of a QDMLL. To this end, the bow-tie slot antenna was proposed to accommodate the higher repetition rates of a QDMLL so that the MLL can extend its operating range.

Another area for improvement during integration is the introduction of the matching

circuit. As the operating frequency increases, the available power from solid state devices decreases. Therefore, the delivered power using an impedance transformer between the solid state device and an antenna is very critical [12]. Details of impedance matching are discussed in Section 4. The prototype of designed matching circuit is shown in Figure 1.6. The phased array tapered slot antenna integrated with QDMLLs is fabricated to perform beam-steering by manipulating the applied voltage biases. Detail antenna designs and tests are also presented in Section 4.

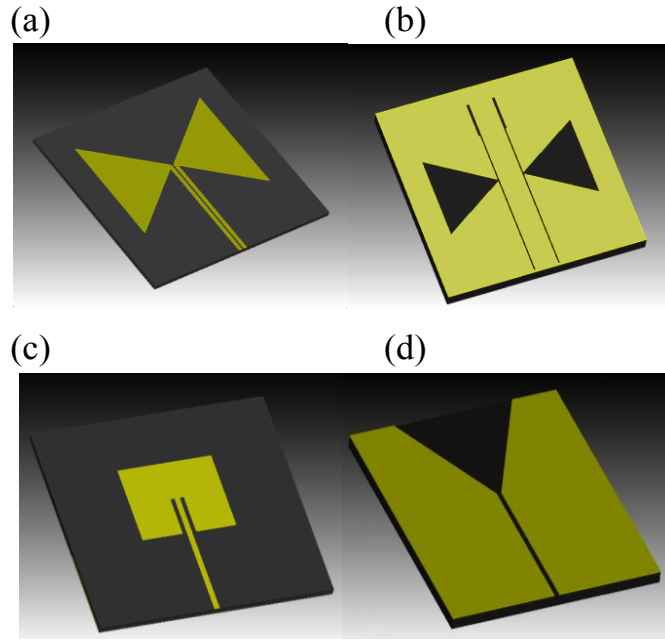


Figure 1.5 The designed prototypes of the lithographic antennas integrated with the QDMLL;  
(a) Bow-tie antenna (b) Bow-tie slot antenna (c) Microstrip patch antenna (d) Tapered slot antenna

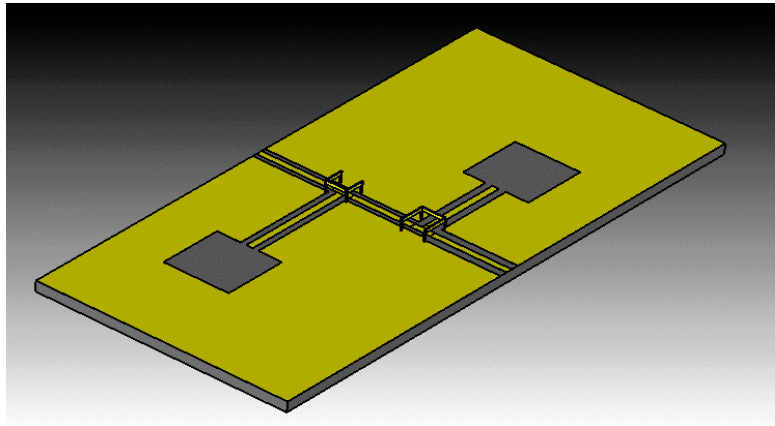


Figure 1.6 A dual frequency impedance matching transformer

## 2. Quantum Dot Passively Mode-locked Laser

### 2.1 Background

Due to the various advantages including its compact size, direct electrical pumping, high electrical-to-optical-to-electrical (E/O/E) conversion efficiency and low power consumption to operate, monolithic passively mode-locked lasers (MLLs) are promising candidates for novel microwave frequency generators [1-4]. Particularly, the unique material properties of quantum dot (QD) materials such as ultra broad bandwidth, ultra fast gain dynamics, and easily saturated gain and absorption, result in an ideal material for MLLs [5,6]. Previously, semiconductor active regions such as quantum wells could produce the same optical gain and absorption functions, but frequently required separate optimization of the optical materials in the MLL cavity. However, for the QDMLL, the same epitaxial structure in both the absorber and gain sections can be used to achieve a more compact design.

### 2.2 Device Structure

The laser epitaxial structure of this device is a multi-stack "Dots-in-a-WELL" (DWELL) structure that is composed of an optimized six-stack QD active region grown by solid-source molecular beam epitaxy (MBE) on a (001) GaAs substrate [7]. The 3.5- $\mu\text{m}$  wide optical ridge-waveguide devices are fabricated with standard multi-section device processing. To achieve the 10 GHz repetition rate of a QDMLL, the two-section QD passively MLLs are made with a total cavity length of 4.1-mm. A highly reflective coating ( $R \approx 95\%$ ) is applied to the mirror facet next to the SA and the other facet is cleaved ( $R \approx 32\%$ ). The scheme of the proposed two-section QDMLL is shown in Figure 2.1. In general, a metal-semiconductor-metal (MSM) detector is applied to convert the optically generated pulse from MLLs to the electrical pulse signal [8]. Basically, the picosecond optical pulse goes into the SA, the leading edge of the optical pulse is absorbed thereby creating free carriers. The applied DC voltage bias results in that electrons and holes are swept to the metal contacts. Thus, the microwave signals can be generated by simply applying DC voltage bias on an absorber. Due to its simpler geometry, it can have the potential to convert the ultrafast optical signal to



electrical pulse more efficiently. The benefits of RF generation from the passive QDMLL compared to competing methods such as optical heterodyning of two continuous-wave single mode lasers are the higher conversion efficiency and easier stabilization of the generated RF frequency. These advantages of the passive QDMLLs are achieved by removing the uncorrelated phase noise and temperature fluctuations.

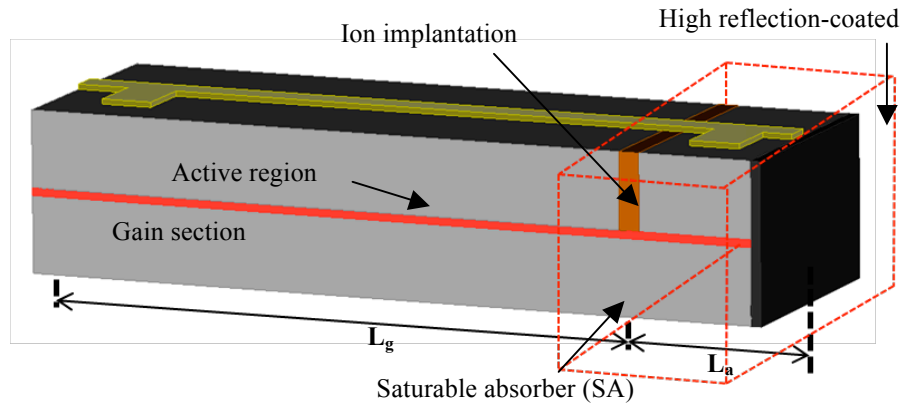


Figure 2.1 Schematic of a 4.1-mm long two section QDMLL

### 2.3 QDMLL Processing

The wafers are processed into two-section devices following standard ridge waveguide laser processing. Wafers were processed to be 3.5- $\mu\text{m}$  wide, deep-etched ridge waveguides with segmented contact sections. The processing is demonstrated as shown in Figure 2.3. The sample was etched to form 3.5- $\mu\text{m}$  wide, 1.8- $\mu\text{m}$  deep ridges by inductively coupled plasma (ICP) etching after the first lithography was applied on the wafer with the ridge-waveguide-mask. Next, standard benzocyclobutene (BCB) processing was applied to achieve isolation between the p-type metal and the etched cladding layer. The segmented-contact mask was used to make photoresist patterns for the p-type metal deposition and ion implantation. The isolation between the adjacent sections is provided by proton implantation. By means of implantation, an isolation resistance is designed that is greater than 10M $\Omega$ . After post processing of the n-type metal deposition on the substrate side of the wafer the sample was annealed at 380°C for 1 minute. A temperature greater than 380°C can crack the BCB. Another Ti/Au metal layer was deposited for the n-side mounting.

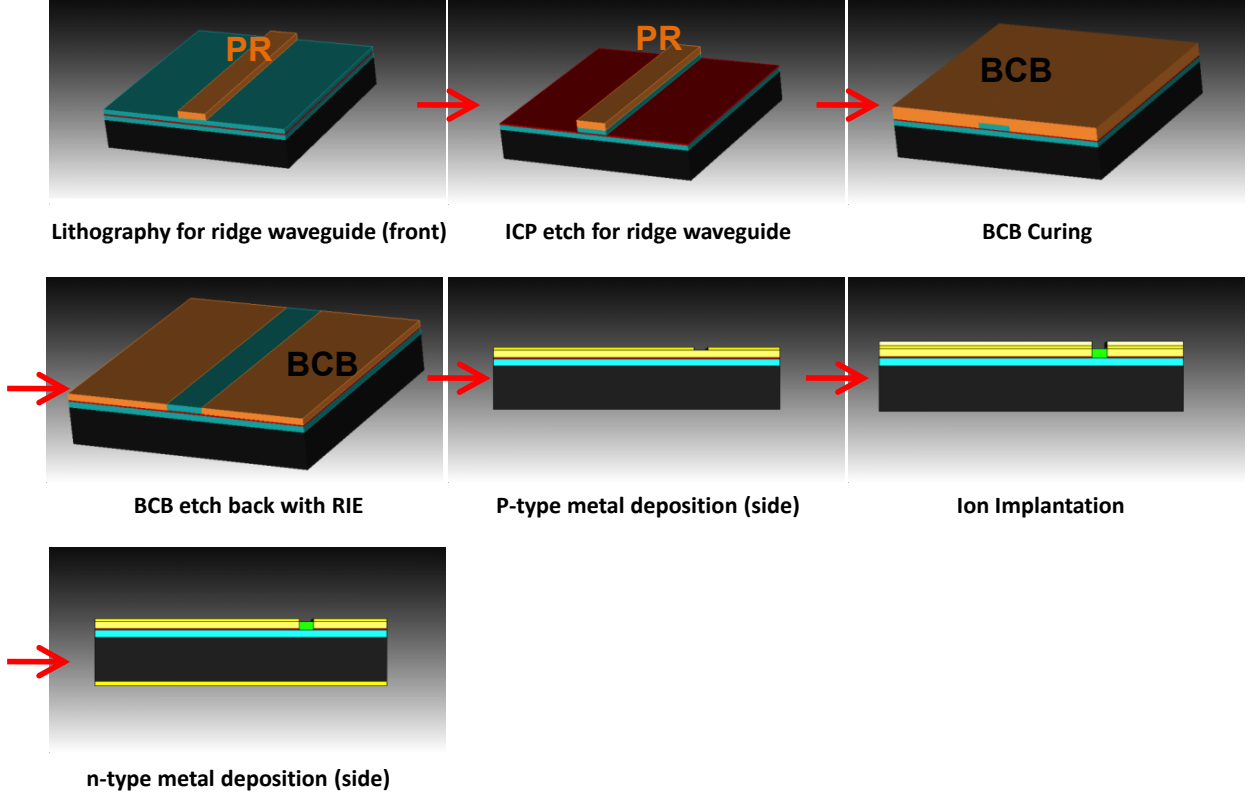


Figure 2.2 Process flow chart

## 2.4 Device characterization

In this section, the characterized results of a two-section QDMLL are presented. In order to suitably apply a QDMLL as a compact microwave frequency source for hybrid integration with antennas, we measured the intensity and phase of photocurrent along the frequencies generated by the QDMLL.

In Figure 2.3, the experimental setup is demonstrated. The two-section laser was mounted on an Aluminum nitride (AlN) substrate and then on copper heat sink for both good thermal conductivity and electrical isolation. The temperature is maintained at 20°C by a thermoelectric cooler (TEC). The optical output of the laser was collected with an optical head, which integrates a lens, an isolator and a short 1-m single-mode polarization maintaining (PM) fiber pigtail, then connected into the Corning SMF-28e fibers followed by a polarization controller. The collected emission was fed into the autocorrelator (Femtochrome FR-103XL Autocorrelator) to measure the pulse width, and the optical spectrum analyzer (Agilent 86142B OSA) to measure the optical spectra through fiber

couplers.

The repetition rate of the electrical pulses out of an absorber was measured by the RF-spectrum analyzer (HP 8563E ESA). We used the 150- $\mu\text{m}$  pitch pico-probe to apply DC-voltage bias on an absorber and simultaneously extract the photocurrent out of a QDMLL. The bias-T circuit is located between the QDMLL and an RF spectrum analyzer. It is composed of a combination of a parallel-inductor and a series-capacitor. Due to the bias-T, the microwave pulse signals from the SA are delivered to the RF spectrum analyzer without affecting the voltage source. A DC voltage can only be applied on the absorber of a QDMLL since the capacitor prevents the DC voltage flowing into the RF spectrum analyzer.

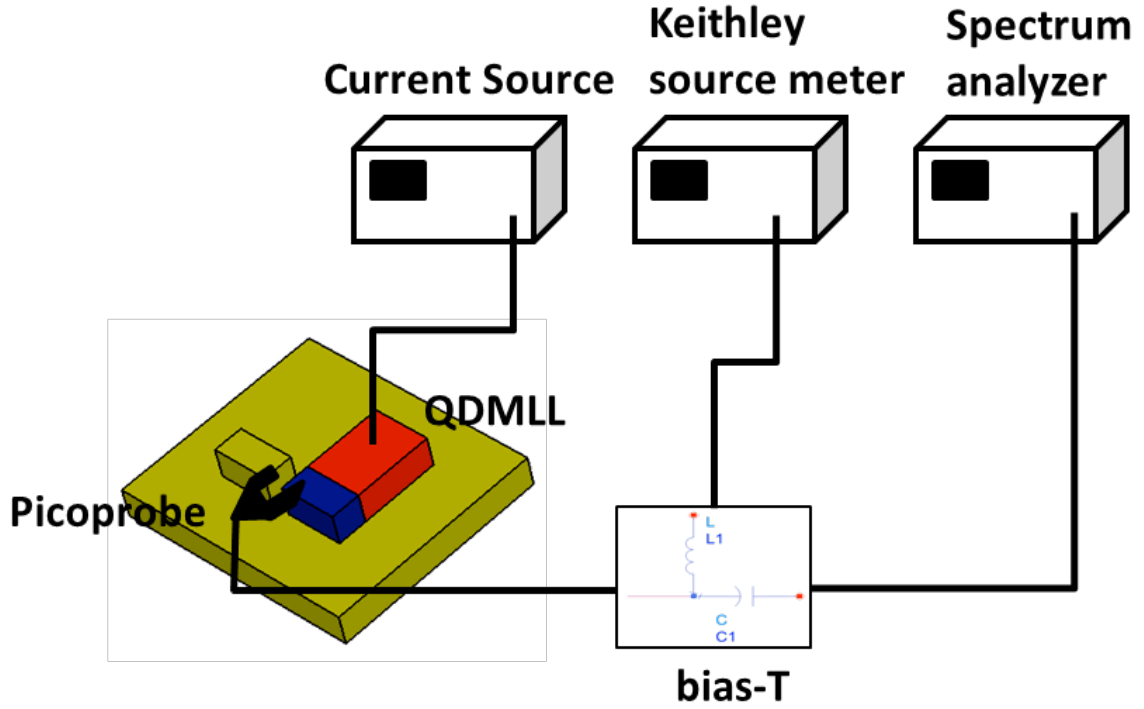


Figure 2.3 Experimental setup to measure RF spectrum of photocurrents

For the 4.1-mm long QDMLL, the measured RF spectrum of the photocurrent is shown in Figure 2.4. Under the biasing conditions of -1V and 200-mA, the intensity of photocurrent is measured to be -3.5 dBm at 10 GHz and -15.16 dBm at 20 GHz, respectively. The fundamental repetition rate of the QDMLL is 10.19 GHz. The repetition rate is determined based on the equation  $f_r = c/2nL$  where  $f_r$  is the repetition rate of a QDMLL.

$c$  is the speed of light at the vacuum medium,  $n$  is the group index of refraction, and  $L$  is the total cavity length of a MLL. As previously discussed, the pulse signals are generated after the light inside of the cavity finishes its round trip, thereby the effective speed of medium is divided by  $2L$ . Figure 2.5 presents the average photocurrent intensity as the function of pumping currents on the gain-section. From the result, it is noticed that the average amount of photocurrents is proportional to the applied pumping current after the threshold current. However, the status of mode-locking in the QDMLL becomes unstable if the pumping current is over the mode-locking condition.

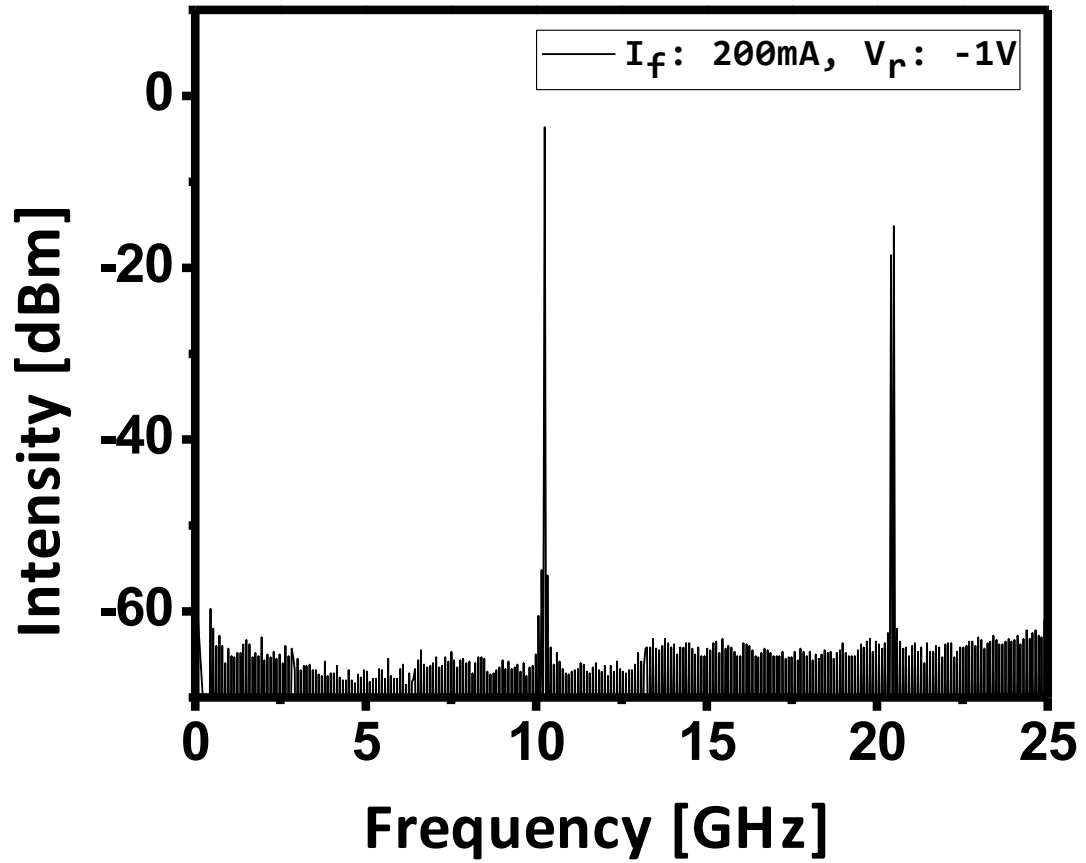


Figure 2.4 Measured RF spectrum of photocurrent of 4.1-mm long QDMLL for the conditions of -1V and 200mA

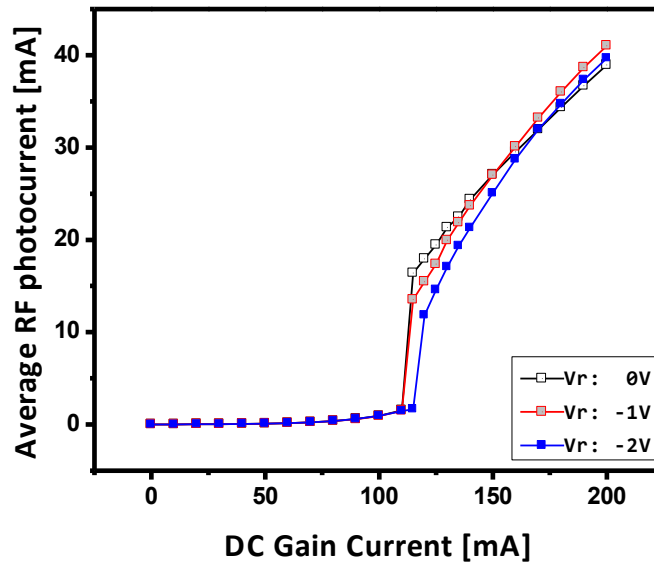


Figure 2.5 Measured average amount of photocurrents as a function of an applied pumping current

For a QDMLL to be an efficient microwave source, it is required to control both the amplitude of its output signal and its phase. After conducting [S]-parameter measurements using the setup in Figure 2.6, the output phase of a MLL is extracted based on the measured impedances of a QDMLL. Compared to the RF-spectrum measurement setup previously shown in Figure 2.3, the DC voltage on an absorber is applied through the network analyzer without the bias-T circuit.

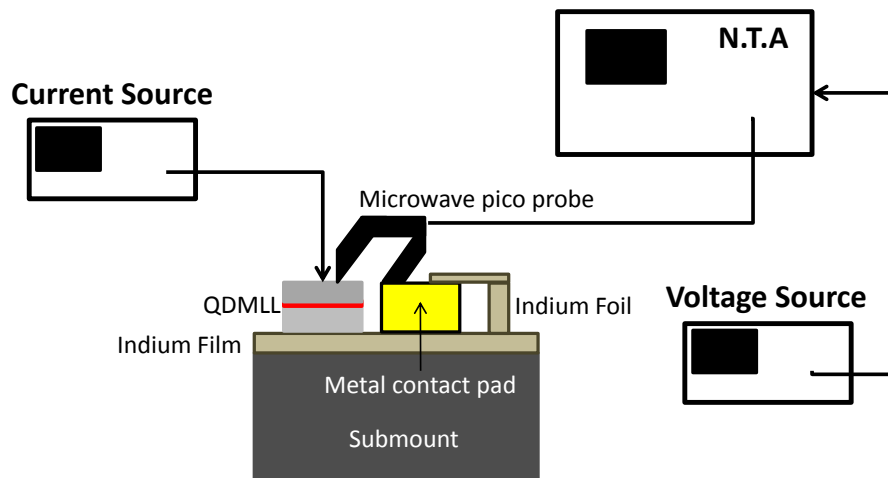


Figure 2.6 The experimental setup to measure the absolute phases of photocurrents

By changing the applied voltage bias on the absorber, the different output phase angles of the photocurrent out of a QDMLL can be observed. To explain the difference in the photocurrent phase, an equivalent circuit model of the absorber is employed under both (a) forward-and (b) reverse-bias conditions, as shown in Figure 2.7 [8]. The simplified equivalent lumped element models are based on the model of a photodetector built on metal-semiconductor-metal. When the absorber is under the forward voltage bias, the phase of the impedance is computed to be  $\theta_f = \tan^{-1}(\omega L / R_s)$ . On the other hand, the phase of the reverse biasing condition is  $\theta_r = \tan^{-1}\{ (L / R_p) [1 + (\omega C_T R_p)^2 - (C_T / L) R_p^2] \}$ . Here,  $\omega$  is the angular frequency,  $L$  is the inductance value,  $R_s$  and  $R_p$  are the series and parallel resistances in the semiconductor medium, respectively, and  $C_T$  is the capacitance induced between the top and bottom metal layers. From the simplified result, the phase angle of a reverse bias condition has an additional term compared to that of forward voltage bias so that the output photocurrents of a QDMLL can be produced with different phases by means of varying the DC applied voltages on the absorber.

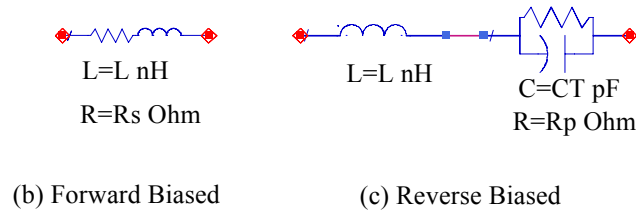


Figure 2.7 Equivalent lumped element models under (b) forward biasing condition and (c) reverse biasing condition

This result is used later to design a compact phased antenna array integrated with QDMLLs. In order to support the theory, the output phases of photocurrents are measured by changing the applied voltage biases in Figure 2.8. In the plot, the result under the pumping current is presented in Figure 2.8 (a). We also compared the measured data to that of the unpumped case in (b). Finally, the phase angle of the output photocurrent,  $\theta_{ph}$ , can be extracted from the measured  $[\Gamma]$ -matrix based on the relation below.

$$\theta_{ph} = \tan^{-1} \left( \frac{\Gamma_{real}}{\Gamma_{imag}} \right)$$

Figure 2.9 shows the change in phase at different frequencies. When the pumping current is applied on the gain-section, the phase angle difference from  $V_{app}$ : -2V to  $V_{app}$ : +0.5V is larger than that without the pumping current. The most variation in the phase angle occurs when the applied voltage is increased from -2 V to +0.5 V with a pumping current and the difference of angles is measured to be  $10^\circ$  at 10 GHz.

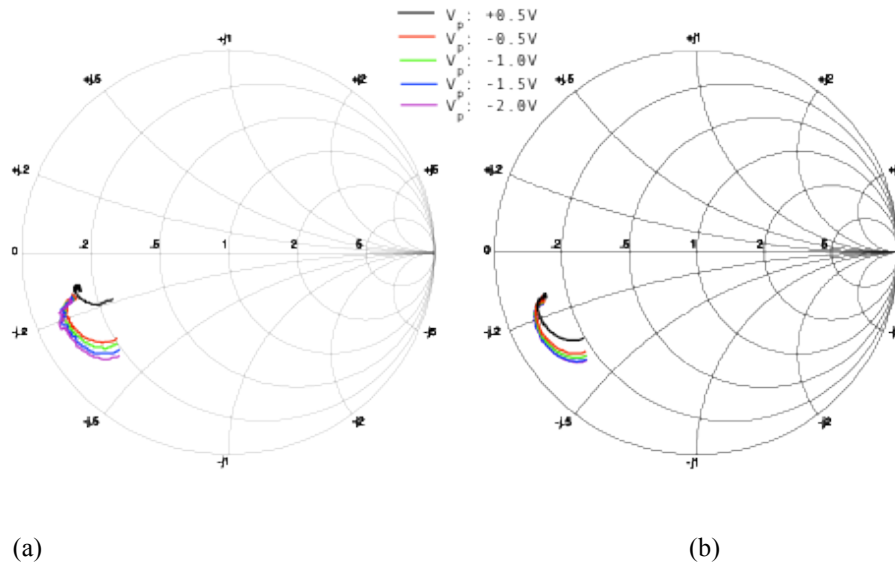


Figure 2.8 Measured  $\Gamma$  of a QDMLL on the smith chart from 5 GHz to 15 GHz under the biasing conditions of (a)  $I_{app}$ : 150mA,  $V_{app}$ : -2 V ~ +0.5 V, (b)  $I_{app}$ : N/A,  $V_{app}$ : -2 V ~ +0.5 V

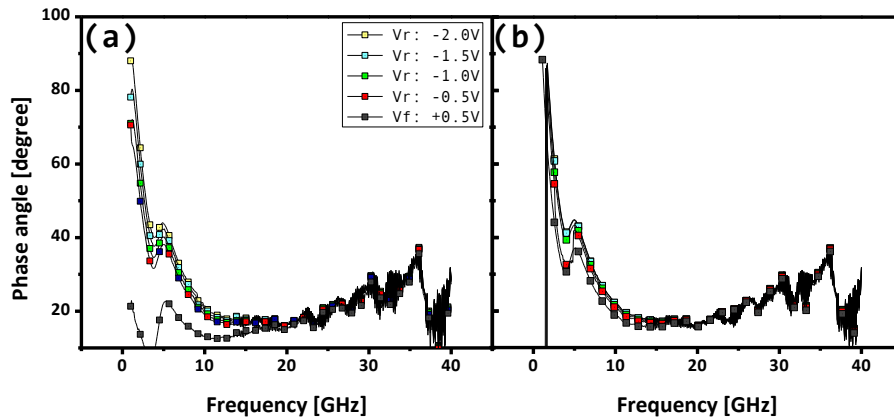


Figure 2.9 The measured phase angle of the photocurrent out of the 4.1-mm long QDMLL under the biasing conditions of (a)  $I_{app}$ : 150mA,  $V_{app}$ : -2 V ~ +0.5 V, (b)  $I_{app}$ : N/A,  $V_{app}$ : -2 V ~ +0.5 V

## 2.5 Reconfigurable microwave pulse generator

In the previous section, a traditional two-section QDMLL was presented. It consists of a single gain and saturable absorber. The repetition rate can be estimated by its total cavity length. According to the repetition rate equation with the cavity length ( $f_r = c/2nL$ ), the repetition rate is inversely related to the length of a cavity. The equation indicates that higher rates can be obtained by making the laser chip shorter. However, the cavity length of a QDMLL is not much shorter than 1-mm because of the size of the absorber. The absorption is not sufficient with shorter absorber lengths. This results in the fundamental repetition rate not being higher than 40 GHz. To overcome this limit for the higher order repetition rates, the multi-section QDMLL is proposed. It consists of connections of segmented QDMLLs and isolations. The generation of a desired higher repetition rate becomes difficult to satisfy because of the operating requirement that the absorber be short enough to simulate higher frequency harmonics and also long enough to maintain sufficient absorption at the same time.

As an alternative, by putting the SA at different segment locations, within the multi-section QDMLL, the laser can harmonically generate pulses at one of possible multiples of the fundamental repetition rate [9]. Instead of using a single SA, the double interval technique applies two separate SAs which stimulate two different harmonics. With the double interval technique, higher orders of the fundamental repetition rate can be obtained. Therefore, the multi-section QDMLLs by a double interval technique can function not only as the higher frequency microwave generation, but also as a reconfigurable microwave source as well. One of the main advantages of using this device is that the repetition rate can be controlled by means of biasing voltages. The ultimate reconfigurable wireless transmitting module can be achieved by combining the multi-section QDMLLs with reconfigurable antennas in future work. For the multi-section QDMLL, the corresponding section number ‘ $m$ ’ that can stimulate the  $n^{\text{th}}$ -order harmonic generation can be determined based on the following equation [9]:

$$m = \frac{N+1}{2} \mp N \left( \frac{1}{2} - \frac{1}{n} \right)$$

where  $N$  is the total number of segments in the laser cavity. For instance, the second harmonic can be generated by locating the SA at section 14 as shown in Figure 2.12. Likewise, the third harmonic is supported by putting the SA at either section 9 or 19. From



the above equation, the actual section number ' $m$ ' for the third harmonic is 8.5 or 18.5. However, the segment numbers are integers so that the values of ' $m$ ' are chosen by rounding them. With the double interval technique, the repetition rate map of the QDMLL of Figure 2.12 is plotted in Figure 2.13 as a function of the gain current and the reverse bias voltage on section 14. It shows the possibility of supporting several orders of harmonics. In reality, not only the 6<sup>th</sup> order of harmonic can be reinforced, but also the 2<sup>nd</sup> and 3<sup>rd</sup> harmonics can be obtained due to the double interval biasing technique on the multi-section QDMLL. Since a single multi-section QDMLL can support diverse repetition rates, it can be an excellent candidate for a reconfigurable microwave source [10].

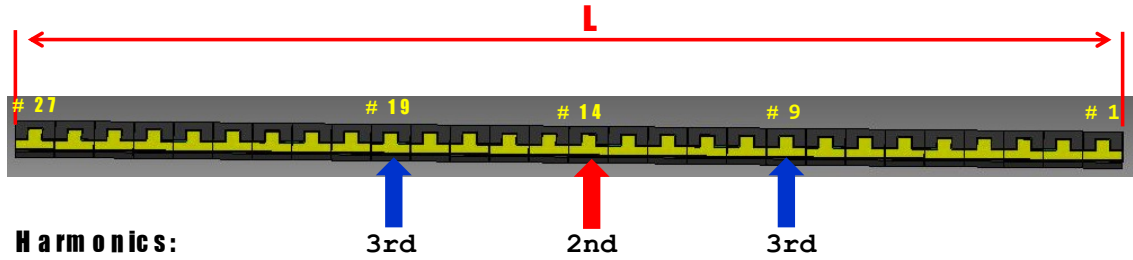


Figure 2.12 Multi-section QDMLL with 27 segments

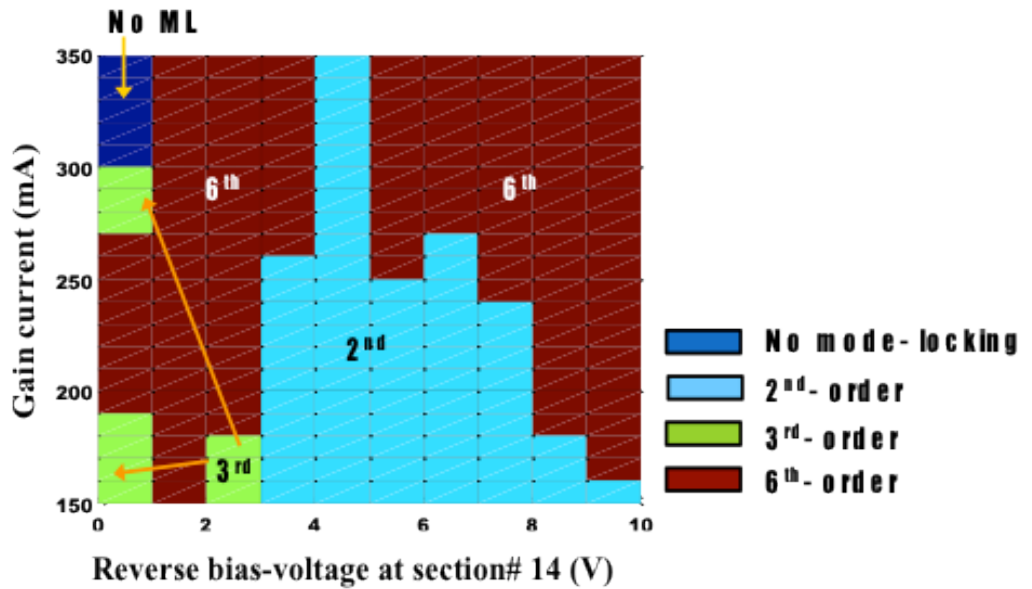


Figure 2.13 An operation map of the reconfigurable multi-section QDMLL

## 2.6 Emission measurement of the QDMLL integrated bow-tie antenna

In order to verify the practical usage of QDMLLs into a microwave system, various types of antennas were designed and integrated with QDMLLs. We fabricated the first chip at 10GHz with a bow-tie antenna as shown in Figure 2.10 [11]. The MLL device has a 1 mm long absorber with the total cavity length of 4mm.

In this particular scheme, the absorber of the MLL is bond-wired to the antenna with 0 V reverse bias applied on the absorber. Testing from the front facet with a spectrum analyzer shows that the MLL device achieves mode-locking at 10.24 GHz with gain currents of 62-mA. The RF spectrum of the radiated signal from the antenna is shown in Figure 2.11. By characterizing the radiation out of the integrated antenna, the concept of using a QDMLL as a compact microwave source can be verified.

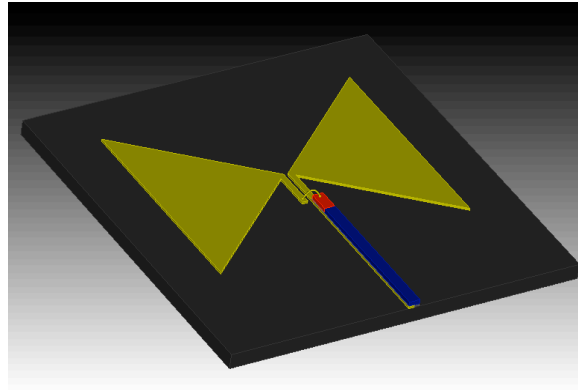


Figure 2.10 The two-section QDMLL-integrated-bowtie antenna

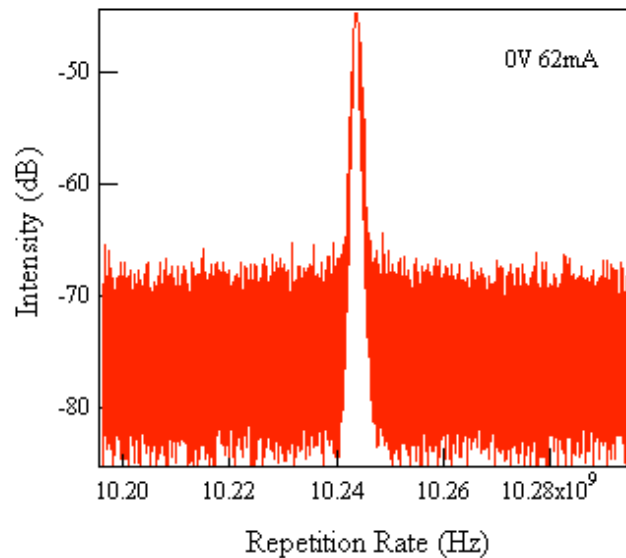


Figure 2.11 ESA spectrum of MLL on the 10GHz antenna chip

### 3. Antennas for Hybrid Integration with a QDMLL

#### 3.1 Antenna Design

Various types of antennas as potential candidates for integration with a QDMLL are proposed. A microstrip antenna has numerous benefits including compact size, light weight, low cost and ease of fabrication. Yet, the resonant modes of the microstrip antennas generally depend on the half-wavelength structure thereby operating bandwidths become rather narrow. Here, we prefer to use broadband antennas that can be matched to a QDMLL over a wide range of frequencies. A bow-tie antenna is used to achieve the QDMLL-integrated-antenna device. The bow-tie antenna is broadband in nature and offers some superior impedance matching characteristics. The antenna structure is determined by its flare angle and bow length. The quasi-static antenna impedance can be computed by the following equation [1]. In Figure 3.1,  $Z_{qs}$  is plotted as a function of the flare angle based on different dielectric permittivities.

$$Z_{qs} = \frac{120\pi}{\sqrt{\epsilon_{eff}}} \left[ \frac{K(\kappa)}{K(\kappa')} \right] \quad \Omega$$

where

$$\epsilon_{eff} = \frac{1}{2}(\epsilon_{r,substrate} + 1) \quad \text{and} \quad \kappa = \tan^2\left(\frac{\pi}{4} - \frac{\theta}{4}\right), \quad \kappa' = \sqrt{1 - \kappa^2}$$

and  $\theta$  is a flare angle.

The 450 $\mu$ m thick semi-insulating Gallium Arsenide (SI-GaAs) is used as a substrate of an antenna whose dielectric constant is 12.9 and loss tangent at resonance is 0.0016. For the 50  $\Omega$  input impedance, the dimensions of an equilateral triangle are determined with a 90° flare angle and 2.8-mm long height. SI-GaAs is used as an antenna substrate. A co-planar strip (CPS) line is the transmission line used to deliver the photocurrent out of a QDMLL into the bow-tie antenna. The geometry of the CPS-line is shown in Figure 3.2.

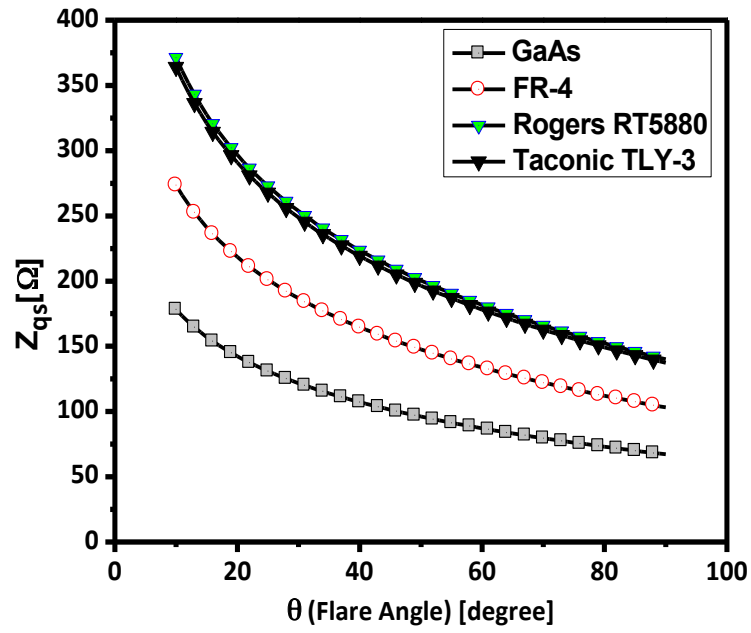


Figure 3.1 Quasi-static impedance of a bow-tie antenna as a function of the flare angle for various substrates: GaAs( $\epsilon_r=12.9$ ), FR-4( $\epsilon_r=4.9$ ), Rogers RT 5880( $\epsilon_r=2.2$ ), Taconic TLY-3( $\epsilon_r=2.33$ )

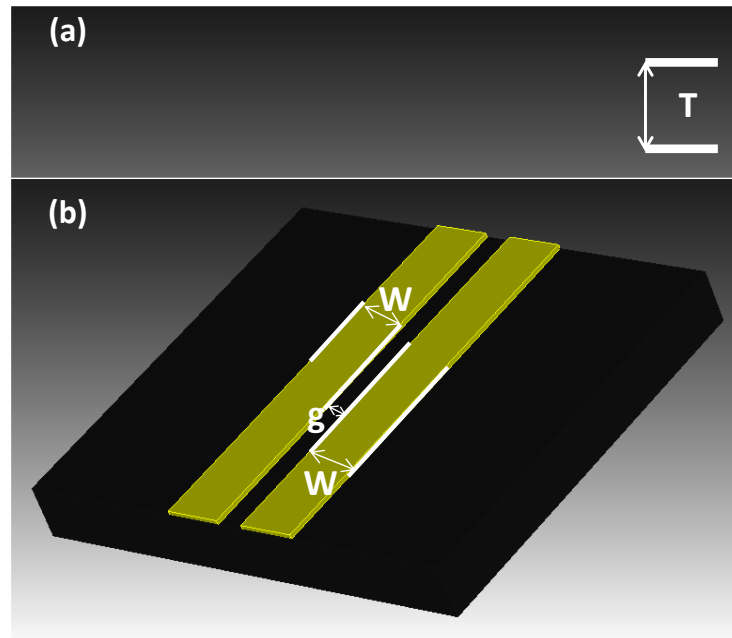


Figure 3.2 (a) Front view of the coplanar strip (CPS) line based on GaAs. (b) Top view of CPS line; T: height of a substrate, W: strip line width, g: air gap

The dimensions of the proposed CPS-line are determined to make the characteristic impedance of a CPS line be  $50\Omega$ . The dimensions of the structure are its air gap (g), line width (W) and its thickness (T). According to the analytical formula presented in [2], the effective dielectric constant is calculated by

$$\epsilon_{eff} = \frac{1}{2}(\epsilon_{r,GaAs} + 1)$$

The characteristic impedance of a CPS line is  $Z_{qs} = \frac{120\pi}{\sqrt{\epsilon_{eff}}} \left[ \frac{K(\kappa)}{K(\kappa')} \right] \Omega$

$$\text{where } \kappa = \sqrt{1 - \frac{\sinh^2 \left[ \frac{\pi}{2T} \left( \frac{g}{2} \right) \right]}{\sinh^2 \left[ \frac{\pi}{2T} \left( W + \frac{g}{2} \right) \right]}} \quad \text{and} \quad \kappa' = \sqrt{1 - \kappa^2}$$

T= height of the substrate, W= strip line width, g= air gap and  $\mathbb{K}$  is the complete elliptical integral of the first kind.

In Figure 3.3, the characteristic impedance of the CPS line is computed as a function of its air gap. The result indicates that its impedance is proportional to the air gap. Likewise, for different gaps, the impedances are also calculated as a function of line width in Figure 3.4. It shows that the characteristic impedance is inversely proportional to the CPS line width. As a final choice, the width of the CPS line is chosen to be 160- $\mu\text{m}$ , separated by 20- $\mu\text{m}$  air gap for a  $Z_{c,CPS} = 50 \Omega$  at 10 GHz. The scheme of a bow-tie antenna is presented in Figure 3.5.

Based on the determined parameters, the height (H) of the triangle of the bow-tie antenna is optimized by using commercial software. To perform the field simulation, we use the CST–Microwave Studio Suite [3].

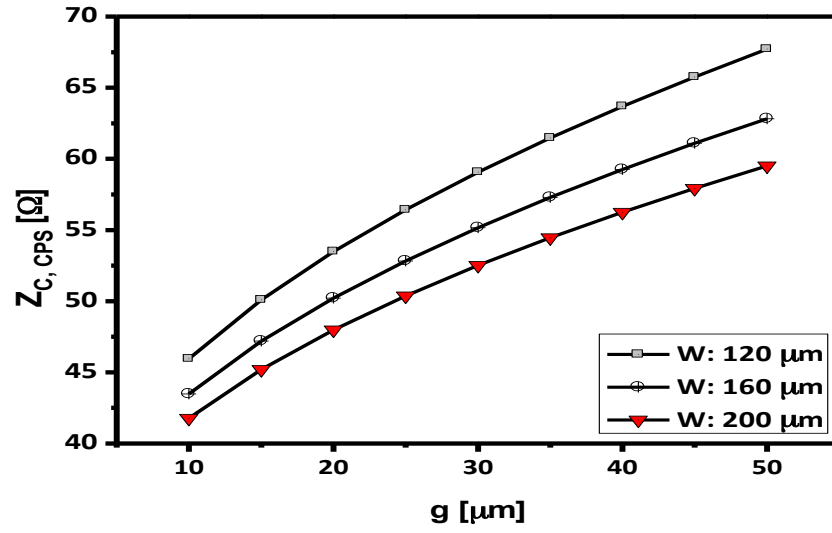


Figure 3.3 Quasi-static characteristic impedance of a co-planar strip (CPS) line as a function of the air gap ( $g$ ) for various CPS line's width ( $W$ ):  $\epsilon_r=12.9$  (Semi-insulating Gallium Arsenide),  $h=450 \mu\text{m}$

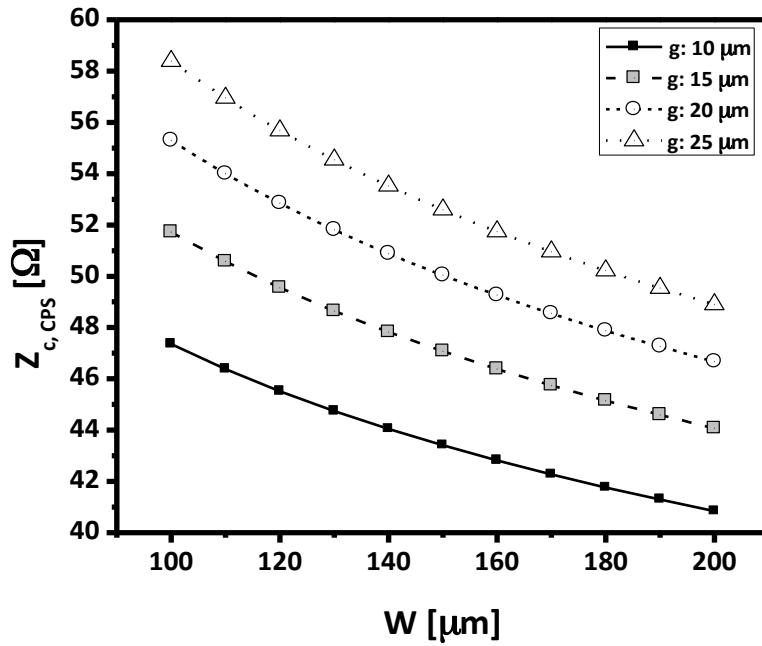


Figure 3.4 Quasi-static characteristic impedance of a co-planar strip (CPS) line as a function of the CPS line's width ( $W$ ) for different air gaps ( $g$ ):  $\epsilon_r=12.9$  (Semi-insulating Gallium Arsenide),  $h=450 \mu\text{m}$

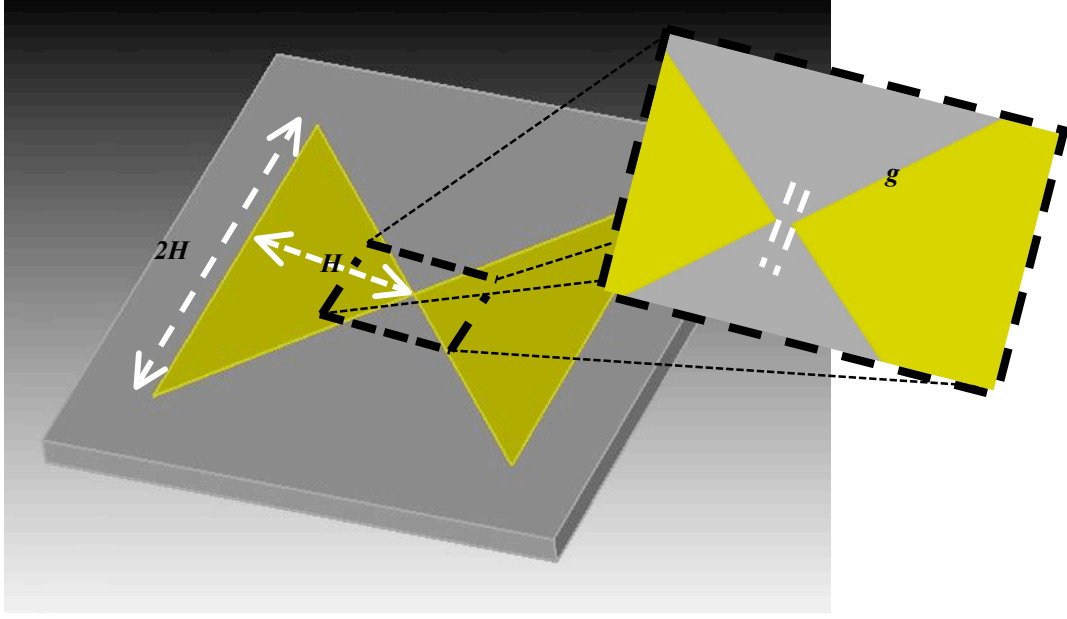


Figure 3.5 A bow-tie antenna with 90° flare angle. The height of a triangle is  $H$  and the base is  $2H$ . Two bows are electrically separated by an air gap (' $g$ ')

### 3.2 Two-port simulation technique into an antenna design

To determine the suitable height ( $H$ ) of a triangle, we used the 2-port simulation technique. We can compute the [S]-parameter data of a 2-port model of a bow-tie antenna using the electromagnetic (EM) software such as the CST-MWS. Based on the calculated [S]-parameters, the admittance [Y] parameters of the bow-tie antenna can be determined by the following equations

$$[Y] = \frac{1}{D} \begin{bmatrix} (1 - S_{11})(1 + S_{22}) + S_{12}S_{21} & -2S_{12} \\ -2S_{12} & (1 + S_{11})(1 - S_{22}) + S_{12}S_{21} \end{bmatrix}$$

Where  $D = (1 + S_{11})(1 + S_{22}) - S_{12}S_{21}$ . In general, all two-port networks can be categorized with either a  $T$  or a  $\pi$ -network. In this research, we used the  $\pi$ -network to analyze the simulation result. With previously computed [Y]-parameters, the series and parallel admittances ( $YY_s$ ,  $YY_p$ ) are calculated by the following equation.

$$YY_s = -y_{21}$$

$$YY_p = y_{11} + y_{21}$$

Next, the impedances are established by the inverse relation of  $YY_s$  and  $YY_p$ .

$$ZZ_s = 1 / YY_s$$

$$ZZ_p = 1 / YY_p$$

The  $\pi$ -network model with the impedances of a bow-tie antenna is shown in Figure 3.6. By using this technique, the complex network models are simplified and easily analyzed. In Figure 3.7, the various impedances of the  $\pi$ -network are provided as a function of frequency range over 8-to-12 GHz for various heights (H) of the antenna. Its result at 10 GHz is tabulated in Table 3.1.

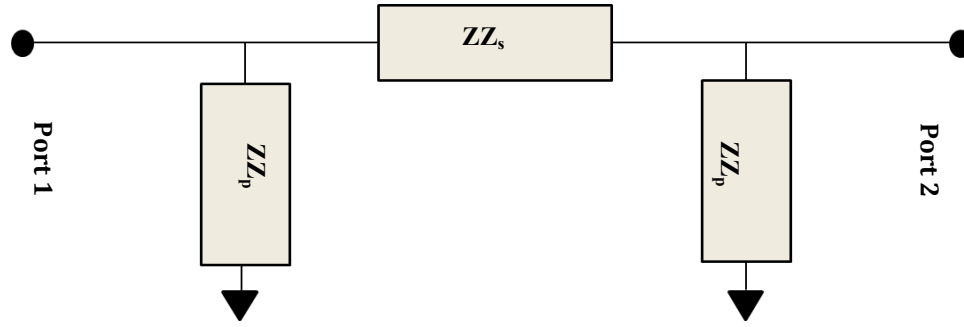
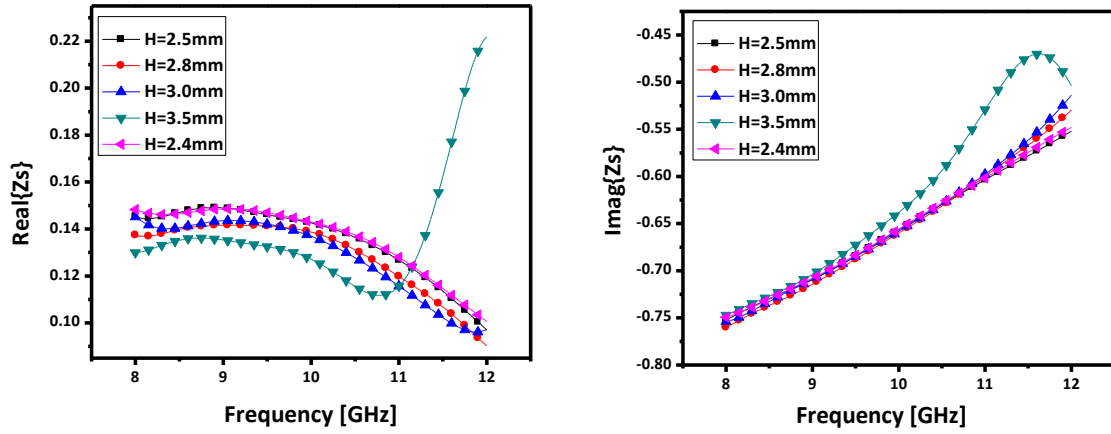


Figure 3.6 Impedance  $\pi$ -network model of a bow-tie antenna





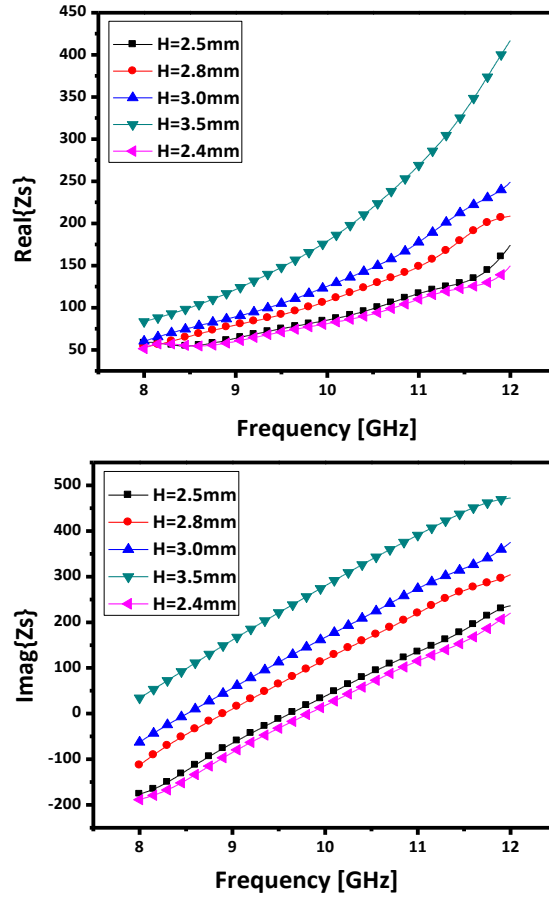


Figure 3.7 Computed impedance of a bow-tie antenna for various triangle heights

Bow height [mm]	$ZZ_s$ [ $\Omega$ ]		$ZZ_p$ [ $\Omega$ ]	
	Real	Imaginary	Real	Imaginary
3.5	0.127	-0.638	179	279.7
3.0	0.137	-0.657	125.35	167
2.8	0.139	-0.658	107.7	118.2
2.5	0.143	-0.660	85.15	37.1
2.4	0.143	-0.656	81.1	17.635

Table 3.1 Impedances of a bow-tie antenna for different bow heights

From the numerical results in Table 3.1, the series impedance ( $ZZ_s$ ) of the antenna at 10 GHz can be considered to be negligible compared to the parallel impedances ( $ZZ_p$ ). In addition to that, it is also noticed that the imaginary part of  $ZZ_p$  decreases as the bow height gets smaller. For  $H=2.4$ -mm, the initially proposed  $\pi$ -network is simplified to the network model in Figure 3.8 (a). The impedance of the simplified network model is to be half of that of the parallel components in  $\pi$ -network. Therefore, the impedance of network is  $ZZ_p = 81.1 + j17.635$ . Its

corresponding lumped model is presented in Figure 3.8 (b).

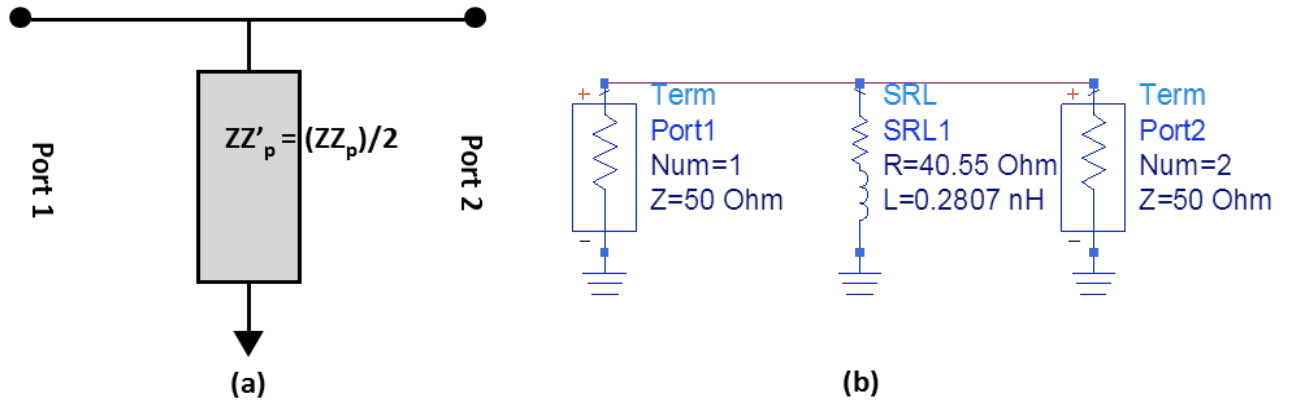
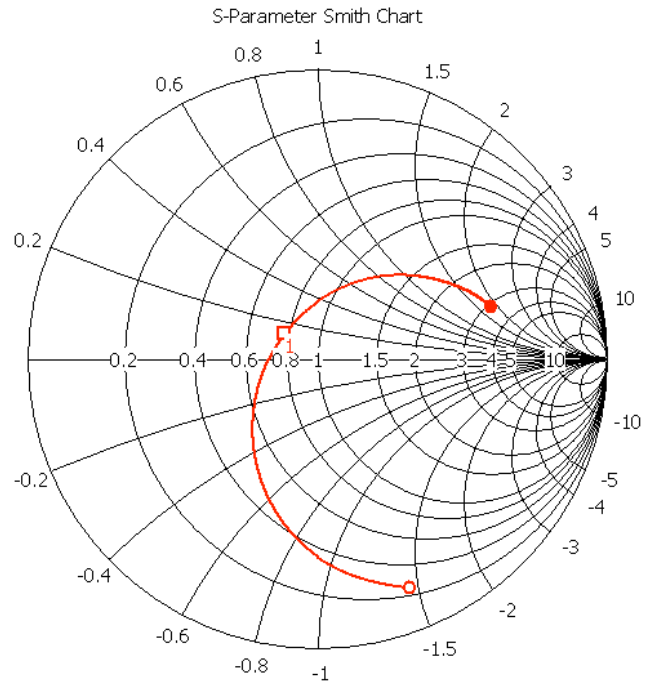


Figure 3.8 (a) Simplified  $\pi$ -network model (b) Equivalent lumped circuit model of a bow-tie antenna

With determined dimensions of the bow-tie antenna;  $H = 2.4 \text{ mm}$ ,  $\theta = 90^\circ$  and  $g = 20 \text{ }\mu\text{m}$ , the return loss of the antenna is simulated and plotted on the Smith chart. The simulated result on Smith chart demonstrates that the antenna impedance is well matched to  $50 \text{ }\Omega$  at  $10 \text{ GHz}$ .

○	8.000 ( 11.92, -68.51) Ohm
□ <sub>1</sub>	10.00 ( 36.78, 6.922) Ohm
●	12.00 ( 146, 88.51) Ohm



Parameter = Frequency / GHz

Figure 3.9 Return loss plot on the Smith chart

### 3.3 Fabrication process and hybrid integration with a QDMLL

Details of the fabrication method are presented in this section. According to the designed dimensions, we built a bow-tie antenna using the photolithographic method. One advantage of the photolithographic approach is the capability of patterning the small structure in the order of  $\mu\text{m}$  on the chosen substrate and its guaranteed accuracy. The entire fabrication procedures for the QDMLL-integrated-bowtie antenna are presented in Figure 3.10. As a beginning step, a thick layer ( $450\mu\text{m}$ ) of SI-GaAs was prepared as a substrate. The wafer cleaning process requires next to sequentially soak the wafers into acetone, methanol and isopropyl alcohol (I.P.A) for 5 min and for each material. After UV laser beam exposure on the surface of the negative photoresist (PR), coated on the SI-GaAs, the desired bow-tie antenna pattern is printed. Since we firstly used the negative type of PR, the photoresist on the antenna image is removed by the development process. Next, thin films of Ti ( $0.05\mu\text{m}$ ) and Au ( $0.3\mu\text{m}$ ) are deposited atop the PR layer by an e-beam metal evaporation. With the help of a thin Ti layer, the deposition of the gold layer is better stuck on the substrate. A bow-tie antenna is finally constructed by a lift-off process. The lift-off process takes the PR away from the surface, thus removing undesired geometries from the substrate. The QDMLL is combined with an antenna through the chip-to-chip bonding method. A thick ( $> \sim 1\mu\text{m}$ ) indium layer is introduced to bond a laser chip on the designed antenna surface. Because the electrical conductivity of indium is in the order of  $10^6$  [S/m] [4], the indium layer can be used as the adhesive without affecting the condition of the electrical properties of device. By applying the same procedure for the antenna fabrication, the indium post is prepared to mount the laser chip. Instead of using an e-beam deposition machine, we used the thermal metal evaporator for this layer. It is mainly due to the fact that the deposition rate of the thermal evaporator is much higher than that of an e-beam deposition method. After constructing the thick indium post, a QDMLL is bonded on one side of the bow by placing it atop of an indium layer and applying heat to the layer. As a final step of the integration, an absorber of a QDMLL is connected on the other side of the bow-tie antenna via wire-bonding.

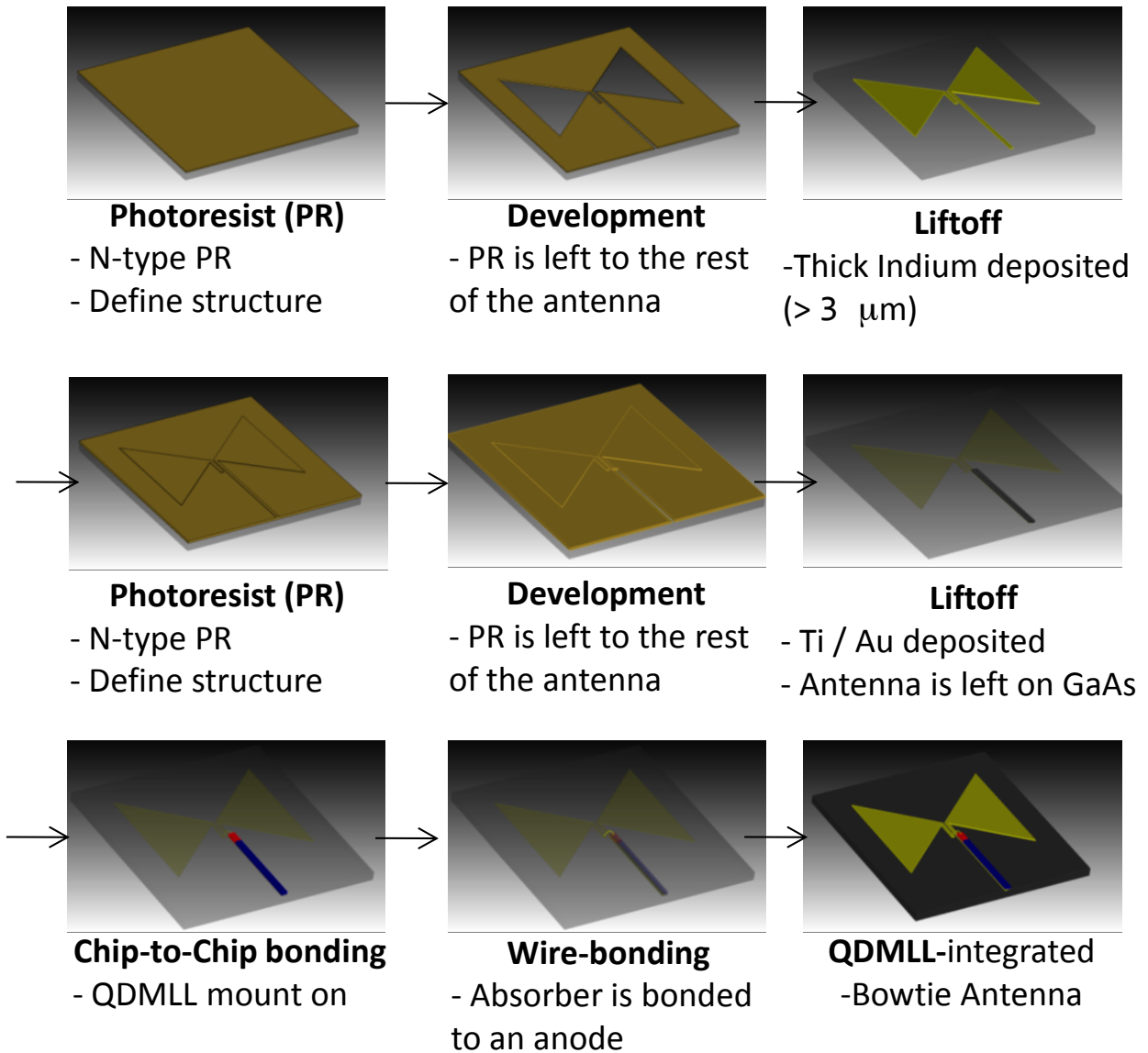


Figure 3.10 Fabrication procedure for the QDMLL-integrated-bowtie antenna

### 3.4 Characterization of the QDMLL-integrated-Antenna

This section presents the experimental setup for the characterization of an integrated antenna and its results. The characterization includes the return loss and emission from the fabricated antenna. For measuring the return loss of an antenna, the on-wafer RF probe approach is used as demonstrated in Figure 3.11. The RF-probe has the signal-ground configuration, which is separated by the 140-mm pitch. The fabricated module is placed on a

copper heat-sink, then the RF-probe contacts on the antenna. The return loss of the antenna is measured by an HP8722D vector network analyzer. To remove the undesirable back scattered effects by a metal sub-mount, the microwave absorbing form is placed underneath the antenna.

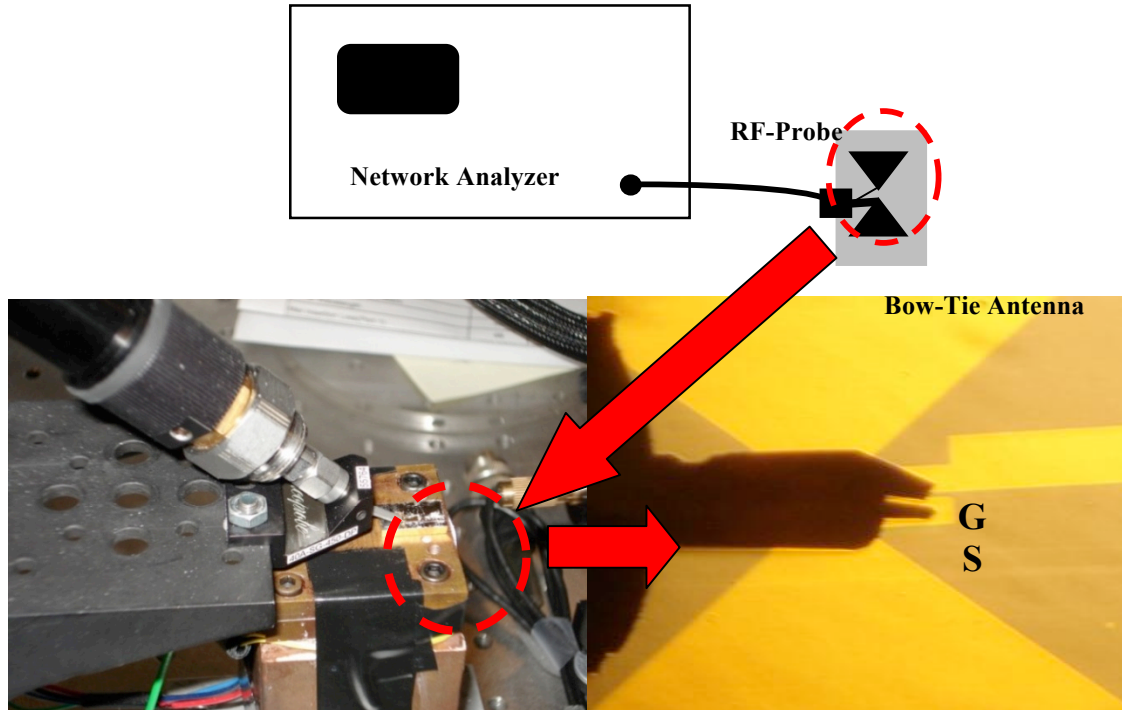


Figure 3.11 Return loss measurement setup: network analyzer (HP 8722D), 140  $\mu\text{m}$  pitching microwave-probe.

The measured return loss in dB is compared with the simulation result in Figure 3.12. In this result, the resonance frequency appears higher than the 10 GHz. In general, the long exposure time to the UV laser beam causes the printed image on the PR to be decreased. Thus, it results in a higher resonance frequency. Although the resonance frequency of the lowest return loss is higher than 10 GHz, its return loss is still less than -10 dB, which indicates a good impedance match. The QDMLL-united active bow-tie antenna is made by following the procedure demonstrated in Figure 3.10.

The setup for the emission measurement out of the integrated antenna module is shown in Figure 3.13. The antenna module under the test is placed on the copper-heat sink which is controlled by a temperature controller. Since the QDMLL sensitively operates by the temperature, the sub-antenna heat controlling unit is a serious requirement. The operation of the QDMLL is controlled by the power supplies. As a receiving / scanning antenna, we use an X-band (8-12 GHz) horn antenna. The radiated power intensity is monitored though

the spectrum analyzer. In Figure 3.14, the measured result of the radiation intensity is shown at 10 GHz. With the measured emission out of an integrated transmitting module, the QDMLL is verified as a feasible compact microwave source. The attempt to improve its radiated power will be discussed in the following section.

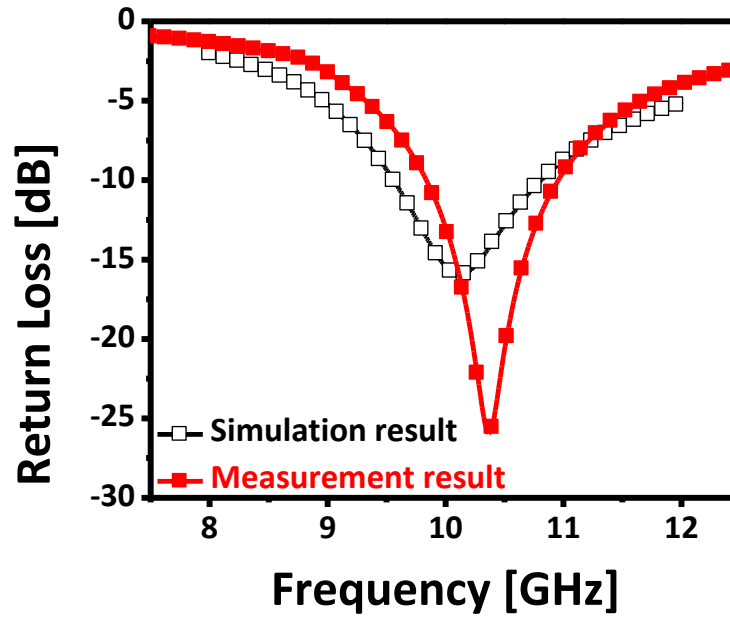


Figure 3.12 Comparison between the measured return loss and simulated one.

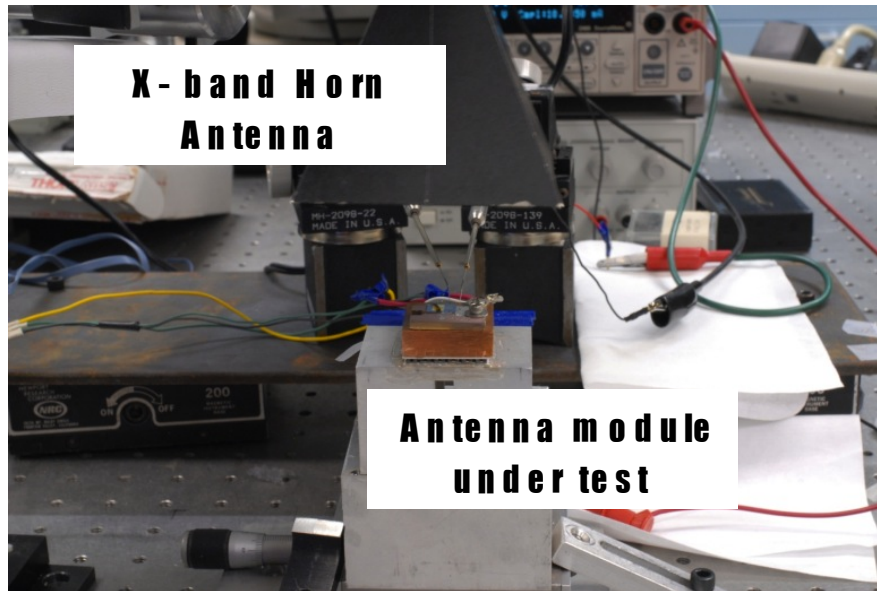


Figure 3.13 Measurement setup for the emission out of an integrated active antenna.

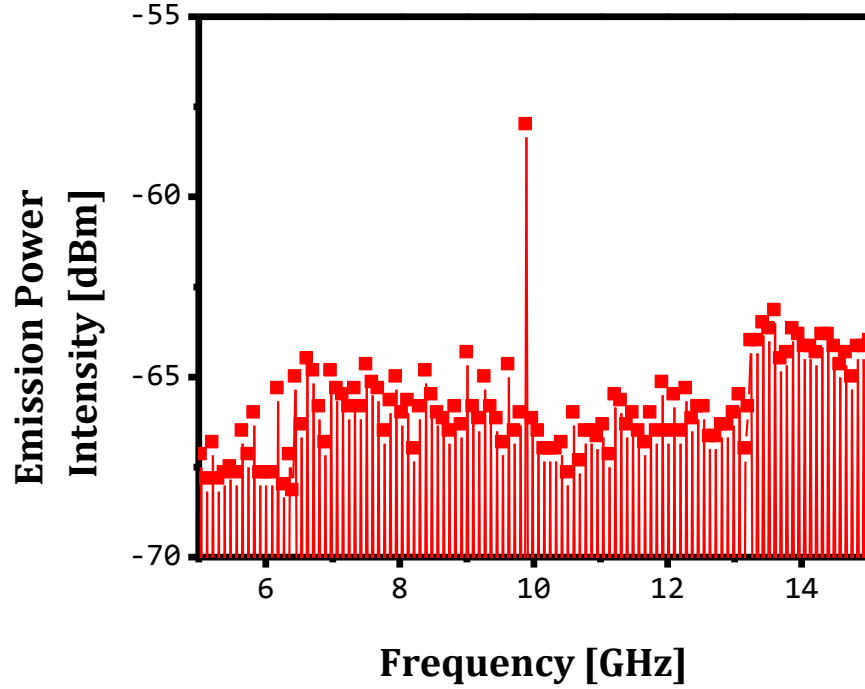


Figure 3.14 Measured emitting power intensity out of the QDMLL-integrated-bowtie antenna.

### 3.5 Pattern estimation of a microstrip antenna integrated with QDMLL

The radiation pattern of a QDMLL-integrated-antenna is estimated in this section. Previously, we measured the emission power intensity using a bow-tie antenna at  $\theta=0^\circ$ ,  $\phi=90^\circ$ . The proper operation of a QDMLL requires the Peltier-type temperature controller that results in a large metalized surface under the MLL chip. Due to its environment, a microstrip-type antenna accommodates this requirement better than a bow-tie antenna. The antenna proposed here is designed to couple at 10 GHz, which is the fundamental repetition rate of the 4.1 mm-long QDMLL. As a base substrate, a 450  $\mu\text{m}$ -thick semi-insulating GaAs is used. The size of the rectangular patch is designed to be 5.1 mm wide and 4.45 mm long. As a compared result in Figure 3.15, the measured return loss is in good agreement with the simulated result at 10 GHz. The electrical signal, optically generated in the SA of the QDMLL, is connected to the patch antenna via wire bonding. Then, the radiated signals are scanned by a horn antenna at different angles;  $(\theta=0^\circ, \phi=90^\circ)$ ,  $(\theta=45^\circ, \phi=90^\circ)$  and  $(\theta=45^\circ,$

$\phi=90^\circ$ ). Figure 3.16 depicts the experimental setup, consisting of an RF-spectrum analyzer (*Agilent 8565EC*), voltage/current sources, and an X-band horn antenna. Three different biasing conditions including ( $I_{app}$ : 100mA,  $V_{app}$ : -1V), ( $I_{app}$ : 120mA,  $V_{app}$ : -1V) and ( $I_{app}$ : 150mA,  $V_{app}$ : -1.5V) are applied on the QDMLL. The X-band horn antenna is used as a receiving antenna and is vertically located above the fabricated patch antenna. The distance between the patch and horn antennas is 3 cm. Figure 3.17 presents the measured RF spectra of the emission power intensity of the QDMLL-integrated-patch antenna for various angles. In Figure 3.17(a), the QDMLL is biased by  $V_{app}$ : -1V,  $I_{app}$ : 100mA. The received emission power intensities are recorded as -64.33 dBm for  $\theta=0^\circ$ ,  $\phi=90^\circ$ , -66.5 dBm for  $\theta=\pm 45^\circ$ ,  $\phi=90^\circ$  and -66.48 dBm for  $\theta=\pm 90^\circ$ ,  $\phi=90^\circ$ . With the evaluated radiation intensities, the signal-to-noise ratio (SNR) is calculated by subtracting the maximum power intensity from the noise level. For instance,  $SNR = -64.33 + 76.4615$  (dBm) = 12.1315-dB for  $\theta=0^\circ$ ,  $\phi=90^\circ$ . Likewise, SNRs for different angles are also computed. For different biasing conditions, the computed SNRs are presented in Table 3.2. According to this table, the highest radiation power is observed at the angles of  $\phi=90^\circ$  and  $\theta=0^\circ$ .

SNR [dB]		-1V / 100mA	-1V / 120mA	-1.5V / 150mA
$\phi=90^\circ$	$\theta=0^\circ$	12.13	11.31	13.98
	$\theta=\pm 45^\circ$	11.31	10.95	11.50
	$\theta=\pm 90^\circ$	10.41	10.77	10.05

Table 3.2 Signal-to-noise ratio (SNR) for different biasing conditions.

The computed SNR values in Table 3.2 are normalized to the maximum SNR. With the normalized signal-to-noise ratios in Table 3.3, the 2-D radiation pattern on the XY-plane can be plotted as shown in Figure 3.18.



Normalized SNR [dB]		-1V / 100mA	-1V / 120mA	-1.5V / 150mA
$\phi=90^\circ$	$\theta=0^\circ$	0	0	0
	$\theta=\pm 45^\circ$	-0.82	-0.36	-2.48
	$\theta=\pm 90^\circ$	-1.72	-0.54	-3.93

Table 3.3 Normalized signal-to-noise ratio (SNR) for the different biasing conditions.

The measured estimated emission patterns for different biasing conditions are compared with the simulated result in Figure 3.18. From the plot, it can be observed that the radiation pattern for the different biases is nearly similar. In addition, the simulated result shows good agreement with the experimental results under various biasing conditions.

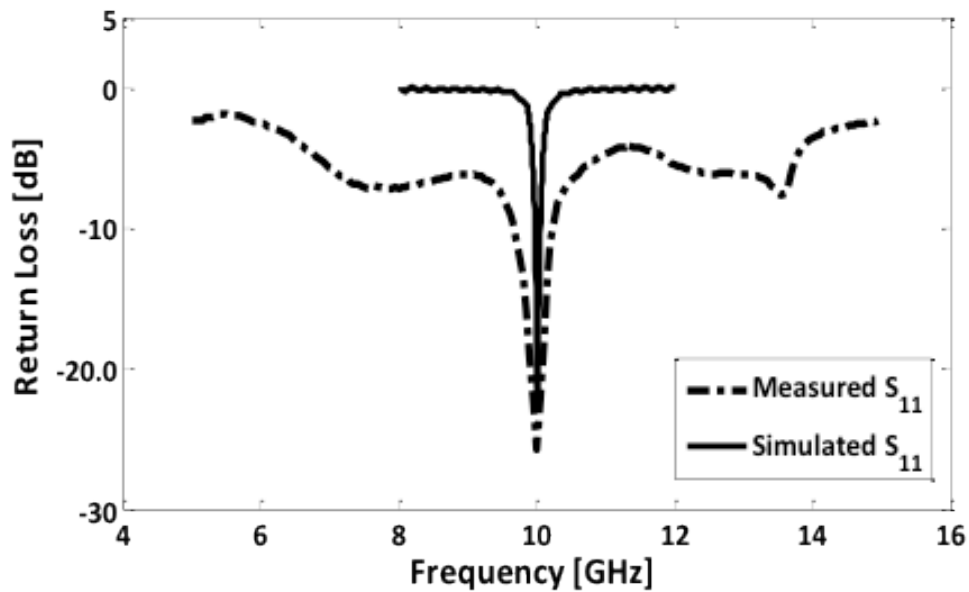


Figure 3.15 Measured and simulated return losses of a fabricated microstrip antenna

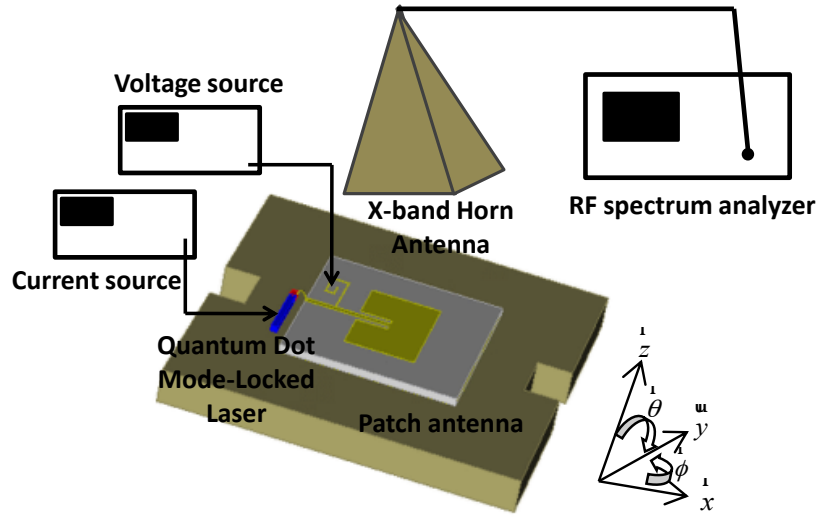


Figure 3.16 The experimental setup for the emission pattern estimation

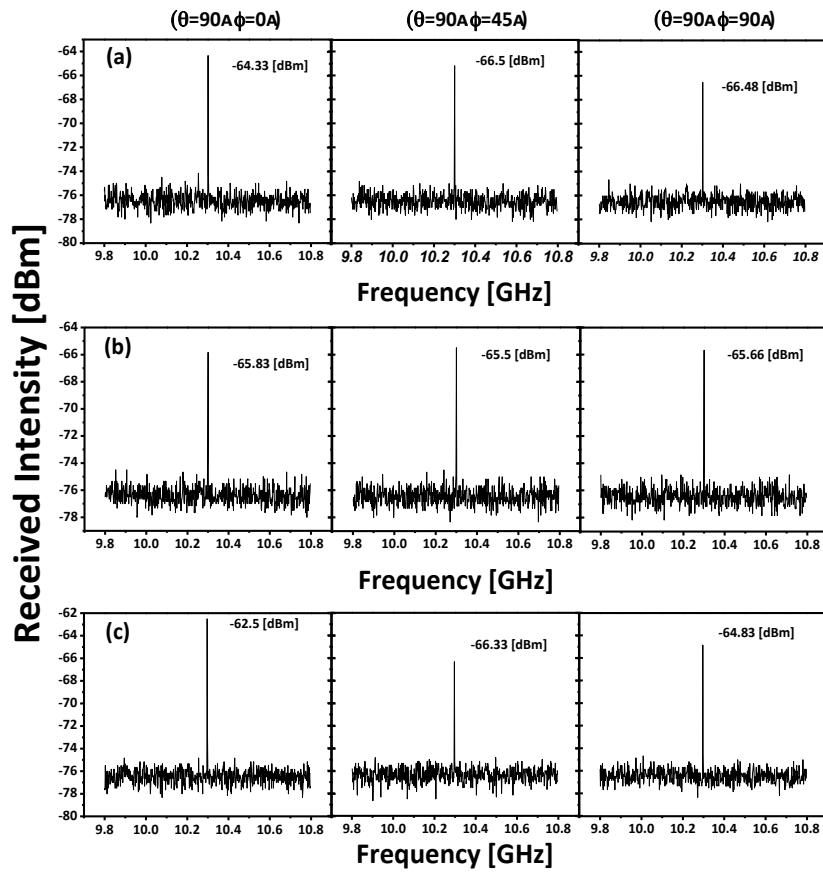


Figure 3.17 RF power spectra of the radiation intensity for different biasing conditions.  
(a) -1V, 100 mA (b) -1V, 120 mA (c) -1.5 V, 150 mA

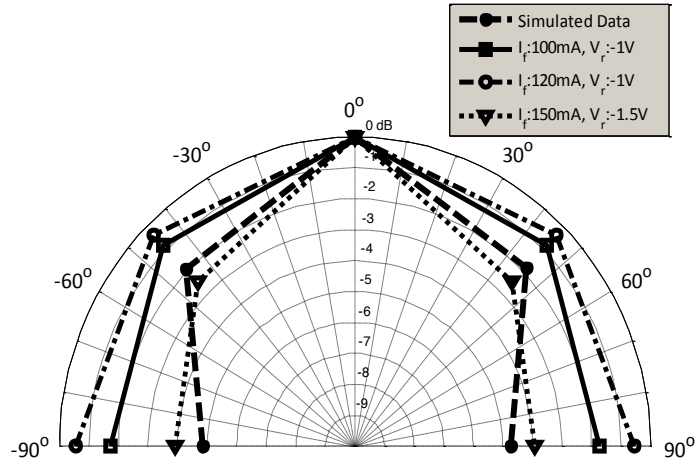


Figure3.18 Comparison of the measured estimated emission patterns and simulated result

### 3.6 Summary

A co-planar strip line and a bow-tie antenna are fabricated and integrated with a 4.1-mm long QDMLL whose repetition rate is 10 GHz. We applied the  $\pi$ -network model to improve the efficiency in designing the antennas. The photo-lithographic method is also used to fabricate the antenna and combine the two devices. The two-section passively mode locked laser is integrated with the fabricated prototype to measure the emission power. Based on the characterized results of an integrated module, the QDMLLs can be verified as possible compact microwave sources.

We characterized the estimated emission pattern out of the microstrip antenna integrated with a QDMLL. We performed the emission measurements by changing the biasing conditions and compared results with the simulation. The experimental result well agrees with the simulation. The results in this section support the concept of the QDMLL as a feasible microwave source.

## 4. Integration with a Bowtie Slot Antenna at 10 and 20 GHz and Antenna Array Beam steering by Biasing the QDMLL

### 4.1 Multi-resonance bow-tie slot antenna

Here another design is presented which works at the first two harmonics (10 and 20 GHz). In Section 2, it was shown that the RF-spectra of the photocurrent (Figure 2.5), under the biasing conditions of  $V_{app}$ : -1V and  $I_{app}$ : 200mA contain second order harmonics. To extend the MLL's operating frequency range beyond the 10 GHz range, the bow-tie slot antenna is proposed. A co-planar wave guide (CPW) is used as the feed line for the antenna. A CPW is commonly used in high frequency RF-applications since its characteristic impedance does not vary too much as a function of frequency

Based on the 450  $\mu\text{m}$  thick SI-GaAs substrate, a CPW with a 0.3 mm-wide microstrip line and 0.2 mm-wide air gap has a 50  $\Omega$  characteristic impedance line. In Figure 4.1, the simulated value is approximately 50  $\Omega$  over the entire frequency range of interest. Figure 4.2 shows the simulated transmission (S21) and reflection (S11) of the 10mm-long CPW. From the figure, one can see that most of the input power is delivered to the load within the frequency range of interest. In order to obtain the suitable dimensions of an antenna, the two-port simulation approach, previously introduced in Section 3, was used.

As mentioned in the beginning of this section, the antenna is designed to resonate at two frequencies; 10 and 20 GHz. The desired resonant frequency of a bow-tie slot antenna can be determined by  $F_{\text{resonance}} = 2nF_0$  where  $n = 1, 2, \text{ and } 3 \dots$  for  $\lambda/2, 3\lambda/2$  and  $5\lambda/2$ . For instance, if  $F_0 = 5$  GHz is chosen, the antenna can resonate at 10 and 20 GHz. The proposed antenna is shown in Figure 4.3. The yellow component is the metal structure and the grey part of the geometry is the dielectric substrate. The two-port simulation approach was used to determine the unknown values of the bow-tie slot antenna including the size of bow base (B), and its height (H). With the values of  $H = 10\text{mm}$ ,  $B = 8\text{mm}$ , Figure 4.4 presents the real and imaginary values of the series-impedance of the two-port model of a bow-tie slot antenna. The parallel-impedances are generally large enough to be regarded as an open circuit. Based on the simulated result, the fundamental resonance frequency ( $F_0$ ) appears at 5GHz.

Next, stub lines were used to cancel the imaginary part of the input impedance of an antenna. The block diagram in Figure 4.5 shows the matching procedure using the ideal transmission (TX) line with a shorted stub line. For matching, the unknown values are required to satisfy the equation of  $|Z_{ant} + jZ_{stub}\tan\theta| = |Z_0|$  where  $Z_0 = 50 \Omega$ .  $Z_{ant}$  is the calculated antenna impedance and  $Z_{stub}$  is the characteristic impedance of the stub line at 10 and 20 GHz. At both 10 and 20 GHz, the antenna resistances ( $R_{ant}$ ) with  $H = 10 \text{ mm}$  X  $B = 8 \text{ mm}$  are approximately  $50 \Omega$ . Thus, the equation is simplified to  $X_{ant} + Z_{stub} \tan\theta = 0$  to meet the matching condition. Using the optimization tools in ADS [1], these unknown variables can be determined. For the calculated variables of  $Z_0 = 75 \Omega$ ,  $\theta_0 = 169^\circ$  at 10 GHz, the detailed dimensions of an antenna are presented in Table 4.1. The schematic of the bow-tie antenna with a stub-line is also presented in Figure 4.6. The simulated return loss is shown for both cases; with and without an impedance matching line. As shown in Figure 4.7, the antenna impedances at 10, 20 GHz are closer to the center of the Smith chart when matching is applied. Figure 4.8 depicts this return loss on a rectangular plot.

..... Unit: [mm]						
<b>B</b>	<b>W<sub>cpw</sub></b>	<b>W<sub>stub</sub></b>	<b>G<sub>cpw</sub></b>	<b>G<sub>stub</sub></b>	<b>H</b>	<b>L<sub>stub</sub></b>
<b>8.0</b>	<b>0.3</b>	<b>0.2</b>	<b>0.2</b>	<b>0.4</b>	<b>10.0</b>	<b>5.25</b>

Table 4.1 Dimensions of the proposed antenna

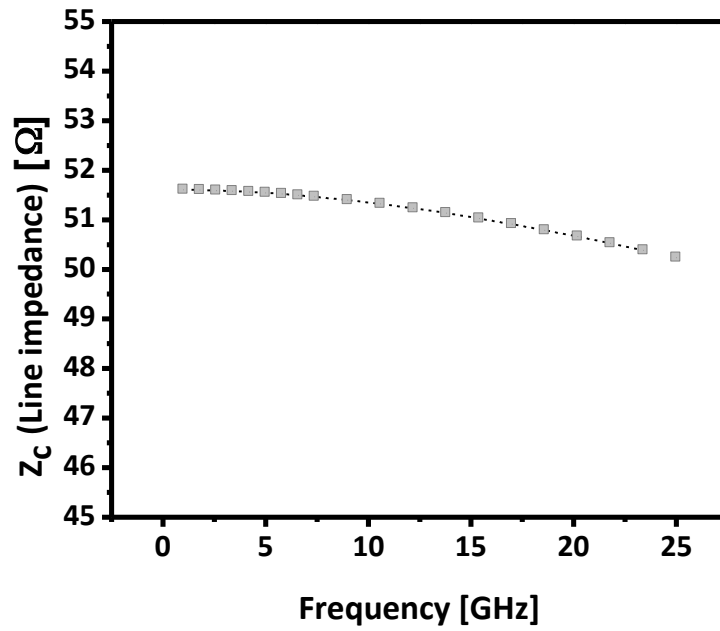


Figure 4.1 Characteristic impedance of CPW line of a 0.3 mm wide center microstrip line and 0.2 mm wide air gap

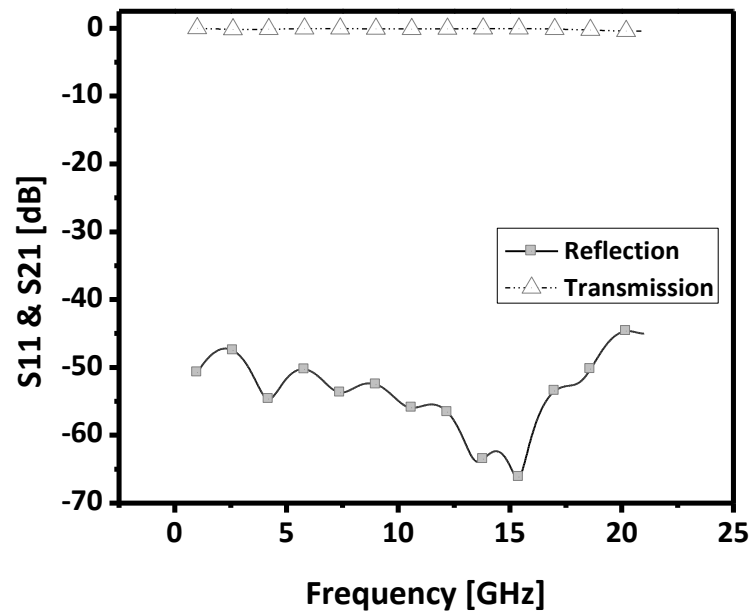


Figure 4.2 A computed transmissions (S21) and reflection (S11) of a 10mm long CPW.

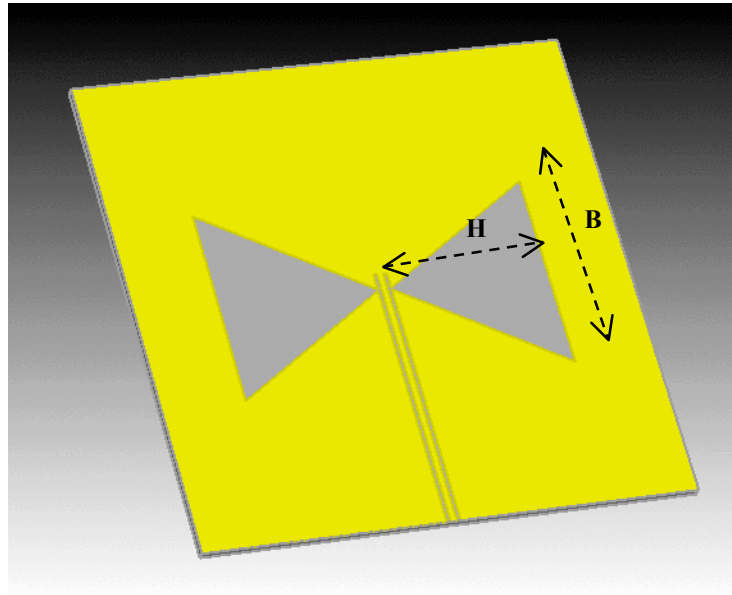


Figure 4.3 A CPW fed bow-tie slot antenna; H: height of a bow, B: width of a bow

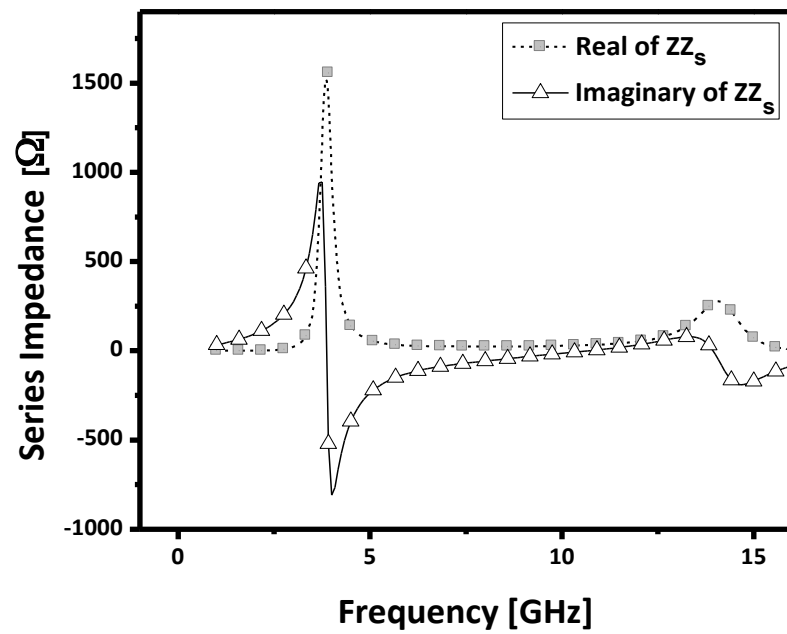


Figure 4.4 Simulated real and imaginary impedances of a bow-tie slot antenna.

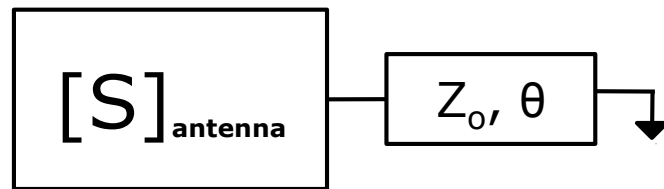


Figure 4.5 The block diagram of impedance matching

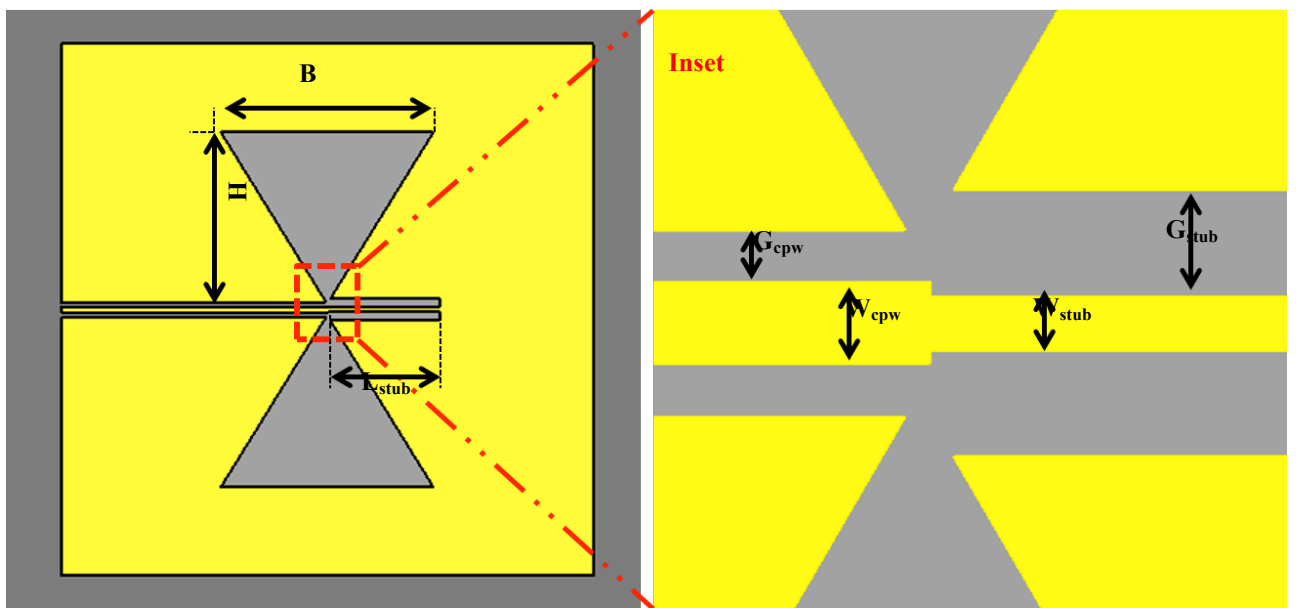


Figure 4.6 The bow-tie slot antenna with a short stub matching line



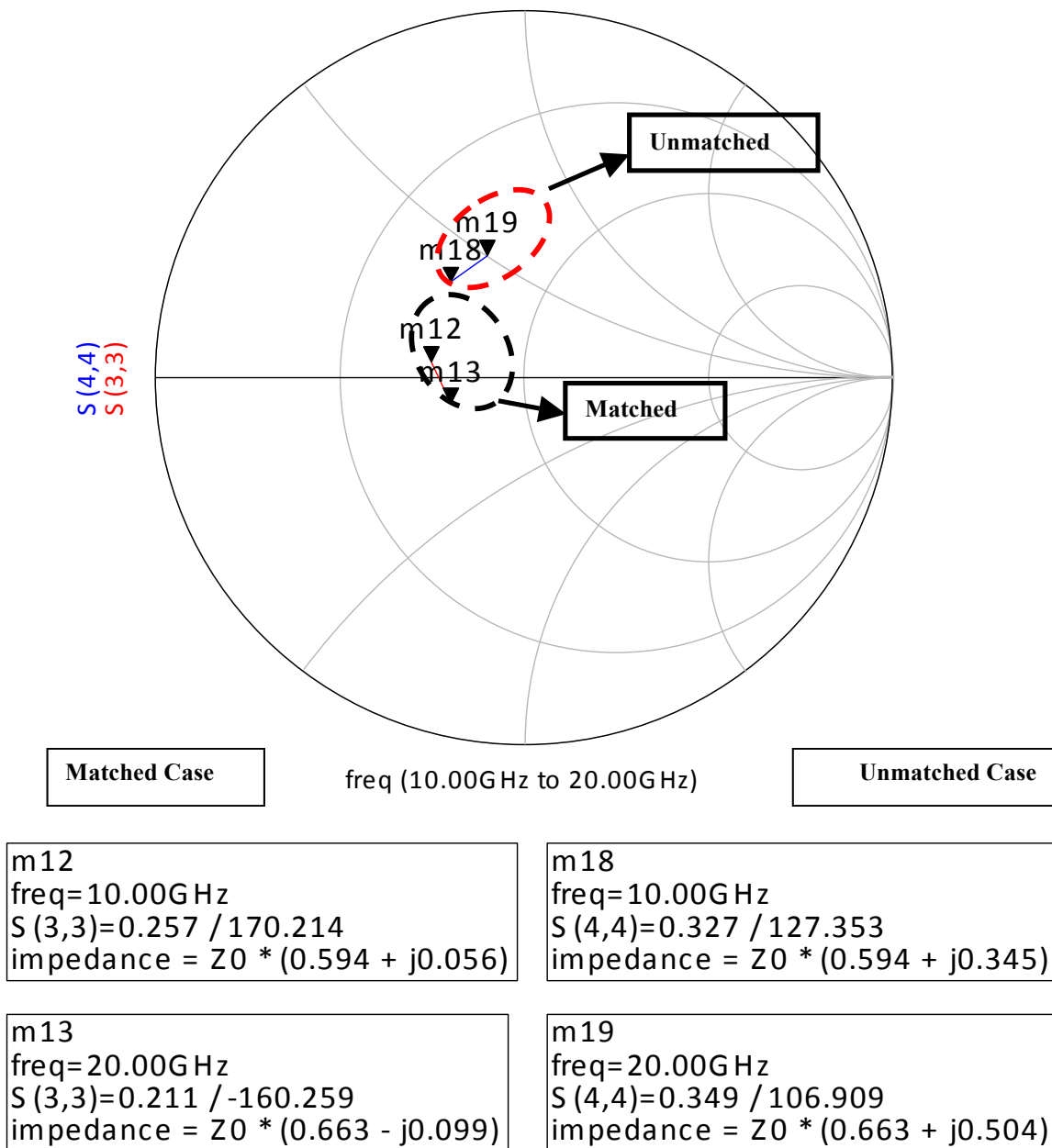


Figure 4.7 Impedances on the Smith chart for both the matched and unmatched case

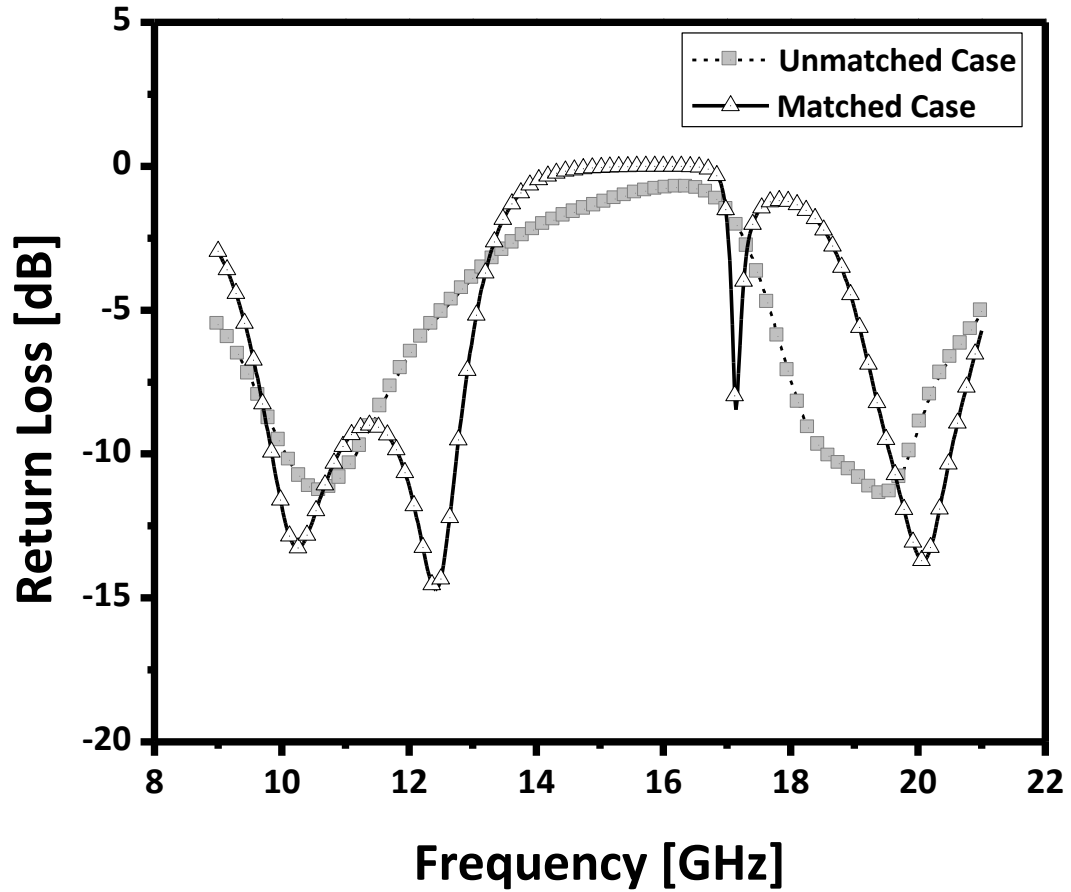


Figure 4.8 Return loss-comparison of the both matched and unmatched case

## 4.2 Antenna fabrication and measurement

Here SI-GaAs is used as the antenna substrate to achieve a seamless integration with the MLL. By using the same material, the laser chip and the antenna allows the monolithic fabrication of the entire RF/photonic device. To realize a  $50\ \Omega$ -characteristic impedance for the required CPW line, a line width of 0.3 mm and a gap of 0.2mm are used. All other dimensions of the proposed antenna are provided in Table 4.1.

The photolithographic method, shown in Figure 3.10, is employed to build the integrated prototype. Figure 4.9 shows the comparison of the measured and simulated  $S_{11}$ -results of the fabricated antenna. The measured and simulated results agree well at the first

resonance frequency but not at 20 GHz (2<sup>nd</sup> resonance). This is because the dimension of the bowtie slot antenna is larger than the actually proposed design.

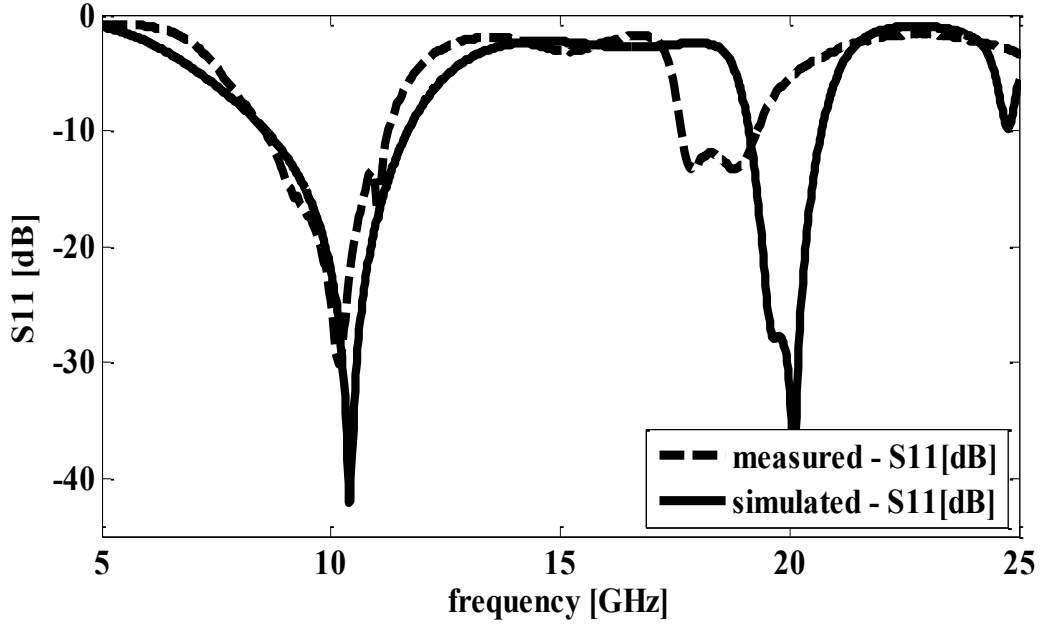


Figure 4.9 Simulated and Measured return losses of a bow-tie slot antenna

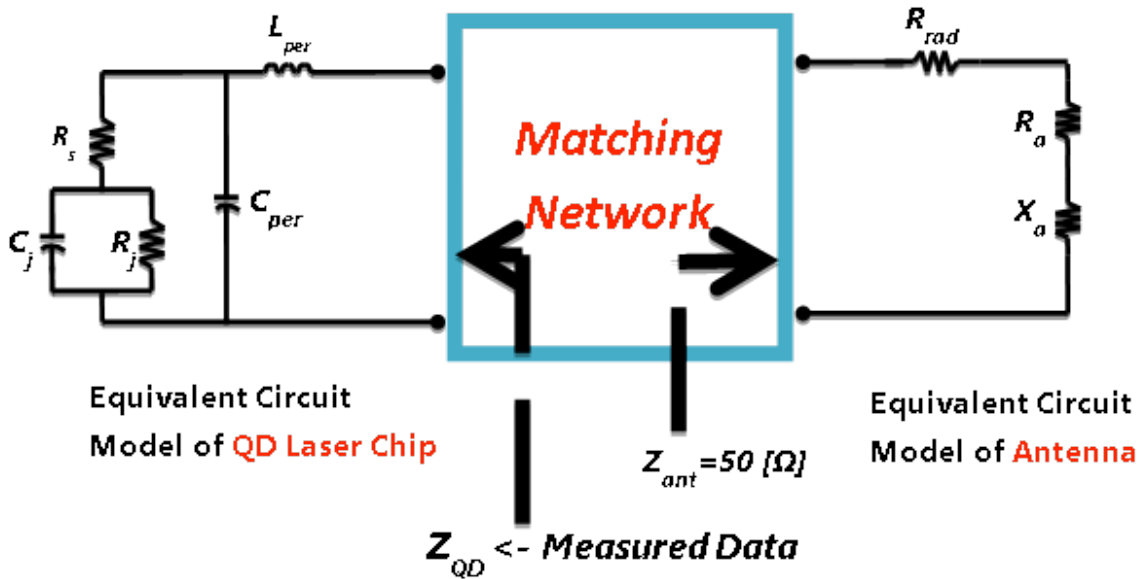


Figure 4.10 Equivalent circuit model of the matching circuit between a QDMLL and a bow-tie slot antenna;  
 $Z_{QD}$ : output impedance of a QD-MLL and  $Z_{ant}$ : impedance of a bow-tie slot antenna

### 4.3 Impedance Matching

To integrate the bow-tie slot antenna in section 4.1.1 to the MLL, the impedance transformer is designed for 10 and 20 GHz; the first and second order harmonics based on the QDMLL's repetition rate. The diagram in Figure 4.10 demonstrates the equivalent lumped element model of the impedance transformer located between the saturable absorber in the MLL and the antenna. The  $S_{11}$  of the quantum dot (QD)-absorber is measured first over the frequency window ranging from 1 to 30 GHz. Based on the measured [S]-parameters and the output impedance of the absorber, one can recalculate  $Z_{QD}$ . In Figure 4.11, the saturable absorber impedance is plotted as a function of reverse bias voltage at both 10 and 20 GHz. The values of its impedance are also tabulated in Table 4.2.

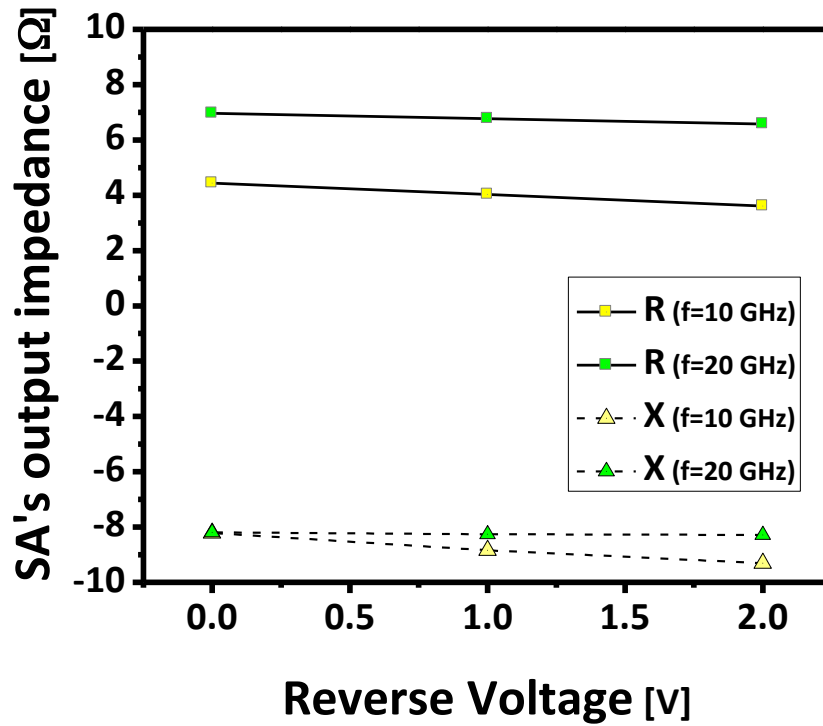


Figure 4.11 Measured output impedance of the saturable absorber in the QDMLL as a function of reverse biasing voltages

Case	Frequency [GHz]	Impedance [ $\Omega$ ]	$S_{11}$ [dB]
Unmatched	10	$4.45-j8.25$	-1.5
	20	$6.95-j8.2$	-2.37
Matched	10	$37.8-j12.3$	-14.17
	20	$56.2-j16.8$	-15.54

Table 4.2 Impedance and  $S_{11}$  in dB in both the matched and unmatched case

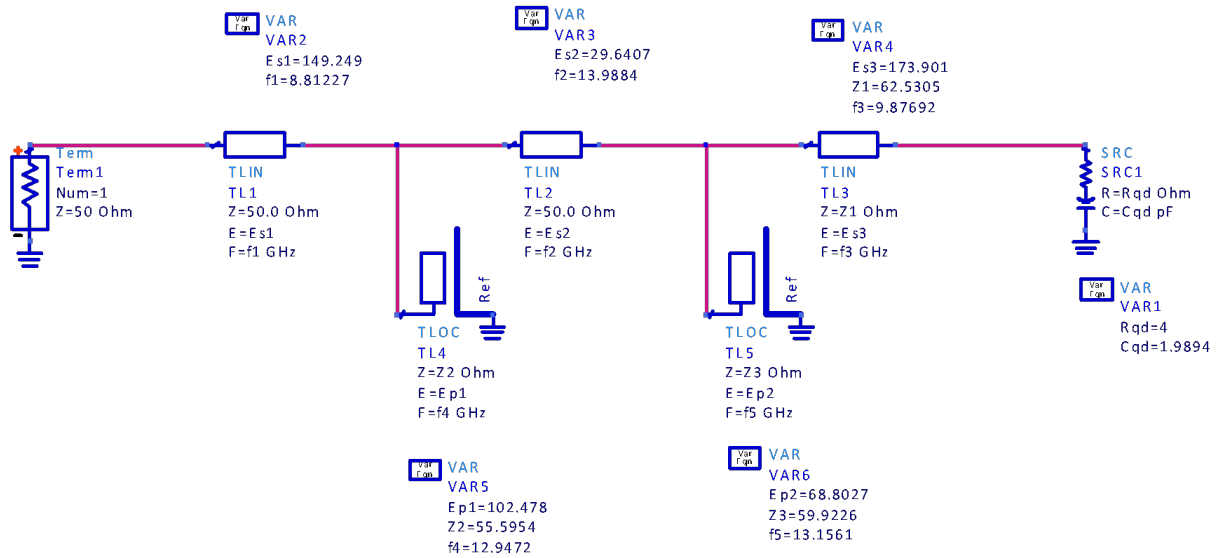


Figure 4.12 Ideal Transmission line model of matching network between the QDMLL and bow-tie slot antenna

The matching network using ideal transmission lines is shown in Figure 4.12. Using fast converging algorithms such as the genetic algorithm [2], the unknown variables including the electrical length, the operating frequency and the characteristic impedance of each transmission line are optimized to meet the requirements. Next, the CPW-based-matching circuit is designed as shown in Figure 4.13. In this design, the abrupt transitions in

the structure are taken into account in the simulation.

The return loss, with and without an impedance matching circuit, is compared in Figure 4.14. According to the computed data, the delivered power to the load is only 29 % at 10 GHz and 43% at 20GHz of the generated power for the unmatched case. With the equation of  $G_{dB} = 20\log_{10}(T_{matched}/T_{unmatched})$  where  $T=S(2,1)$ , the possible gain is computed by employing the impedance transformer. Its result is also shown in Figure 4.14. The outline of the impedance matching circuit and its corresponding dimensions are presented in Figure 3.30 and Table 4.3, respectively. Figure 4.16 shows the bow-tie slot antenna integrated with a dual-band impedance matching network. In the figure, the yellow component is the metal structure and the black one is that of the dielectric. To affirm the progress due to a matching network, the emitting power intensity out of the antenna with a matching circuit is compared with that of an antenna without the aid of impedance transformer at 10 GHz. The result is presented in Figure 4.17. The received power intensity in the matched and unmatched case is -41 dBm and -45.7 dBm, respectively. As a result, the gain in the received power intensity is 4.7 dB. This result agrees with the simulated 5 dB-gain in the return loss.

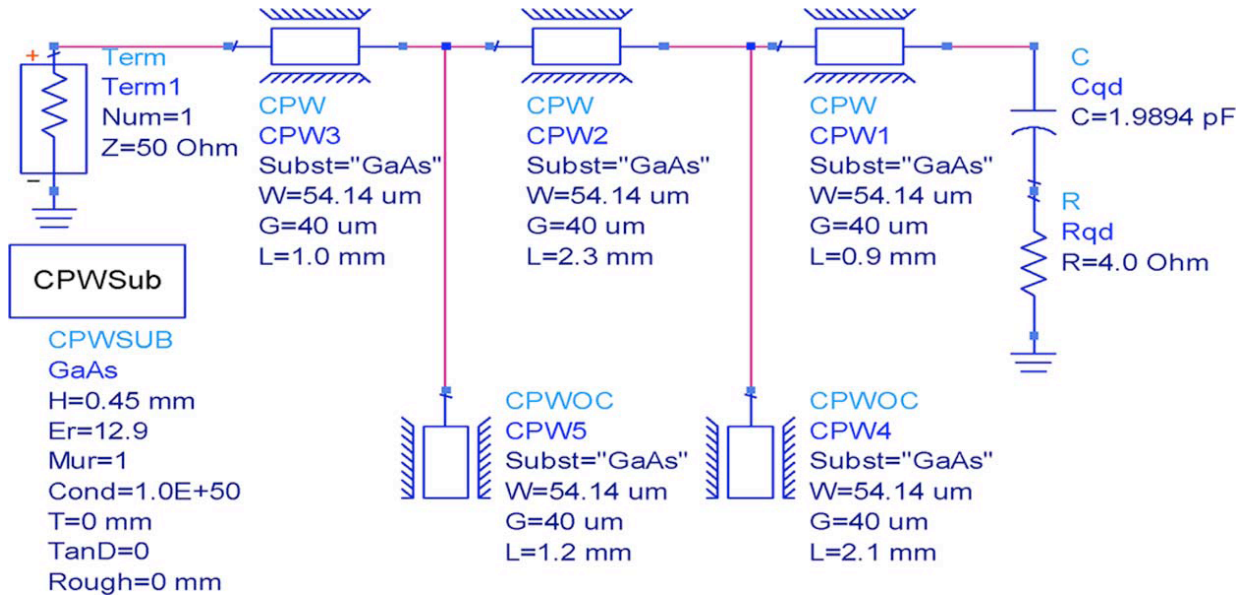


Figure 4.13 The CPW-based-impedance matching circuit between the QDMLL and bow-tie slot antenna

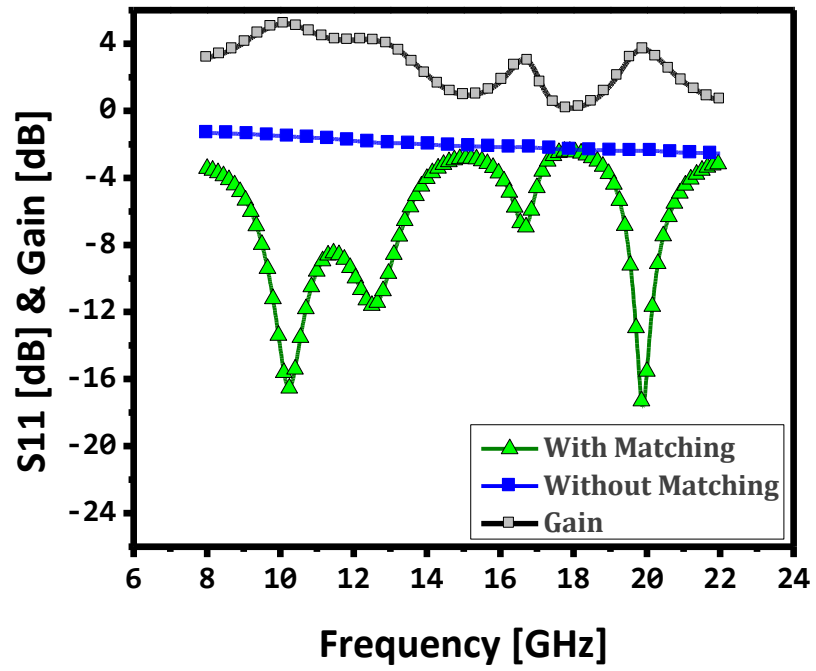


Figure 4.14 The simulated return losses under the consideration of both matched and unmatched cases, and the computed gain in dB

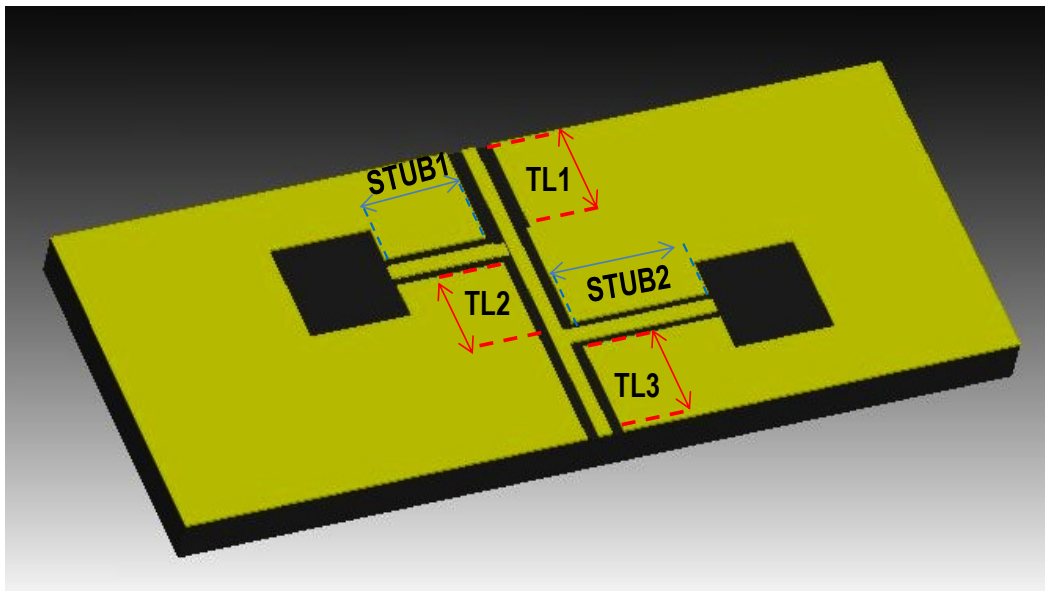


Figure 4.15 The schematic of an impedance transformer of two open stub lines.

Unit: mm			
	W	G	L
TL1	0.3	0.2	3.5
STUB1	0.3	0.26	4.95
TL2	0.3	0.2	2.8
STUB2	0.3	0.31	3.825
TL3	0.3	0.35	3.5

Table 4.3 Dimensions of an impedance matching circuit

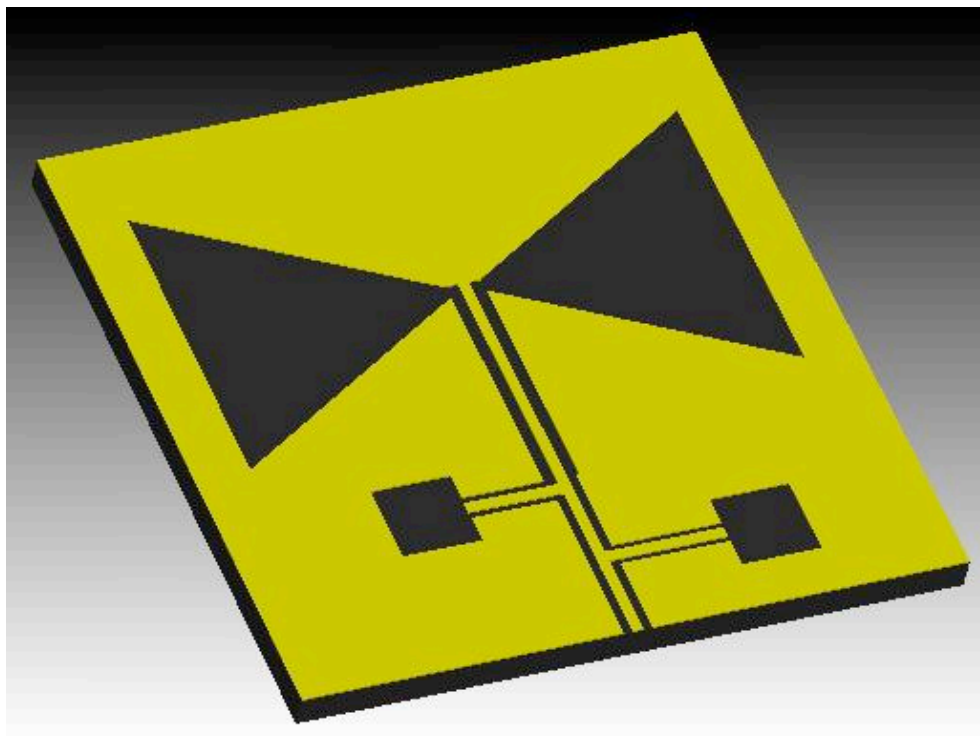


Figure 4.16 A dual-band impedance matching network embedded bow-tie slot antenna



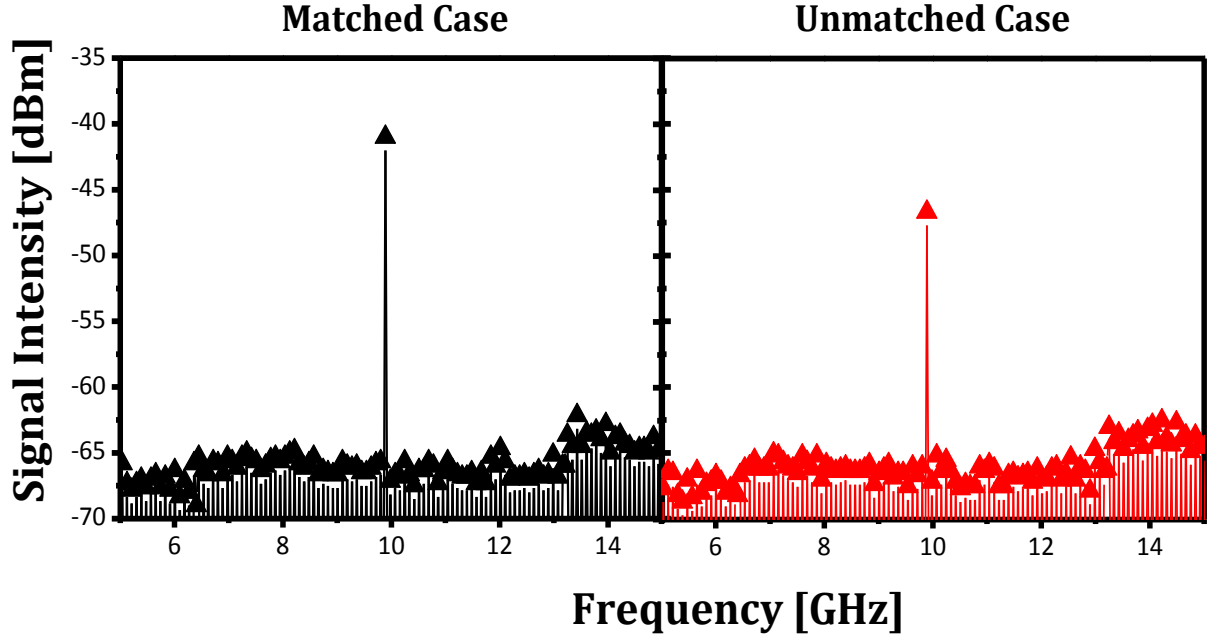


Figure 4.17 Measured signal power intensity comparison between matched and unmatched case

#### 4.4 Tapered slot antenna (TSA) design using the ideal transmission line

Previously, we designed a multiband resonance bow-tie slot antenna and tested the radiation improvement by adding an impedance matching circuit. In this section, a phased array tapered slot antenna is fabricated to perform a beam-steering experiment. Our aim is to also achieve beam steering by changing the bias conditions on the QDMLL and avoid the use of any RF phase shifters.

The tapered slot antenna (TSA) was initially developed by Gibson *et al.* and Yngvesson *et al.* [3, 4]. It consists of a tapered slot etched onto a thin film of metal on a substrate. It produces radiation in the end-fire direction at the wider end of the slot. Since the phase velocity of the travelling waves on the antenna is smaller than the speed of light in free space, the radiation out of an antenna occurs toward the end-fire.

In order to reduce the time and effort to design a TSA, the transmission line model is applied. The length  $L$  of the TSA can be modeled by cascading ideal transmission lines with progressing characteristic impedances and the length of  $L_n$  ( $L_n = L/N$ ) [5]. This can be supported by the electric field distribution profile in Figure 4.18. Thus, the equivalent circuit model of a TSA is also regarded as the cascaded step lines as shown in Figure 4.19. In the equivalent model, the circuit is compared to the series-combined TLINs and shunt

admittance ( $Y_k$ ). TLIN has the characteristic impedance ( $Z$ ), propagation constant ( $b$ ) and length ( $q$ ) at 10 GHz. Any shunt admittances ( $Y_k$ ) are due to step discontinuities between TLINs. The discontinuity is decreased if the step line becomes finite. In other words, the discontinuity admittances are ignored due to the small slot step changes. This approximation is valid because the large number of steps reduces the reflected traveling wave within the slots in the TSA.

Figure 4.20 presents three equivalent ideal TLIN-models of a TSA. Each TLIN is composed of the characteristic impedance ( $Z$ ) and electrical length ( $q$ ) based on the fundamental frequency of 10 GHz. The load impedances of the models are 120pW. For an ideal TLIN model, the propagation constants and electrical lengths are computed as  $b = w/c$ ,  $q = bl$  at  $f = 10$  GHz. Here  $c$  is the speed of light at air and  $w$  is the angular frequency at 10 GHz. By using ADS software tools the unknown values of  $Z$ ,  $l$  are determined. The optimized  $Z$  and  $l$  values of the ideal transmission line are converted to the physical realizations of gap width and length of the slotline. For instance, the size of an air gap is computed based on the line impedance calculation for the slot line. The slotline's physical length ( $l'$ ) is determined by  $l' = (b/b')l$ . Here,  $b'$  is the propagation constant of a slotline at 10 GHz. The values  $b$  and  $l$  are the propagation constant and length of an ideal TLIN, respectively. The slot gaps and line lengths for the three models are presented in Table 4.4. The ideal transmission line modeled TSAs are shown in Figure 4.21.

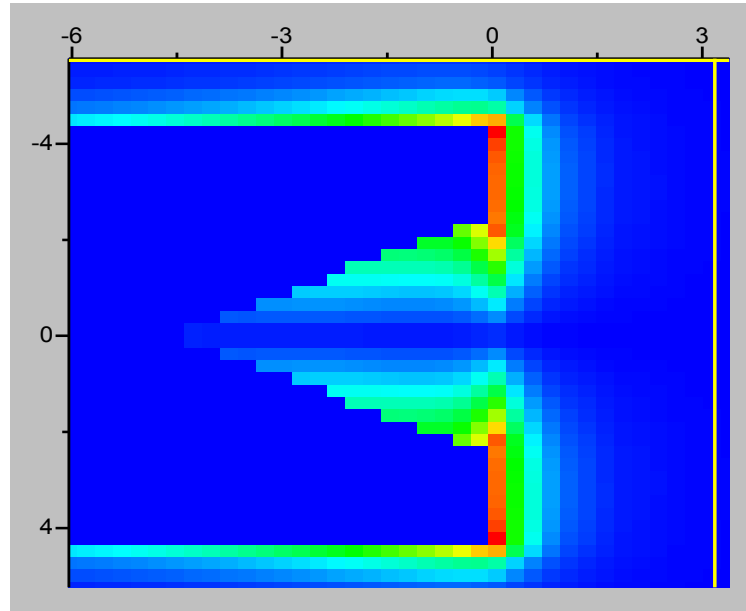


Figure 4.18 Electrical field distributions on the TSA

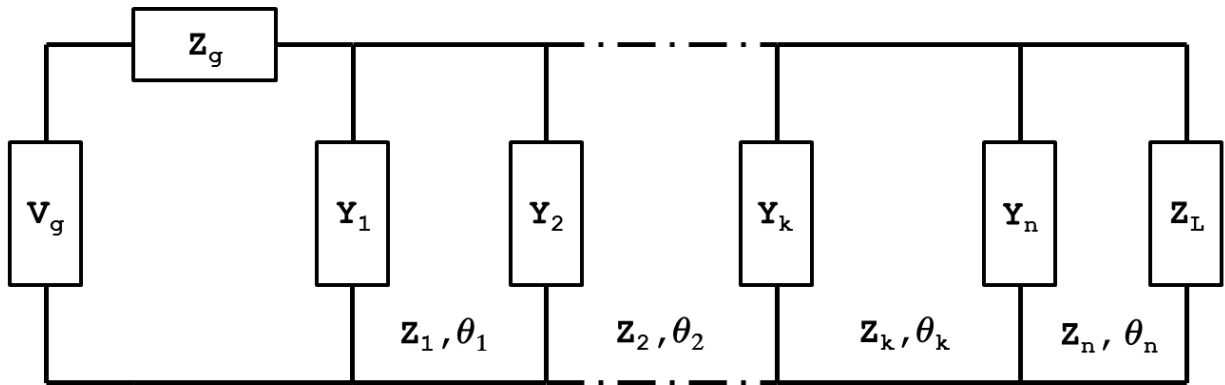
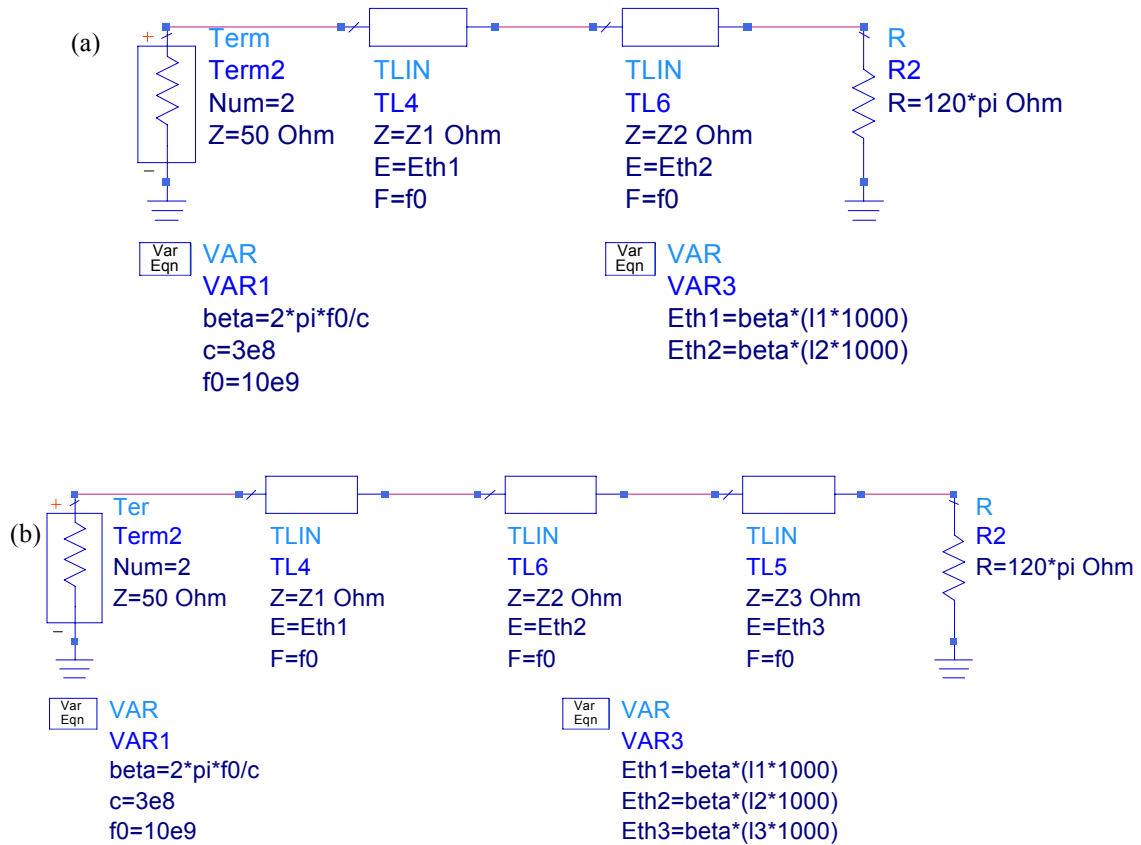


Figure 4.19 Equivalent circuit of the step line



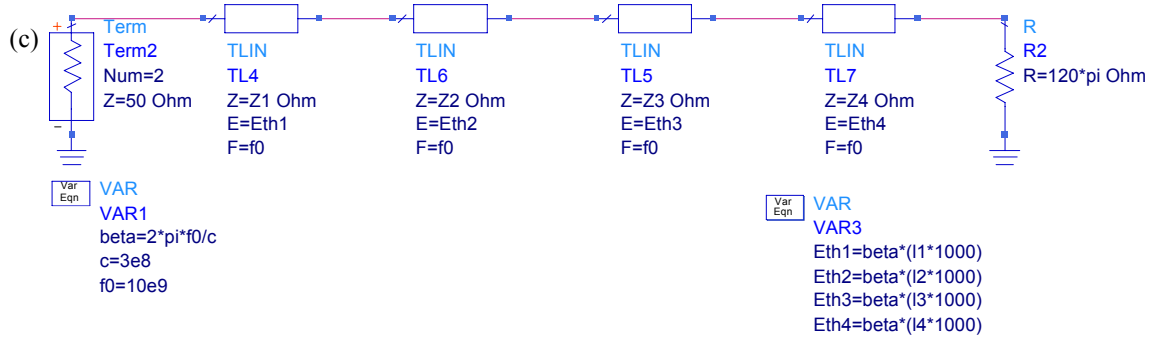


Figure 4.20 (a) Two-TLIN model of a TSA (b) Three-TLIN model of a TSA  
(c) Four-TLIN model of a TSA

(a) Two-TLIN

Unit: mm

Z1	186.57
Z2	504
l1	3.95124
l2	0.7488

g1	3.7
g2	5.2
l1'	1.8944
l2'	0.5012

(b) Three-TLIN

Z1	50
Z2	135
Z3	430
l1	1.39376
l2	2.87257
l3	3.09084

g1	0.055
g2	0.8
g3	4.4
l1'	0.5695
l2'	1.2998
l3'	1.5676

(C) Four-TLIN

Z1	59.2197
Z2	96.6004
Z3	223.685
Z4	457.106
l1	1.51943
l2	1.89764
l3	2.63293
l4	1.85544

g1	0.1
g2	0.41
g3	2.0
g4	4.8
l1'	0.6342
l2'	0.8386
l3'	1.2989
l4'	0.8507

Table4.4 Dimensions of slotline model of a TSA

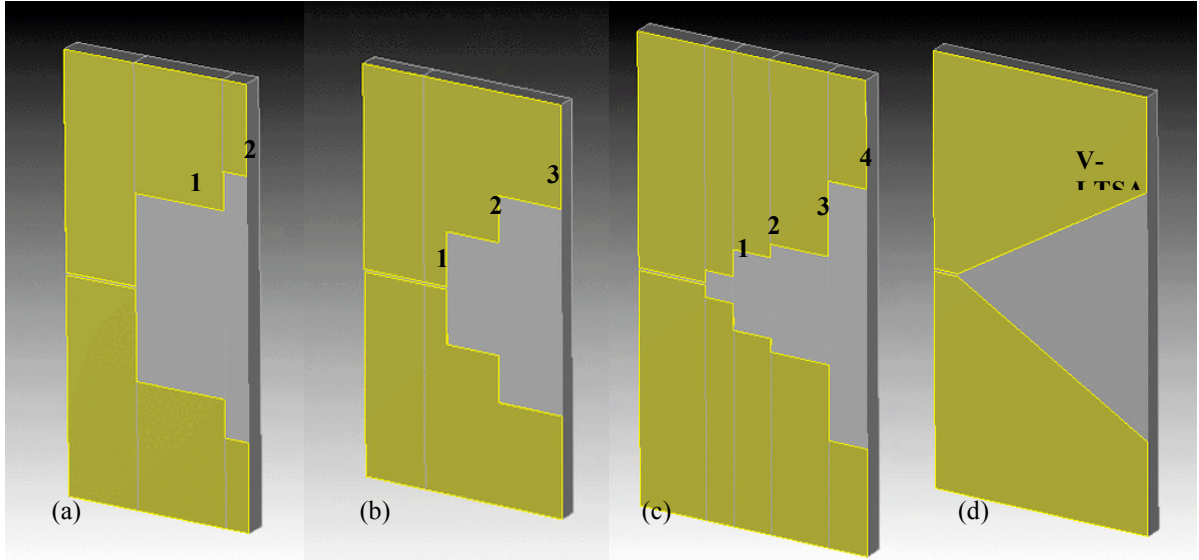


Figure 4.21 Schematic views of the TSA with increased transmission lines; (a) two section, (b) three section, (c) four section, (d) V-LTSA

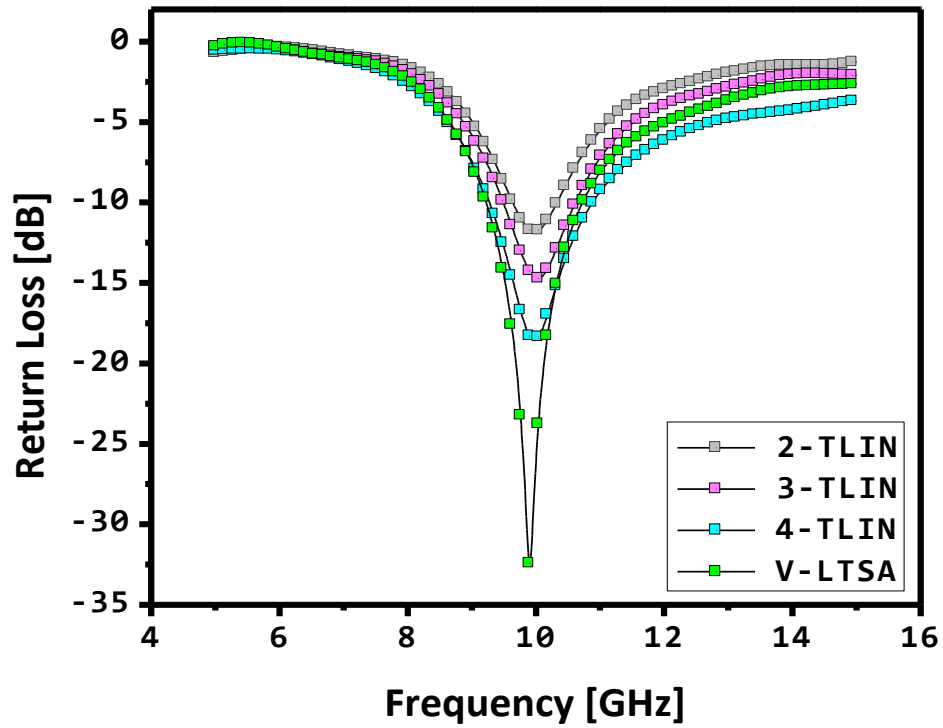


Figure 4.22 Return losses of the TLIN-modeled TSAs and the V-LTSA

## 4.5 Tapered slot antenna (TSA) with biasing lines

To incorporate with a QDMLL, the linearly tapered slot antenna (LTSA) is designed using ideal TLIN-models. The shape and detailed dimensions are presented in Figure 4.23 and Table 4.5. The LTSA is fed by a coplanar slot line with a 0.1-mm wide air gap. The corresponding characteristic impedance of a slot line with a 0.1-mm air gap is 50Ω at 10 GHz. The design goal is to make an antenna operate at 10 GHz and the operation of an antenna should not be affected by the biasing lines for the QDMLL. The biasing lines for a QDMLL are also shown in Figure 4.23. The biasing network is composed of the forward DC current ( $I_f$ ), reverse voltage ( $V_r$ ) and GND lines. The simulated input impedance ( $Z_{in}$ ) of the LTSA is presented in Figure 4.24. Based on the simulated result, the resonance frequency of an antenna is 10 GHz because of the  $\text{Imag}(Z_{in}) \cong 0$  and the  $\text{Real}(Z_{in}) \cong 50$  at 10 GHz.

The proposed LTSA is fabricated by the lithographic method. The measured return loss is compared to the simulated data. As shown in Figure 4.25, the two results agree well at the desired frequency.

After integration with the QDMLL, we measured the emitting power intensity out of the integrated module. As a receiving antenna, an X-band horn antenna was used. It rotated along  $-90^\circ < \phi < 90^\circ$  at the fixed  $\theta = 90^\circ$ . Figure 4.26 shows both the simulated directivity and measured emitting power intensity. The strongest radiation was achieved in the direction of  $\phi = 0^\circ$ ,  $\theta = 90^\circ$ . This is because the TSA produces radiation in the end-fire direction at the wider end of the slot [6].

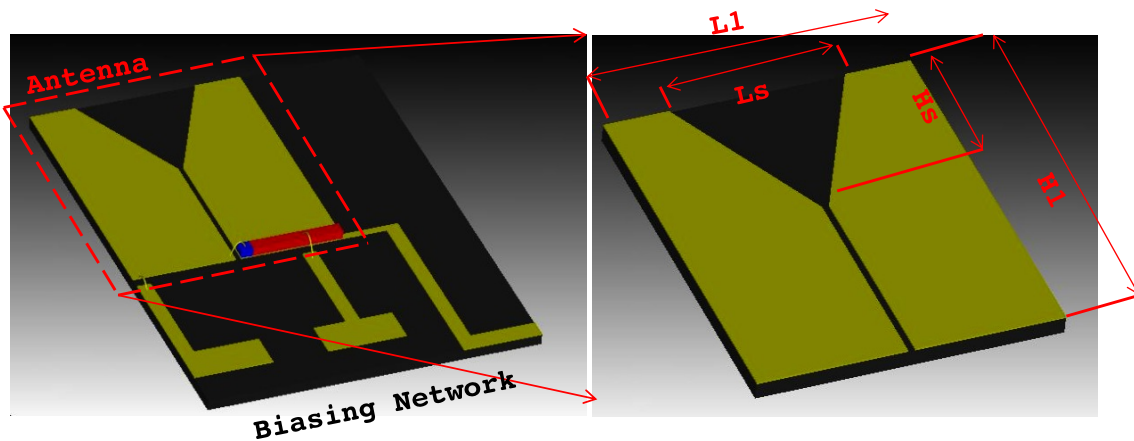


Figure 4.23 QDMLL-integrated-TSA module and the enlarged view of a TSA

---

Unit: mm	
L1	8.8
Ls	4.9985
H1	10.5
Hs	4.667

---

Table 4.5 Detail dimensions of a TSA

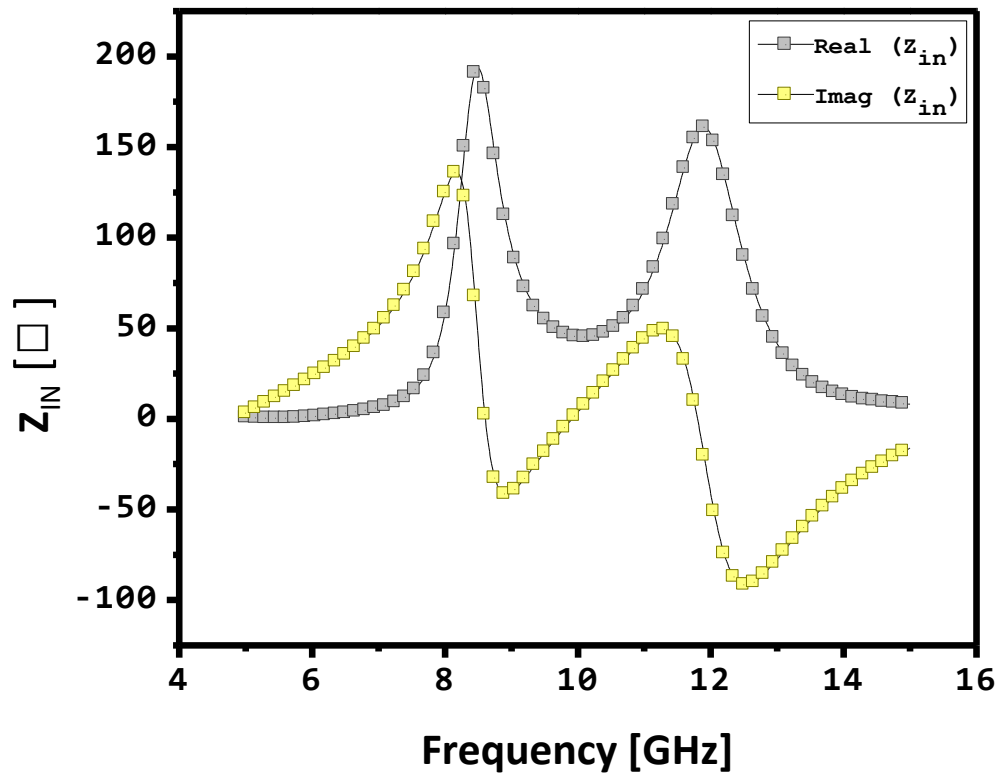


Figure 4.24 Input impedance ( $Z_{in}$ ) of the TSA

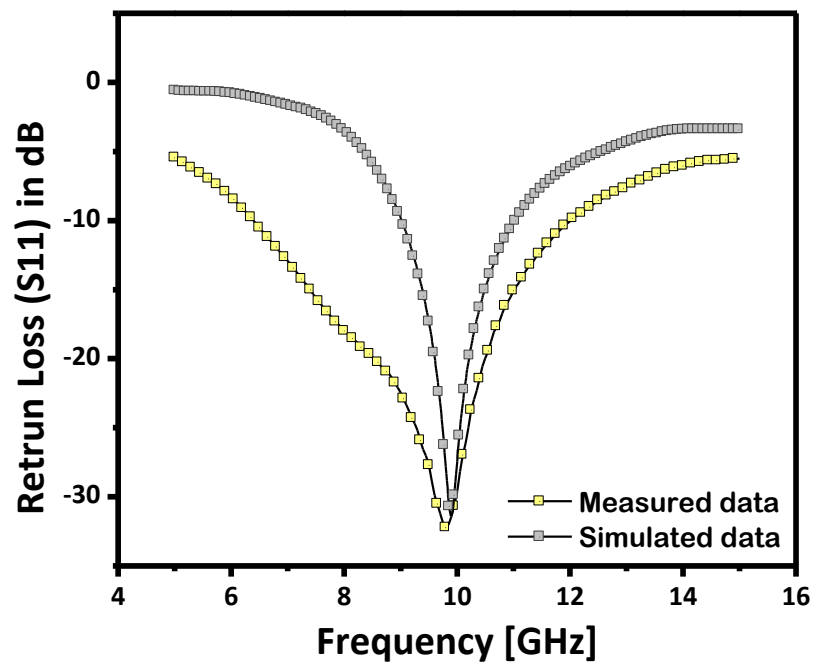


Figure 4.25 Measured and simulated return losses

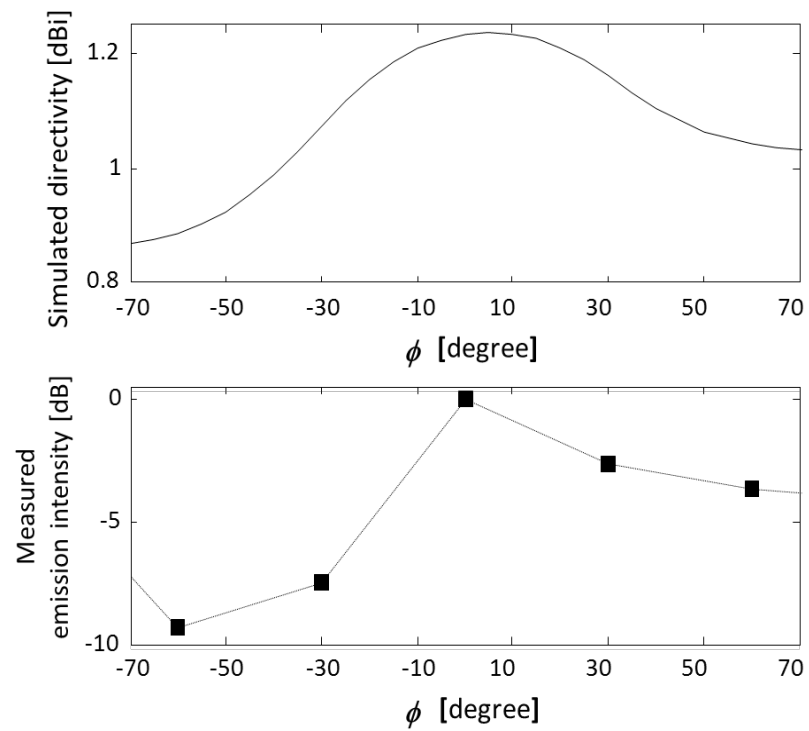


Figure 4.26 Simulated directivity and measured radiation intensity over  $-90^\circ < \phi < 90^\circ$



## 4.6 2 Element TSA array

Here, the design and operation of a two element linearly tapered slot-line antenna array is described. The antenna array was designed to achieve beam steering by manipulating the bias conditions of a QDMLL. The common technique to achieve beam steering in array antennas is to differentiate the microwave signal out of the power sources by implementing phase shifters such as phase delay lines [7-9]. To this end, an external phase controller such as a phase delay line or phase shifter is required. External phase controllers have been well developed and investigated. Yet, the power consumption and the enlarged size of an array are inevitable. Of particular interest are the QDMLLs because they are capable of generating photocurrents of different phases by manipulating the reverse voltage bias on the absorber. The detail theory of phase variation of output photocurrent was previously explained in Section 2. A two element phased tapered slot antenna array was fabricated and integrated with two identical QDMLLs.

To design an array system, the interval distance ( $d$ ) of two adjacent elements needs to be decided. The distance affects its radiation property. If the distance is chosen too small, its mutual coupling between two elements can deteriorate the desirable radiation pattern [10-12]. In order to choose the proper distance ( $d$ ), the  $S_{21}$ s of various distances are simulated. The result in Figure 4.27 shows that the mutual coupling of the two antenna elements gets smaller as the distance of separation gets larger. Although the lower  $S_{21}$  is preferable for better array performance, the array size is also a limitation. As a compromise, the smallest distance that satisfies  $S_{21} < -15$  [dB] was chosen. The first fabricated prototype of a phased antenna array is shown in Figure 4.28. Each bias line is designed to have a very high impedance at 10 GHz so that the excited signal can only propagate into the array module and not on the bias lines so they do not radiate as well. The fabricated prototype of the QDMLL-integrated-TSA array is shown in Figure 4.29. Two identical QDMLLs are directly mounted onto a co-planar ground side of the TSA and the absorber is wire-bonded to the other metal-side of the TSA. To have solid bondage between the QDMLLs and the antenna array, a thick ( $> \sim 5$ mm) titanium layer is deposited on top of the co-planar ground.

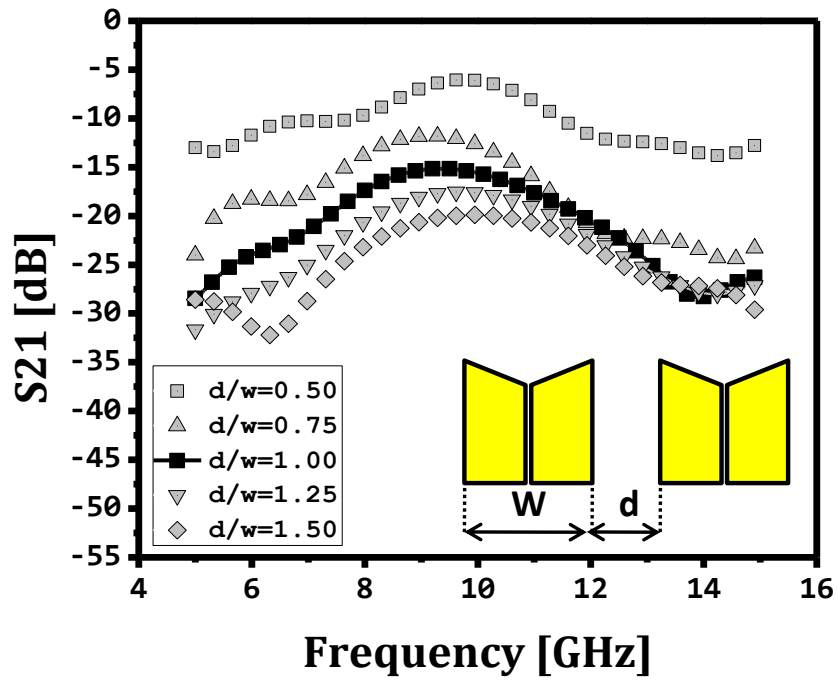


Figure 4.28 S21-simulation of the 2 element TSA array as increasing the interval distance

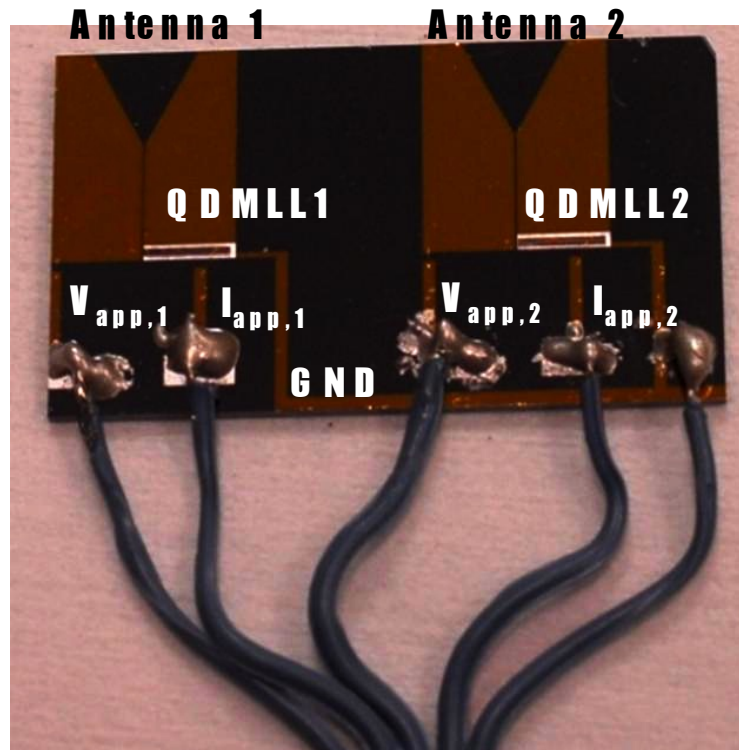


Figure 4.29 Photo-image of the fabricated QDMLL-integrated-LTSA array

## 4.7 Beam-steering experiment

The radiation measurement setup is shown in Figure 4.30. In this setup, the array of TSAs, as the transmitter, is located in the center of the chamber. As the receiving antenna, an X-band horn antenna is mounted on the rotating post controlled by a stepper motor. The scanned RF spectrum of the emitted electrical field is monitored by an electrical spectrum analyzer. All power supplies are placed outside of the chamber so that undesired scattering fields can be minimized. The phase and magnitude of the output photocurrents are controlled by means of manipulating the current and voltage bias on the QDMLL. The placement of the antenna in the anechoic chamber is shown in Figure 4.31. The distance between the transmitter and receiver is approximately 10 cm.

To achieve beam-steering, two different bias conditions are applied to the QDMLLs. The first bias condition, 150-mA DC current and -2-V voltage were applied to both QDMLLs. In the second bias case, 150-mA DC current and -2 V voltage were applied on the QDMLL 1 and 150-mA DC current and +0.5 V voltage were applied to the QDMLL2. In Figure 4.32, the output phase angle of each QDMLL is measured and presented. The resulting phases for the application of -2V and +0.5V are  $21.7^\circ$  and  $12.6^\circ$ , respectively. Thus, the phase angle difference of the two cases is  $9.1^\circ$ . In Figure 4.33, two maximum emitting power intensities are measured. For the first biasing case, the angle for the maximum power intensity is  $-10^\circ$ . The maximum value for the second biasing condition is measured at  $0^\circ$ .

In order to verify the measured result, the directivity of the TSA array is simulated in Figure 4.34. The simulation shows that the angle of the maximum directivity increases by changing the same angle degree in input signals. Both measured emission power-intensity and simulated directivity demonstrates that radiation beam pattern is tilted by means of applying different voltages.

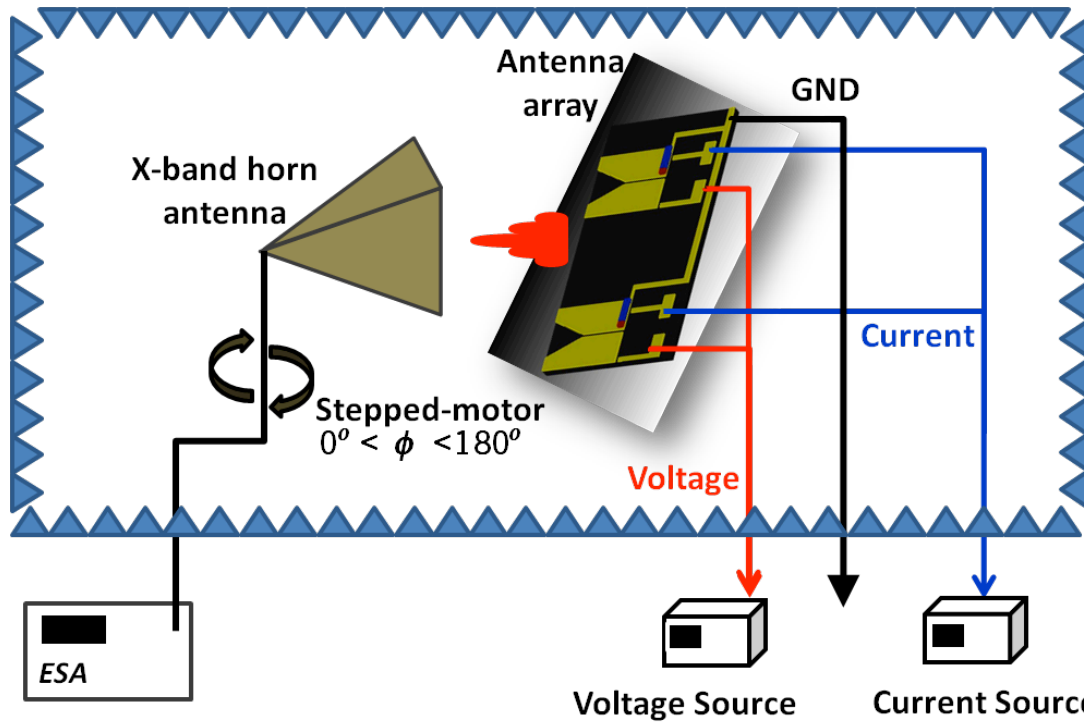


Figure 4.30 Experimental environment and schematics of a measurement setup for beam-steering.

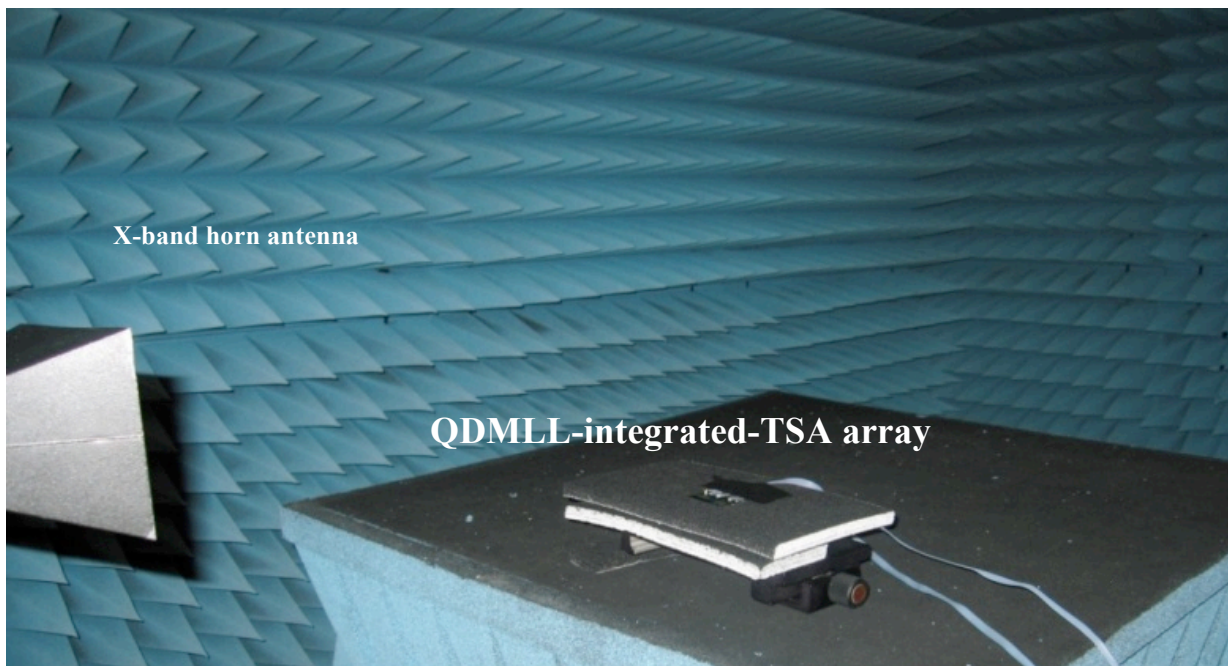


Figure 4.31 Anechoic chamber measurement setup

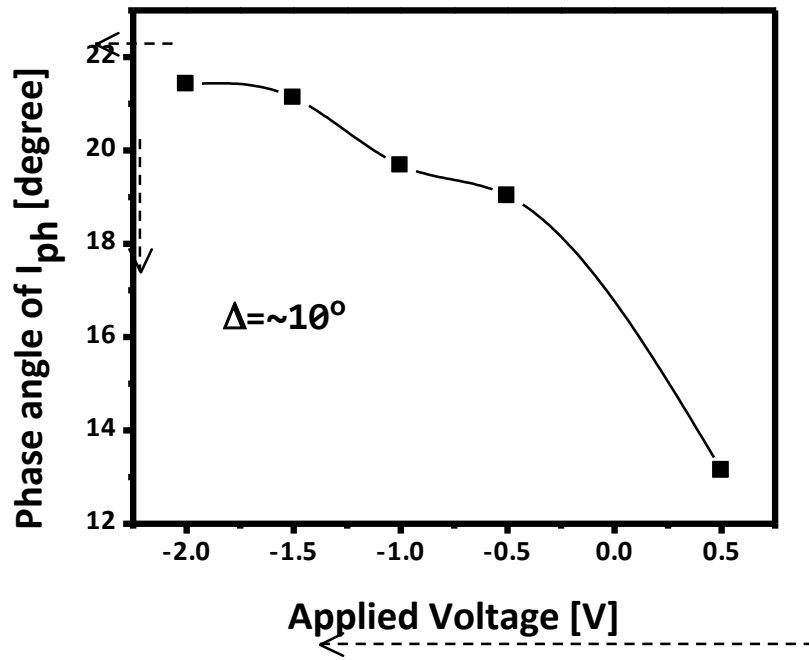


Figure 4.32 The measured output phase angle of a QDMLL as applied voltage.

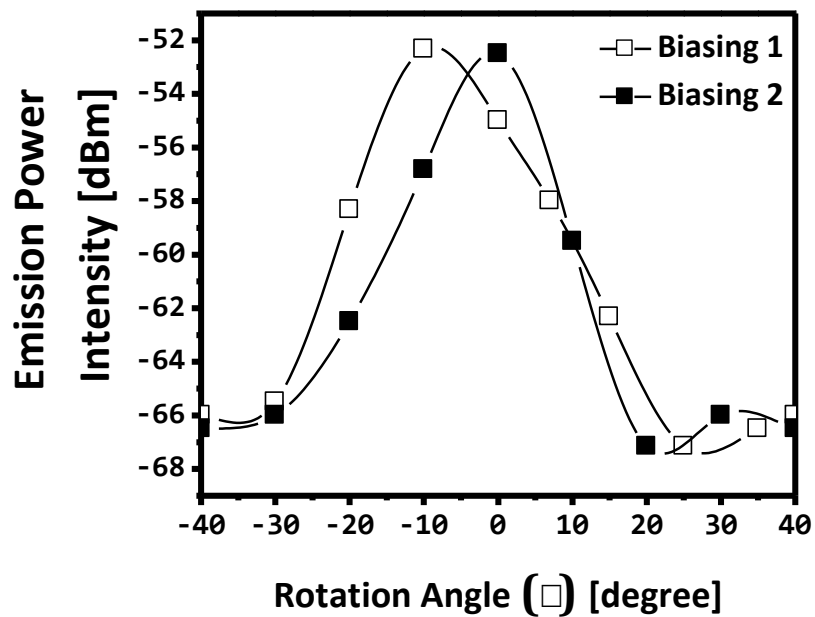
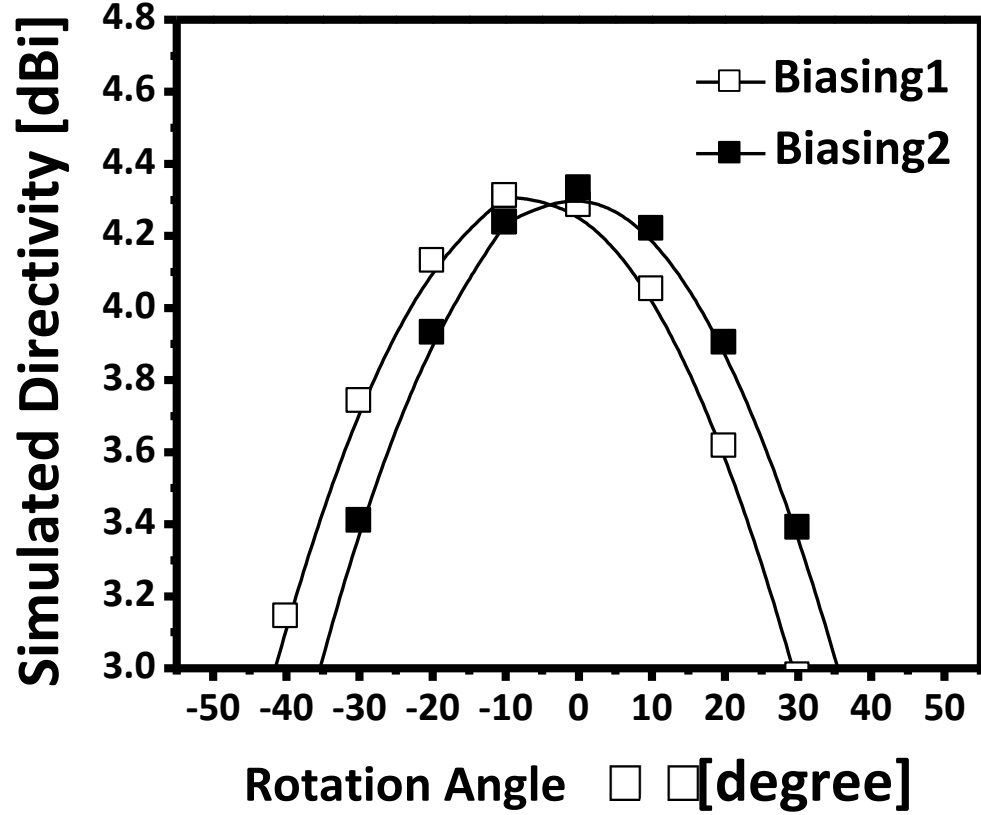


Figure 4.33 The measured emission power-intensity for different bias conditions.



Fig

ure 4.34The simulated directivity of a TSA array

## 4.8 Summary

A dual band bow-tie slot antenna is first designed, fabricated and tested. An impedance matching circuit is introduced to increase the radiation efficiency at the first and second order harmonics of the QDMLL; 10 and 20 GHz. Based on numerical computations, the antenna is able to have 5.17 dB-gain at 10 GHz and 3.63 dB-gain at 20 GHz.

In 4.2, beam-steering capabilities were clearly demonstrated using an integrated 2 element QDMLL-LTSA phased array by manipulating the laser bias conditions. To improve the efficiency of the antenna design, the LTSA was designed using the equivalent ideal transmission line model. The far-field measurement experiment in an anechoic chamber showed good agreement between measured and simulation results. With this novel technology the QDMLL demonstrated a potential as a good candidate in realizing a compact phased array system without the use of complicated delay lines and phase shifters.

## 5. Conclusions and Future work

### 5.1 Summary and Conclusions

In this work, the integration of a Quantum Dot Mode Locked Laser, that acts as a microwave and millimeter wave source, with a wideband antenna was presented. To this end, two aspects of research were discussed. The first aspect of this work dealt with the MLLs based on the quantum dot (QD) materials. Due to the unique properties of the QDs, the QDMLL can expand the range of stable mode-locking operation. The details on the MLL structure and operation mechanism are also discussed by experimenting on a two-section QDMLL. In order to gather photocurrent from the absorption section, forward currents are applied on the gain and reverse voltage-bias to the absorber.

The second aspect of this work was the realization of a compact transmitting antenna integrated to a QDMLL. For this purpose, several antenna prototypes were designed by using the two-port approach. The designed antennas were fabricated and integrated with laser chips using the lithographic method. The emitted power intensity and estimated pattern out of the fabricated prototypes were presented and discussed. Measurements on these integrated antennas showed a good agreement between simulation and experimental results. Moreover, the measured radiation generated by the QDMLL also confirms the proposed concept of the MLL as a possible compact microwave antenna source. To fully take advantage of a QDMLL, a bow-tie slot antenna was used. The challenge of designing a slot antenna is that the fabricated antenna should resonate at multiple harmonics of the QDMLL repetition rate.

Another important development for the QDMLL-integrated-antenna was to match the antenna impedance to the absorber impedance, which is the key for enhancing the radiation efficiency. With the proposed dual band impedance matching stub lines, the power gain to the load was improved by 5-dB at 10 GHz and 3-dB at 20 GHz, respectively.

Finally, an example of achieving beam-steering using a two-element QDMLL-LTSA phased array by manipulating the laser bias condition was presented and discussed. To improve the efficiency of the antenna design, the LTSA was designed using an equivalent ideal transmission line model. Up to  $10^\circ$ , beam steering was observed by simply handling the applied voltage bias on each QDMLL and without the use of any external phase shifters. The

far-field measurement performed in an anechoic chamber showed good agreement between measured and simulated results. With this technology, the proposed RF/Photonic antenna has the potential to be an attractive candidate in realizing a compact phased antenna array system by removing complicated delay lines and phase shifters.

## **5.2 Future work and recommendation**

The results of this work show that the amount of generated power of the QDMLL is limited. The power of photocurrents is in general in the order of mW. Although an impedance matching circuit has been implemented, the radiating power intensity is still not sufficient for practical applications. There are several possible approaches that can be used to increase the radiating power. At the MLL level, the generation of photocurrents can be increased by enhancing the optical-to-electrical conversion efficiency. A second approach is to use a power amplifier between the QDMLL and the antenna to amplify the signal from the MLL. This approach will give enough power to make the proposed design useful for practical applications where more power out of the antenna is required.

Another challenge in our research is producing higher repetition rates. Based on the discussion in Section 2, the repetition rate of QDMLLs is inversely related to the total cavity length. The shorter the cavity, the higher the repetition rate. However, the absorption of the signal out of the cavity is restricted by the size of the absorber. To resolve this limitation, the multisection QDMLL is suggested in section 2.4. It is useful not only for the high frequency pulse generation but also for generating a reconfigurable microwave source by manipulating its bias positions. The ultimate reconfigurable system is feasible by combining the multisection QDMLL with reconfigurable antennas.

Another area of future research that merits further attention is using the double interval approach to generate multiple harmonics in the cavity and extracting several RF frequencies simultaneously. This will require a more sophisticated design with a single or multiple antennas attached to the same QDMLL. The use of a power amplifier can be employed here as well.

If a single combination of QDMLL/antenna is to operate between 5 to 65 GHz and beyond, a wider broadband matching network will be required. This is not an easy task considering the fact that the matching network will have to be a planar structure that is



inherently narrowband.

Finally, although, it was demonstrated that beam steering and phase shifting can be achieved by manipulating the voltage bias condition of the attached QMLLs, the result was around 10 degrees. For practical application the beam steering angle has to go beyond the 10 degree point and at much higher frequencies.

## References

1. J. Genest, M. Chamberland, P. Tremblay, M. Tetu, "Microwave signals generated by optical heterodyne between injection-locked semiconductor lasers," *IEEE J. Quantum Electron.*, vol. 33, no. 6, pp. 989-998, Jun 1997.
2. M. A. Bernacil, S. O'Connor, B. Maher, A. Dekelaita, and D. Derickson, "Microwave Signal Generation Using Self-Heterodyning of a Fast Wavelength Switching SG-DBR Laser," *IEEE MTT-S International symposium*, pp. 603-606, Jun 2008.
3. A. Gubenko, D. Livshits, I. Krestnikov, S. Mikhlin, A. Kozhukhov, A. Kovsh, N. Ledentsov, A. Zhukov and E. Portnoi, "High-power monolithic passively modelocked quantum-dot laser", *ELECTRONICS LETTERS* 29th September 2005 Vol. 41 No. 20.
4. M. Passerini, M. Sorel and P.J.R. Laybourn, "Optimization and regime characterization of monolithic semiconductor mode-locked lasers and colliding-pulse mode-locked lasers at microwave and millimeter-wave frequency," *IEE Proc. Optoelectron.*, vol. 151, no. 6, pp. 508-512, Dec. 2004.
5. C.-Y. Lin, Y.-C. Xin, J. H. Kim, C. G. Christodoulou, and L. F. Lester, "Compact Optical Generation of Microwave Signals Using a Monolithic Quantum Dot Passively Mode-Locked Laser", *IEEE Photonics Journal*, vol. 1, no. 4, pp. 236-244, Oct. 2009.
6. S. Arahira and Y. Ogawa, "Polarization-insensitive all-optical 160-Gb/s clock recovery with a monolithic passively mode-locked laser diode in polarization-diversity configuration," *IEEE J. Quant. Electron.*, vol. 43, no. 6, pp. 1204-1210, Dec. 2007.
7. R. Kaiser and B. Huttel, "Monolithic 40-GHz mode-locked MQW DBR lasers for high-speed optical communication systems," *IEEE J. Selected Topics Quant. Electron.*, vol. 13, no. 1, pp. 125-135, Jan./Feb. 2007.
8. E. U. Rafailov, M. A. Cataluna, and W. Sibbett, "Mode-locked quantum-dot lasers", *Nature Photonics*, Vol. 1, 395 - 401, July 2007.
9. Y.-C. Xin, "Quantum Dot Multi-section light emitters", *Ph.D dissertation*, University of New Mexico, 2006.
10. U. Keller, "Recent developments in compact ultrafast lasers," *Nature* 424, 831-838, (2003).
11. J.H. Kim, C.G. Christodoulou, Z. Ku, Y.-C. Xin, N.A. Naderi, L.F. Lester, "Quantum-dot laser coupled bowtie antenna," *IEEE Int. Antennas and Propagation Symp.*, pp. 1-4, Jul. 2008.
12. J. H. Kim, C. G. Christodoulou, Z. Ku, C.-Y. Lin, Y.-C. Xin, N. A. Naderi, L. F. Lester, "Hybrid Integration of a Bowtie Slot Antenna and a Quantum Dot Mode-Locked Laser," *Antennas and Wireless Propag. Letters*, vol. 8, pp. 1337 - 1340, 2009.
13. A.J.C. Vieira, P.R. Herczfeld, A. Rosen, M. Ermold, E.E. Funk, W.D. Jemison, and K.J. Williams, "A mode-locked microchip laser optical transmitter for fiber radio", *IEEE Trans. Microw. Theory Tech.*, vol. 49, no. 10, 1882-1887 (2001).
14. J.H. Kim, C.G. Christodoulou, Z. Ku, Y.C. Xin, N.A. Naderi, L.F. Lester, "Quantum-dot laser coupled bowtie antenna," *IEEE AP-S*, pp. 1 - 4 (2008).
15. D.J. Derickson, R.J. Helkey, A. Mar, J.G. Wasserbauer, and J.E. Bowers, "Microwave and millimetre-wave signal generation using modelocked semiconductor lasers with intrawaveguide saturable absorbers," *Proc. of IEEE Int. Symp. on Microwave Theory and Techniques*, pp. 753-756 (1992).
16. C.-Y. Lin, Y.-C. Xin, J.H. Kim, C.G. Christodoulou and L.F. Lester, "Compact Optical Generation of Microwave Signals Using a Monolithic Quantum Dot Passively Mode-Locked Laser," *IEEE Photonics Journal*, Vol. 1, no. 4, pp. 236-244, Oct. 29 (2009).

17. E.U.Rafailov, M.A.Cataluna, W.Sibbett, "Mode-locked quantum-dot lasers," *Nature Photonics* 1, 395-401, (2007).
18. M. G. Thompson, A. R. Rae, M. Xia, R. V. Penty, and I. H. White, "InGaAs quantum-dot mode-locked laser diodes," *IEEE J. Sel. Top. Quantum Electron.* 15, 661-672, (2009).
19. Y.-C. Xin, Y. Li, V. Kovanis, A. L. Gray, L. Zhang, and L. F. Lester, "Reconfigurable quantum dot monolithic multi-section passive mode-locked lasers," *Opt. Express* 15 7623-7633 (2007).
20. A.H.Steinbah, I. Penn, N. Chokshi, D. Martin, K. Slomkowski, W. Baun, N. Agrawal, R.Ben-Michael, M.A. Itzler, "Equivalent circuit modeling of p-i-n photodiodes for 40 Gb/s receivers," *LEOS 2002. IEEE*, Vol. 2, pp. 486 – 487(2002).
21. Y.-C. Xin, Y. Li, V. Kovanis, A. L. Gray, L. Zhang, and L. F. Lester, "Reconfigurable quantum dot monolithicmultisection passive mode-locked lasers", *Opt. Express*, 15, 7623-7633 (2007)
22. Y. Li, F. L. Chiragh, Y.-C. Xin, C.-Y. Lin, J.-H. Kim, C.G. Christodoulou, L.F. Lester,"Harmonic mode-locking using the double interval technique in quantum dot lasers," *Opt. Express*, 18 (14), 14637-14642 (2010).
23. J. H. Kim, C. G. Christodoulou, Z. Ku, Y.-C. Xin, N. A. Naderi, and L. F. Lester, "Quantum-dot laser coupled bowtie antenna", AP-S 2008. IEEE, 5-11 July 2008 Page(s):1 – 4
24. R.C. Compton, R.C. McPhedran, Z. Popovic, G.M. Rebeiz, P.P. Tong, and D.B. Rutledge, "Bow-Tie antennas on a dielectric half-space: Theory and Experiment," *IEEE Transaction, Antennas and Propagation*, Vol. 35, pp 622-631, February, 1987
25. E. Chen, S.Y. Chou, "Characteristics of Coplanar Transmission Lines on Multilayer Substrate: Modeling and Experiments," *IEEE Transactions on Microwave Theory and Techniques*, Vol. 45, No. 6, June 1997.
26. CST Studio Suite 2010 ([www.cst.com](http://www.cst.com)).
27. A. W. Smith, "The electrical conductivity of Indium and Thallium," *The Ohio Journal of Science*, Vol. XVI, No. 6, pp 244 – 247, April 1916.
28. Advanced Design System (ADS), ([www.home.agilent.com/agilent](http://www.home.agilent.com/agilent)).
29. E. Michielssen, S. Ranjithan, R. Mittra,"Optimal multilayer filter design using real coded genetic algorithms," *Optoelectronics, IEE Proceeding*, Vol. 139, Issue no. 6, pp. 413 – 420, Dec., 1992
30. P. J. Gibson, "The Vivaldi aerial," in *Proc. 9th Eur. Microwave Conf.*, Brighton, U.K., Jun. 1979, pp. 101–105.
31. K. S. Yngvesson, "Endfire tapered slot antennas on dielectric substrates," *IEEE Trans. Antennas Propagat.*, vol. 33, no. 12, pp.1392–1400,1985.
32. H. Oraizi, S. Jam, "Optimum design of tapered slot antenna profile," *IEEE Trans. Antennas Propagat.*, vol. 51, no. 8, pp.1987–1995, Aug. 2003.
33. K.S. Yngvesson, T.L. Korzeniowski, Y.-S. Kim, E.L.Kollberg, J.F.Johansson,"The tapered slot antenna-a new integrated element for millimeter-wave applications," *IEEE Trans. Microw.Theory Tech.*, vol. 37, no.2, pp. 365 - 374, Aug. 2002.
34. E. Ojefors, Cheng. Shi,K. From, I. Skarin, P.Hallbjorner, A. Rydberg, "Electrically Steerable Single-Layer MicrostripTraveling Wave Antenna With Varactor DiodeBased Phase Shifters," *IEEE Trans. Antennas Propagat.*, vol. 55, no. 9, pp. 2451 - 2460, 2007.

35. M.A.Y. Abdalla, K.Phang, G.V.Eleftheriades, "A Planar Electronically Steerable Patch Array Using Tunable PRI/NRI Phase Shifters," *IEEE Trans. Microw.Theory Tech.*, vol. 57, no.3, pp. 531–541, 2009.
36. M.Y.-W. Chia, T.-H. Lim, J.-K. Yin, P.-Y. Chee, S.-W. Leong, C.-K. Sim, "Electronic Beam-Steering Design for UWB Phased Array," *IEEE Trans. Microw.Theory Tech.*, vol. 54, no.6, pp. 2431 - 2438, Jun. 2006.
37. Hoi-Shun Lui, Hot Tat Hui, MookSeng Leong, "A Note on the Mutual-Coupling Problems in Transmitting and Receiving Antenna Array,"*IEEE Mag. Antennas Propagat.*, vol. 51, no. 5, pp. 171 – 176, Oct. 2009.
38. Jing Zhao, Yueheng Li, Guishuang Sun, "The Effect of Mutual Coupling on Capacity of 4-Element Squared Antenna Array MIMO Systems,"WiCom '09. 5<sup>th</sup> International Conference, pp. 1-4, Sept. 2009.
39. T. Mbarek, Gharsallah, "Mutual coupling in phased array for 3X4 Butler Matrices antenna network,"*Int.Signals, Circuit and Systems*, 2008, pp. 1-5, Nov.2008.

## 6. Personel, Publications, Interactions,

### Personell

Dr. Christos Christodoulou	Professor and PI ( EM Simulation)
Dr. Luke Lester	Professor and Co-PI (photonics)
Mr. J. H. Kim	PhD. Student
Mr. C.Y. Lin	Ph.D. Student
Mr. N. A. Naderi	Ph.D. Student
Georgios Atmatzakis	M.S. Student

### Publications

#### A. Journal Papers

J. H. Kim, C. G. Christodoulou, Z. Ku, C.-Y. Lin, Y.-C. Xin, N. A. Naderi, and L. F. Lester, “Hybrid Integration of a Bowtie Slot Antenna and a Quantum Dot Mode-Locked”, *IEEE Antennas and Wireless Propagation Letters*, vol. 8, pp. 1337-1340, 2009.

C.-Y. Lin, Y.-C. Xin, J. H. Kim, C. G. Christodoulou, L. F. Lester, “Compact optical generation of microwave signals using a monolithic quantum dot passively mode-locked laser”, *IEEE Photonics Journal*, vol. 1, no. 4, pp. 236-244, Oct. 2009.

Yan Li, Furqan L. Chiragh, Yong-Chun Xin, Chang-Yi Lin, Christos G. Christodoulou, and Luke. F. Lester, “Harmonic mode-locking using the double interval technique in quantum dot lasers”, *Optics Express*, vol. 18(14), pp. 14637-14643, 2010.

J. H. Kim, C. G. Christodoulou, C.-Y. Lin, and L. F. Lester, “Pattern Estimation of a Microstrip Antenna Integrated With a Quantum Dot Mode-Locked Laser”, *IEEE Antennas and Wireless Propagation Letters*, vol. 9, pp. 954-957, 2010.

C.-Y. Lin, F. Grillot, Y. Li, R. Raghunathan, and L. F. Lester, "Characterization of timing jitter in a 5 GHz quantum dot passively mode-locked laser," *Optics Express* 18(21), pp. 21932-21937 (2010).

C.-Y. Lin, F. Grillot, N. A. Naderi, Y. Li, and L. Lester, “ rf linewidth reduction in a quantum dot passively mode-locked laser subject to external optical feedback”, *Applied Physics Letters*, vol. 96, pp. 51118 - 051118-3, 2010.

C.-Y. Lin, F. Grillot, N. A. Naderi, Y. Li, J. H. Kim, C. G. Christodoulou, and L. F. Lester, “RF Linewidth of a Monolithic Quantum Dot Mode-Locked Laser Under Resonant Feedback”, *IET Optoelectronics*, vol. 5, no. 3, pp.105–109 , June 2011.

C.-Y. Lin, F. Grillot, N.A. Naderi, Y. Li, R. Raghunathan, and L.F. Lester, "Microwave Characterization and Stabilization of Timing Jitter in Quantum-Dot Passively Mode-Locked

Laser via External Optical Feedback," *IEEE J. Special Topics Quantum Electron.*, vol. 17, no. 5, pp. 1311-1317 (2011).

## **B. Papers in Conference Proceedings**

J. H. Kim, C. G. Christodoulou, Z. Ku, Y.-C. Xin, N. A. Naderi, L. F. Lester, "Quantum-Dot Laser Coupled Bowtie Antenna", IEEE AP Symposium in San Diego, CA, July 2008 .

J. H. Kim, C. G. Christodoulou, Z. Ku, C.-Y. Lin, Y.-C. Xin, N. A. Naderi, L. F. Lester, J. P. Kim, "Quantum-dot mode locked laser integrated bowtie antenna", EUCAP, Berlin, March 2009, pp 2799-2802.

C.-Y. Lin, N. A. Naderi, F. Chiragh, J. H. Kim, C. G. Christodoulou and L. F. Lester, " 31% DC to RF Differential Efficiency Using Monolithic Quantum Dot Passively Mode-Locked Lasers", CLEO, Baltimore, Maryland , May-June 2009,.

J.H. Kim, C. G. Christodoulou, Z. Ku, C.-Y. Lin, N. A. Naderi, L. F. Lester and J. P. Kim, "A Bowtie Slot Antenna coupled to a Quantum-Dot Mode Locked Laser", IEEE AP URSI Symposium, Charleston, South Carolina, June 2009.

L. F. Lester, C.-Y. Lin, Y. Li, J. H. Kim and C. G. Christodoulou, "Reconfigurable, Multi-Section Quantum Dot Mode-Locked Lasers, CLEO/QELS 2010, May 2010.

(Invited Paper) L. F. Lester, C.-Y. Lin, Y. Li, J. H. Kim and C. G. Christodoulou, "Reconfigurable, Multi-Section Quantum Dot Mode-Locked Lasers, CLEO/QELS 2010, May 2010.

J. H. Kim and C. G. Christodoulou, "A simple reconfigurable microstrip antenna for wideband applications", IEEE AP URSI Symposium, Toronto, Canada, July 2010.

J-H. Kim, C-Y. Lin, Yan. Li, N. Naderi, C. G. Christodoulou, and L. F. Lester, "Beam Steering of a Linearly Tapered Slot Antenna Array Integrated with Quantum Dot Mode Locked Lasers", the 23rd Annual Meeting of the IEEE Photonics Society, Denver, Colorado, Nov. 2010

G. Atmatzakis, C. G. Christodoulou, D. Murell, and L. F. Lester, "RF Power Extraction from a Quantum Dot Mode Locked Laser Connected to an Antenna", *IEEE International Symposium on Antennas and Propagation*, Chicago, July 2012.

## **Interactions**

We have participated in several conference and meetings both in the Photonics community and the Antennas/RF community. The conference papers presented are listed above.

Locally we interacted with AFRL by having several meetings and discussion with Jim Lyke,

Steve Lane and Scott Erwin on various reconfigurable circuits and antennas.

On the photonic side we have interacted with Vassilios Kovanis at Wright Patterson.

We have also been involved with setting up the AFOSR's 2010 DCT workshop on "Reconfigurable Systems" Albuquerque. This allowed to bring researchers from all over the US for 2 days to discuss some new ideas in the field of reconfigurable photonics and electronics.

## **Recognition**

Prof. Lester won the SPIE 2012 Harold E. Edgerton award

Professor Christodoulou was selected as the IEEE Educator of the year 2012 from the Albuquerque Section.

Professor Christodoulou received the John Kraus Antenna 2010 APS Award

## **New Discoveries, Inventions, Patents**

None.

## 7. Appendix A (Selected publications)

### I. Characterization of timing jitter in a 5 GHz quantum dot passively mode-locked laser

Chang-Yi Lin<sup>1,\*</sup>, Frederic Grillot<sup>2</sup>, Yan Li<sup>1</sup>, Ravi Raghunathan<sup>1</sup> and Luke F. Lester<sup>1</sup>

<sup>1</sup>Center for High Technology Materials, University of New Mexico, 1313 Goddard SE, Albuquerque, NM 87106, USA

<sup>2</sup>Université Européenne de Bretagne, INSA, CNRS- Laboratoire FOTON, 20 avenue des buttes de Coesmes, 35708 Rennes, Cedex 7, France

\*[cylin@unm.edu](mailto:cylin@unm.edu)

**Abstract:** The timing jitter performance of a 5 GHz quantum dot passively mode-locked laser is investigated at different harmonics in the RF spectrum. The necessity of measuring the phase noise at relatively large harmonic numbers is motivated experimentally in the context of determining the corner frequency, its correlation to the RF linewidth, and the related white noise plateau level. The single-sideband phase noise with an integrated timing jitter of 211 fs (4-80 MHz) is reported. An all-microwave technique has been used to determine a pulse-to-pulse rms timing jitter of 96 fs/cycle. This low timing jitter value makes the chip-scale quantum dot mode-locked laser an attractive source for low noise applications such as optical clocking and sampling.

©2010 Optical Society of America

**OCIS codes:** (140.4050) Mode-locked lasers; (140.5960) Semiconductor lasers; (250.5590) Quantum-well, -wire and -dot devices

#### References and Links

1. G. Carpintero, M. G. Thompson, R. V. Penty, and I. H. White, "Low noise performance of passively mode-locked 10-GHz quantum dot laser diode," *IEEE Photon. Technol. Lett.* **21**, 389-391 (2009).
2. A. Akrouf, A. Shen, A. Enard, G.-H. Duan, F. Lelarge, and A. Ramdane, "Low phase noise all-optical oscillator using quantum dash modelocked laser," *Electron. Lett.* **46**, 73-73 (2010).
3. S. Breuer, W. Elsaer, J. G. McInerney, K. Yvind, J. Pozo, E. A. J. M. Bente, M. Yousefi, A. Villafranca, N. Vogiatzis, J. Rorison, "Investigations of Repetition Rate Stability of a Mode-Locked Quantum Dot Semiconductor Laser in an Auxiliary Optical Fiber Cavity," *IEEE J. Quantum Electron.* **46**, 150-157 (2010).
4. M. G. Thompson, D. Larsson, A. Rae, K. Yvind, R. V. Penty, I. H. White, J. Hvam, A. R. Kovsh, S. Mikhlin, D. Livshits, and I. Krestnikov, "Monolithic hybrid and passive mode-locked 40 GHz quantum dot laser diodes," *Proc. Eur. Conf. Opt. Commun. (ECOC)*, 1-2 (2006).
5. E. U. Rafailov, M. A. Cataluna, and W. Sibbett, "Mode-locked quantum-dot lasers," *Nat. Photonics* **1**, 395-401 (2007).
6. M. G. Thompson, A. R. Rae, M. Xia, R. V. Penty, and I. H. White, "InGaAs quantum-dot mode-locked laser diodes," *IEEE J. Sel. Top. Quantum Electron.* **15**, 661-672 (2009).
7. Y.-C. Xin, Y. Li, A. Martinez, T. J. Rotter, H. Su, L. Zhang, A. L. Gray, S. Luong, K. Sun, Z. Zou, J. Zilko, P. M. Varangis, and L. F. Lester, "Optical gain and absorption of



- quantum dots measured using an alternative segmented contact method,” *IEEE J. Quantum Electron.* **42**, 725–732 (2006).
8. L. Zhang, L.-S. Cheng, A. L. Gray, H. Huang, S. Kutty, H. Li, J. Nagyvary, F. Nabulsi, L. Olona, E. Pease, Q. Sun, C. Wiggins, J. C. Zilko, Z. Zou, and P. M. Varangis, “High-power low-jitter quantum-dot passively mode-locked lasers,” *Proc. SPIE* **6115**, 611502 (2006).
  9. D. Von der Linde, “Characterization of noise in continuously operating mode-locked lasers,” *Appl. Phys. B: Photophys. Laser Chem.* **39**, 201–217 (1986).
  10. J. P. Tourrenc, A. Akrou, K. Merghem, A. Martinez, F. Lelarge, A. Shen, G. H. Duan, and A. Ramdane, “Experimental investigation of the timing jitter in self-pulsating quantum-dash lasers operating at 1.55  $\mu\text{m}$ ,” *Opt. Express* **16**, 17706–17713 (2008).
  11. D. Eliyahu, R. A. Salvatore, and A. Yariv, “Noise characterization of pulse train generated by actively mode-locked lasers,” *J. Opt. Soc. Am. B* **13**, 1619–1626 (1996).
  12. “The control of jitter and wander within the optical transport network,” Recommendation G.8251, ITU-T, (2001).
  13. D. Eliyahu, R. A. Salvatore, and A. Yariv, “Effect of noise on the power spectrum of passively mode-locked lasers,” *J. Opt. Soc. Am. B* **14**, 167–174 (1997).
  14. F. Kefelian, S. O'Donoghue, M. T. Todaro, J. G. McInerney, and G. Huyet, “RF linewidth in monolithic passively mode-locked semiconductor laser,” *IEEE Photon. Technol. Lett.* **20**, 1405–1407 (2008).
  15. T. Yilmaz, C. M. Depriest, A. Braun, J. H. Abeles, and P. J. Delfyett, “Noise in Fundamental and Harmonic Modelocked Semiconductor Lasers: Experiments and Simulations,” *IEEE J. Quantum Electron.* **39**, 838–849 (2006).
  16. C.-Y. Lin, F. Grillot, N. A. Naderi, Y. Li, and L. F. Lester, “rf linewidth reduction in a quantum dot passively mode-locked laser subject to external optical feedback,” *Appl. Phys. Lett.* **96**, 051118 (2010).
  17. C.-Y. Lin, F. Grillot, Y. Li, R. Raghunathan, and L. F. Lester, “Characterization of timing jitter in a quantum dot passively mode-locked laser at low offset frequency,” submitted to *IEEE Photonics Society Annual Conference* (2010).
  18. Y.-C. Xin, Y. Li, V. Kovanis, A. L. Gray, L. Zhang, and L. F. Lester, “Reconfigurable quantum dot monolithic multisection passive mode-locked lasers,” *Opt. Express* **15**, 7623–7633 (2007).
- 

## 1. Introduction

Effective and compact semiconductor passively mode-locked lasers (MLLs) have been attracted plenty of attention due to the demand of ultra-low phase noise optoelectronic oscillators for optical signal processing applications [1–4]. These applications include high speed optical sampling, all-optical clock recovery and clock distribution. Quantum dot (QD) materials offer several potential advantages to improve the timing jitter performance of a passive MLL, such as reduced internal loss, low spontaneous emission noise, and low linewidth enhancement factor. [5,6]. However, in contrast to active mode-locking, the timing stability issue (nonstationary processes) is the main disadvantage of passive MLLs due to the lack of an external reference source. Since timing fluctuations in the optical pulse train play an important role in determining the laser performance, it is crucial that the jitter characterization in a passive MLL be studied more thoroughly.

In this paper, we experimentally characterize the corner frequency and low-frequency plateau level in the phase noise of a nonstationary monolithic two-section passive QD MLL operating with a nominal 5 GHz repetition rate. The device exhibits a state-of-art integrated

timing jitter value of 211 fs (4-80 MHz) and a pulse-to-pulse root mean square (rms) timing jitter of 96 fs/cycle for a 5 GHz passive QD MLL.

## 2. Device structure and fabrication

The QD structure investigated in this work was grown by elemental source molecular beam epitaxy on an  $n^+$ -doped (100) GaAs substrate. The active region consists of six “Dots-in-a-Well” (DWELL) layers. In each layer, an equivalent coverage of 2.4 monolayer InAs QDs is confined approximately in the middle of a 10 nm  $\text{In}_{0.15}\text{Ga}_{0.85}\text{As}$  quantum well (QW) [7]. The epitaxial structure and waveguide design are displayed in Fig. 1(a). The 3- $\mu\text{m}$ -wide ridge-waveguide devices were etched by inductively coupled plasma (ICP) etching and planarized using benzocyclobutene (BCB). Ti/Pt/Au was then deposited to form the p-metal contact. The electrical isolation between the gain and absorber sections was provided by proton implantation with an isolation resistance of  $>10\text{ M}\Omega$ . After the substrate had been thinned and polished, a Ge/Au/Ni/Au n-metal contact was deposited on the backside of the  $n^+$ -GaAs substrate and annealed at  $\sim 380^\circ\text{C}$  for 1 minute to form the n-ohmic contact. The two-section QD passive MLLs were made with a total cavity length of 7.8-mm and a saturable absorber (SA) length of 1.1-mm. The nominal repetition rate of the QD MLL is 5 GHz. A highly reflective coating ( $R \approx 95\%$ ) was applied to the mirror facet next to the SA to create self-colliding pulse effects in the SA for pulse narrowing, and the output facet was cleaved ( $R \approx 32\%$ ). The devices were p-side-up mounted on AlN heatsink carriers. These chip-on-carriers were then packaged into an industry-standard 14-pin butterfly packages with a thermoelectric cooler (TEC) and a polarization-maintaining lensed fiber pigtail as shown in Fig. 1(b) [8]. The function of the packaged module is to reduce environmental noise and enhance mechanical stability. The fiber-coupled light-current (L-I) curve under -7 V reverse voltage bias condition at  $20^\circ\text{C}$  is displayed in Fig. 2. The inset is the optical spectrum showing the peak lasing wavelength at 1.33- $\mu\text{m}$  under a gain current of 90 mA and an SA reverse voltage of -7 V. The typical average powers emitted by these devices under mode-locking conditions at the end of the fiber pigtail are 1-2.5 mW. The pulse durations are on the order of 10 ps. The time-bandwidth product of the MLL typically ranges from 2 to 10.

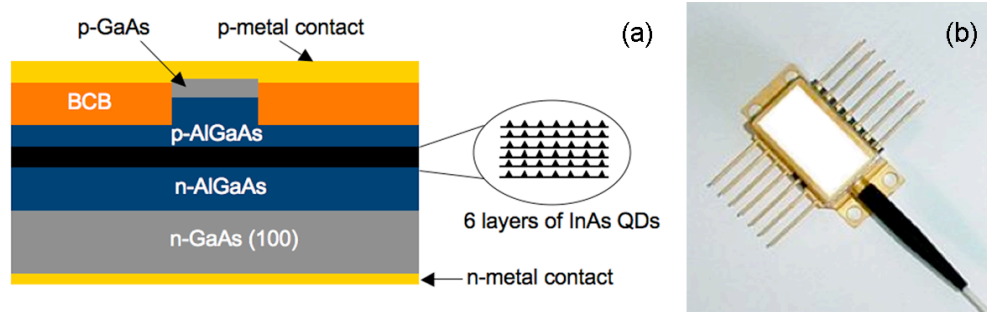


Fig. 1. (a) Schematic of the epitaxial layer structure of the InAs QD laser. (b) Picture of the passive QD MLL packaged module.

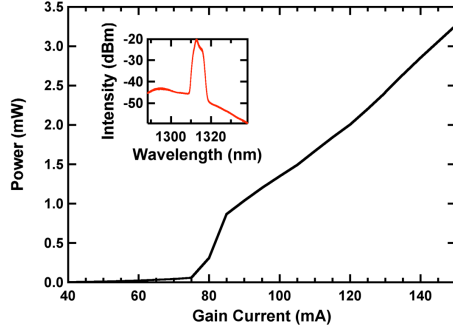


Fig. 2. L-I characteristic measured at 20°C for an absorber bias of -7 V. The inset shows the optical spectrum under 90 mA gain current and -7 V reverse voltage.

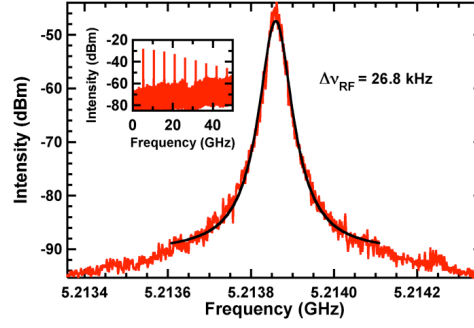


Fig. 3. RF linewidth of 26.8 kHz under 90 mA gain current and -7 V reverse voltage. The inset shows the full span RF spectrum at the same bias condition.

### 3. Characterization results and discussion

The rms timing jitter characterization is performed via a 45 GHz bandwidth photodiode coupled to an Agilent 8565EC electrical spectrum analyzer (ESA) that has a 50 GHz frequency range. Since above the corner frequency, the phase noise in our QD MLL scales with harmonic number, the rms timing jitter is calculated by integrating the single-sideband phase noise (SSB-PN) spectral density,  $L(f)$ , using the following expression: [9]

$$\sigma = \frac{1}{2\pi n f_R} \sqrt{2 \int_{f_{\min}}^{f_{\max}} L(f) df} \quad (1)$$

where  $n$  is the number of the harmonic at which the phase noise is measured,  $f_R$  is the repetition frequency, and  $f_{\min}$  and  $f_{\max}$  determine the offset frequency range over which the  $L(f)$  is integrated. In contrast to previous optical cross-correlation techniques [10], microwave data on the corner frequency and white noise plateau level across the 8 harmonics tested is used to calculate the pulse-to-pulse rms timing jitter [11].

The optimum 3-dB RF linewidth shown in Fig. 3 is 26.8 kHz under a 90 mA DC bias on the gain section and -7 V applied to the absorber. The inset shows the full-span RF spectrum at the same bias condition. The RF linewidth is confirmed with a Lorentzian curve fitting through the ESA with a resolution bandwidth of 1 kHz. Fig. 4(a) displays the SSB-PN spectra,  $L(f)$ , for different harmonics of the 5 GHz passive MLL device. The relatively low repetition rate of this monolithic passive MLL makes the characterization of higher order harmonics possible and all harmonics are phase noise dominated as confirmed in Fig. 4(b). Above the corner frequency, the phase noise trace shows the typical roll-off with a slope of -20 dBc/Hz per decade until it hits the thermal noise floor. For communication system applications, the MLL is to be used as a transmitter, where clock-recovery is performed in the receiver. Consequently, the jitter on a very long timescale will not matter, as this will be trivially tracked by the clock-recovery circuit. Integration of the SSB-PN using the ITU-T specified range gives a timing jitter of 390 fs at the 3<sup>rd</sup> harmonic order (4 MHz to 80 MHz) as shown in Fig. 4(c) [12]. The phase noise trace hits the thermal noise floor at the offset frequency of 9 MHz. Thus, extrapolating the trace from 9 MHz at the standard roll-off of -20 dBc/Hz per decade results in a timing jitter value of 211 fs, the lowest reported to date of a 5 GHz passive MLL. From the data presented in Fig. 4(a), the pulse-to-pulse rms timing jitter,  $\sigma_{pp}$ , can be calculated using the nonstationary passive MLL theory of Eq. (23) in [11]. The associated curve-fits to the 8 harmonics give an average  $\sigma_{pp}$  of 96±10 fs/cycle.

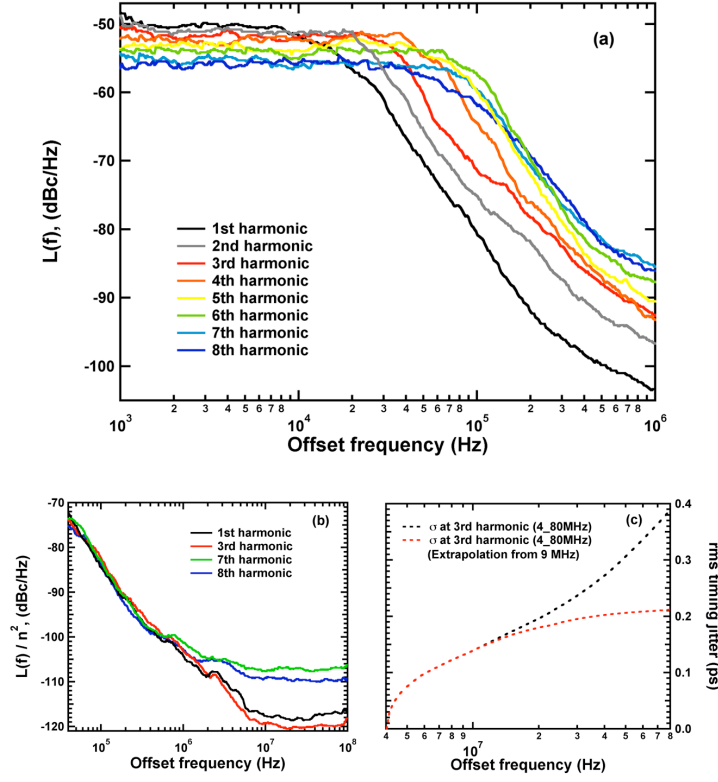


Fig. 4. (a) SSB-PN spectra density from different harmonics under 90 mA gain current and -7 V reverse voltage. (b) SSB-PN spectra density above the corner frequency normalized to  $n^2$  from different harmonics under the same bias condition as (a). (c) Timing jitter at the 3<sup>rd</sup> harmonic over the offset frequency range of 4 MHz to 80 MHz.

Further noise performance of the passive MLL is investigated at different bias conditions. Fig. 5(a) and (b) demonstrate the RF linewidth under -7 V applied to the absorber and 110 mA and 130 mA DC bias on the gain section, respectively. As seen in these figures, the RF linewidth broadens with increasing gain current to 95.4 (110 mA) and 294 kHz (130 mA), which implies that the pulse-to-pulse rms timing jitter should also rise [13,14]. The SSB-PN spectra at the 3<sup>rd</sup> harmonic under different bias currents and -7 V reverse voltage are shown in Fig. 6. It clearly demonstrates that the corner frequency increases from 14 kHz to 200 kHz to 1.6 MHz, as the gain current is raised from 90 mA to 110 mA and then 130 mA DC bias, respectively. Concurrently, the white-noise plateau does decrease since the total power of the oscillator has not changed much but the phase noise has broadened the spectral linewidth significantly. Thus, the corner frequency is a good figure-of-merit for MLLs regarding pulse timing stability. Here, it is empirically found from the data that the corner frequency varies as the square of the RF linewidth.

In contrast to actively mode-locked lasers [15], the pulse train timing stability issue is still the main disadvantage of passive MLLs due to the lack of an external reference source. However, several methods have been proposed to reduce the phase noise in passive MLLs such as injection locking or external optical feedback [2,3,16]. Under the resonant feedback condition, the RF linewidth can be reduced which results in a smaller jitter value than the free-running case. The feedback effect has also been observed to improve the corner frequency down to a lower offset frequency level [17]. The detailed investigation of the external feedback effect on SSB-PN spectra will be discussed in a future paper. Furthermore, hybrid

mode-locking techniques can also be used for lowering the white-noise plateau level of a MLL [1].

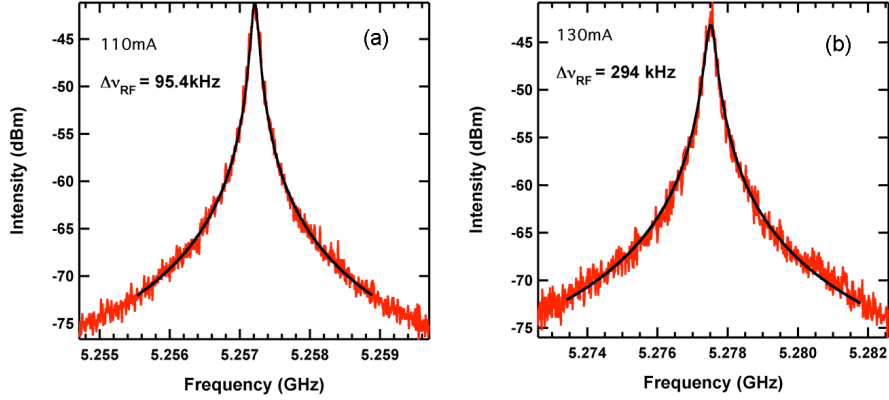


Fig. 5. (a) RF linewidth of 95.4 kHz under 110 mA gain current and -7 V reverse voltage. (b) RF linewidth of 294 kHz under 130 mA gain current and -7 V reverse voltage. The black curves represent the Lorentzian curve-fitting results.

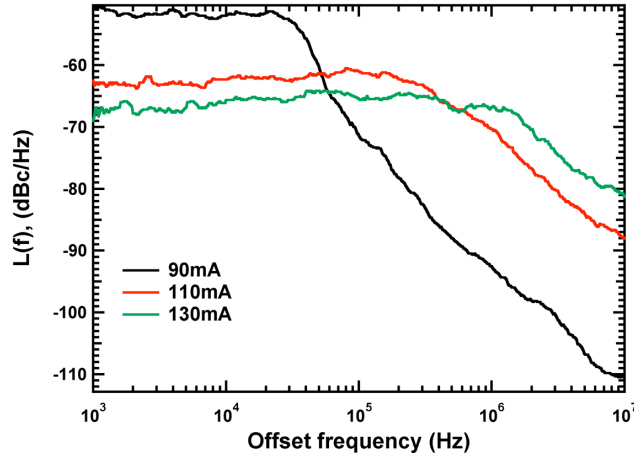


Fig. 6. SSB-PN spectra density at the 3<sup>rd</sup> harmonic under 90, 110, and 130 mA gain current and -7 V reverse voltage.

#### 4. Conclusion

To the best of our knowledge, this is the first time that the relationships between the timing jitter, RF linewidth, and SSB-PN corner frequency and white-noise plateau in a monolithic passive QD MLL have been discussed. A state-of-the-art timing jitter value of 211 fs (4 MHz to 80 MHz) for a 5 GHz passive QD MLL has been reported. The best jitter and lowest corner frequency was found just above the threshold current of the MLL and then typically the performance degraded with increasing current bias in the gain section at a fixed absorber voltage. In general this behavior mirrors the trend in the pulse quality, which has been reported previously [18]. The wide offset frequency span examined (1 kHz to 100 MHz) gives a better understanding of the noise performance at and below the corner frequency, which provides an alternative all-microwave method to obtain the pulse-to-pulse rms timing jitter. Further improvement of noise performance and corner frequency could be achieved under injection locking or external optical feedback.

## II. Microwave characterization and stabilization of timing jitter in a quantum dot passively mode-locked laser via external optical feedback

Chang-Yi Lin, *Student Member, IEEE*, Frédéric Grillot, *Member, IEEE*, Yan Li, *Member, IEEE*, Ravi Raghunathan, and Luke F. Lester, *Senior Member, IEEE*

**Abstract**— The pulse-to-pulse rms timing jitter of a 5.25 GHz quantum dot two-section passively mode-locked laser is characterized through an all-microwave technique. The experimental phase noise spectra at different harmonics are in good agreement with previous diffusion-based theory. This theory is validated for a quantum dot mode-locked laser device for the first time. This measurement technique provides a simple way to characterize the noise performance of a passively mode-locked laser. Furthermore, the average pulse-to-pulse rms timing jitter reduces from 295 fs/cycle to 32 fs/cycle via external optical feedback.

**Index Terms**—Mode-locked lasers, optical feedback, semiconductor quantum dot lasers, timing jitter

### I. INTRODUCTION

The need for cost-effective, power-efficient, and low phase noise optical pulse sources has motivated recent research into semiconductor passively mode-locked laser (MLL) solutions for optical time division multiplexing (OTDM) applications applied to intra-chip and on-chip communications [1-3]. In these signal processing applications, optical pulses with short picosecond pulse durations and multi-gigahertz repetition rates are needed. Furthermore, a low pulse-to-pulse timing jitter is also required to prevent errors arising from the ambiguity between successive neighboring pulses. In order to meet these requirements, MLLs are promising candidates for generating stable short optical pulses that have a corresponding broad spectral bandwidth consisting of phase-correlated modes. Of all the different MLL configurations, monolithic two-section passive MLLs offer several advantages including compact size, simple fabrication, DC bias only, and the ability for hybrid integration to silicon substrates. In addition, various unique characteristics of quantum dot (QD) materials, such as high gain saturation energy, reduced threshold current density, and low spontaneous emission noise, make them an ideal choice for semiconductor monolithic MLLs, especially for improved noise performance [4]. However, in contrast to active mode-locking, the timing stability issue is still a drawback of passive MLLs due to the lack of an external reference source.

The timing jitter performance of a passive MLL can be further improved through the optical injection-locking technique or external optical feedback [5-12]. In this work, we focus on the optical feedback method since it provides a compact and cost-effective fiber-based feedback arm compared to the optical injection-locking technique that requires an additional CW tunable laser source. In various potential applications, such as OTDM, performance of the MLL in an external optical cavity is an important feature, as the laser diode is likely to be monolithically integrated on chip with other devices, in which case optical isolation is difficult. Thus, MLLs

---

Manuscript received December 6, 2010. This work was supported by the Air Force Office of Scientific Research under Grant Nos. FA9550-10-1-0276 and FA9550-09-1-0490.

C.-Y. Lin, Y. Li, R. Raghunathan, and L. F. Lester are with Center for High Technology Materials, University of New Mexico, Albuquerque, NM 87106 USA (e-mail: cylin@unm.edu; yanli@chtm.unm.edu; raghunat@unm.edu; luke@chtm.unm.edu).

F. Grillot is with Université Européenne de Bretagne, CNRS FOTON, Institut National des Sciences Appliquées, 20, Avenue des buttes de Coesmes, 35043 Rennes Cedex, France, (email: frederic.Grillot@insa-rennes.fr).

F. Grillot is also with Institut Telecom/Telecom ParisTech, CNRS LTCI, 46 rue Barrault, 75634 Paris Cedex, France, (frederic.grillot@telecom-paristech.fr)

may be subjected to optical feedback generated by discrete reflections. These perturbations may be induced by discontinuities in the optical waveguide of the monolithic chip or at the device-package interfaces from other optical devices placed along an optical fiber. The sensitivity of quantum well (QW) MLLs under optical feedback has been evaluated experimentally by several groups [5,6]. On one hand, resonant reduction of noise for external cavity lengths that are a multiple of the laser's optical length was observed [5]. On the other hand, by using monolithic colliding-pulse passive QW MLLs, Passerini et al. have shown that optical feedback negatively affects the phase-locking relation between the longitudinal modes [6]. Recently, the sensitivity and noise performance of QD MLLs under optical feedback have also attracted numerous theoretical and experimental studies [8-13]. The reduced RF linewidth and timing jitters have been obtained under the resonant feedback case. Meanwhile, a numerical investigation also demonstrated the influence of optical feedback on the dynamics and spectra of monolithic MLLs [13]. A wide variety of dynamic regimes were numerically simulated taking into account the length of the external cavity in the MLL dynamics.

After introducing the methods to improve the noise performance, it is crucial that the jitter characterization in a passive MLL be studied more thoroughly. Since the timing-jitter fluctuations in a passive MLL constitute a nonstationary process, the phase noise does not scale with harmonic number [14]. Thus, the commonly-used model for calculating the integrated rms jitter proposed by von der Linde [15], which assumes a stationary process only, is not suitable for a passive MLL unless the offset frequency is above the corner frequency. For the pulse-to-pulse timing jitter calculation, we present an alternative all-microwave technique based on previously published theory [14] and compare this different RF measurement approach to the work reported by Kefelian et al. [16].

The paper is organized as follows. Device structure and fabrication process are introduced in section II. The basic optical characterization in the free-running case is also presented. Section III is devoted to the introduction of noise performance characterization in a passive MLL, including the integrated root mean square (rms) timing jitter and the pulse-to-pulse rms timing jitter,  $\sigma_{pp}$ . Following that, we experimentally characterize  $\sigma_{pp}$  using the analytical model by Eliyahu *et al.* [14] and make comparisons with prior research. Timing jitter reduction is achieved by using a controlled external feedback arm to stabilize the QD MLL. The jitter value reduces from 295 fs/cycle to 32 fs/cycle under external optical feedback. Finally, the key findings of the paper are summarized in Section V.

## II. Device Structure and fabrication

The laser epitaxial structure of the MLL device is a multi-stack "Dots-in-a-WELL" (DWELL) structure that is composed of an optimized six-stack InAs QD active region grown by elemental source molecular beam epitaxy (MBE) on an n+-doped, <100>-oriented GaAs substrate [17]. The epitaxial structure and waveguide design are described in Fig. 1. The 3- $\mu$ m-wide ridge-waveguide devices were formed by inductively coupled plasma (ICP) etching and planarized using benzocyclobutene (BCB). Ti/Pt/Au was then deposited to form the p-type metal contact. The electrical isolation between the gain and absorber sections was achieved by ion implantation with an isolation resistance of >10 M $\Omega$ . After the substrate had been thinned and polished, a Ge/Au/Ni/Au n-metal contact was deposited on the backside of the n+-GaAs substrate and annealed at ~380°C for 1 minute to form the ohmic contact. The two-section passive QD MLLs were cleaved with a total cavity length of 7.8-mm and a saturable absorber (SA) length of 1.1-mm, corresponding to a pulse repetition rate of 5.25 GHz. A highly reflective coating ( $R \approx 95\%$ ) was applied to the mirror facet next to the SA to create self-colliding pulse effects in the SA for pulse narrowing, and the output facet was cleaved ( $R \approx 32\%$ ). The devices were p-side-up mounted on AlN heatsink carriers. These chip-on-carriers were then packaged into an industry-standard 14-pin butterfly package with a thermoelectric cooler (TEC) and a polarization-maintaining lensed fiber pigtail. The function of the packaged module is to reduce environmental noise and enhance mechanical stability.

Fig. 2 shows the fiber-coupled light-current (L-I) curve under various reverse voltage bias conditions at 20°C. The inset is the optical spectrum showing the peak lasing wavelength at 1313 nm under a gain current of 100 mA and an SA reverse voltage of -7 V. The typical average powers emitted by these devices under mode-locking conditions at the end of the fiber pigtail are 1-2.5 mW. The pulse durations shown in Fig. 3 are typically about 10 ps and were measured by a Tektronix DSA 8200 oscilloscope with a 140 GHz optical sampling head. The resolution of the oscilloscope is limited by the bandwidth of the optical sampling head. In our experimental setup, the minimum measurable pulse duration is around 8 ps. Fig. 4(a) demonstrates the full-span RF spectrum with 9 detected harmonics under a 90 mA DC bias on the gain section and -7 V applied to the absorber. The optimum 3-dB RF linewidth of the free-running laser at the fundamental harmonic shown in Fig. 4(b) is 46.2 kHz at the same bias condition. The RF linewidth is confirmed with a Lorentzian curve fit on the RF spectrum

analyzer (RFSA) output with a resolution bandwidth of 1 kHz.

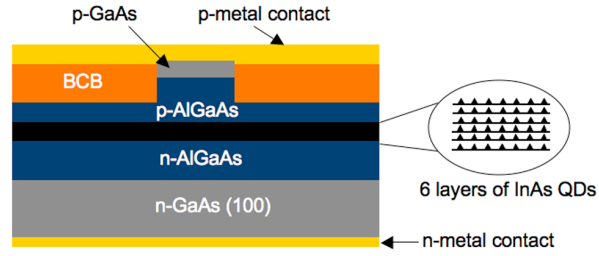


Fig. 1. Schematic of the epitaxial layer structure of the InAs QD laser.

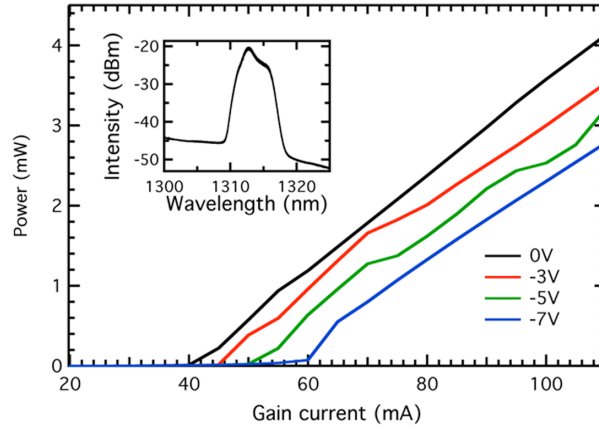


Fig. 2. Light current characteristics measured at 20°C under various absorber bias voltages. The figure in the inset shows the optical spectrum under 280-mA gain current and -1 V reverse voltage.

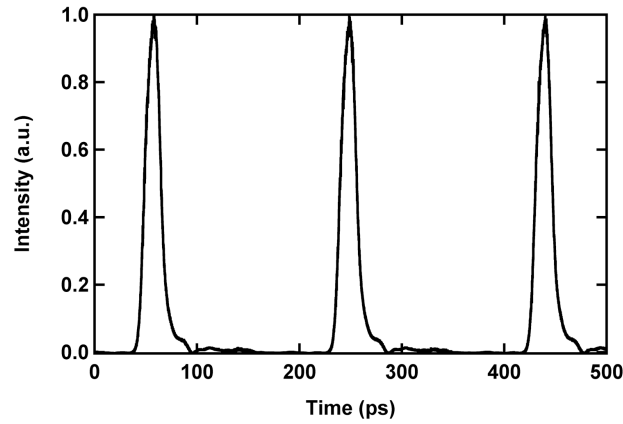


Fig. 3. Pulsewidth of 10.9-ps under 75-mA gain current and -7 V reverse voltage through high speed sampling oscilloscope measurement.



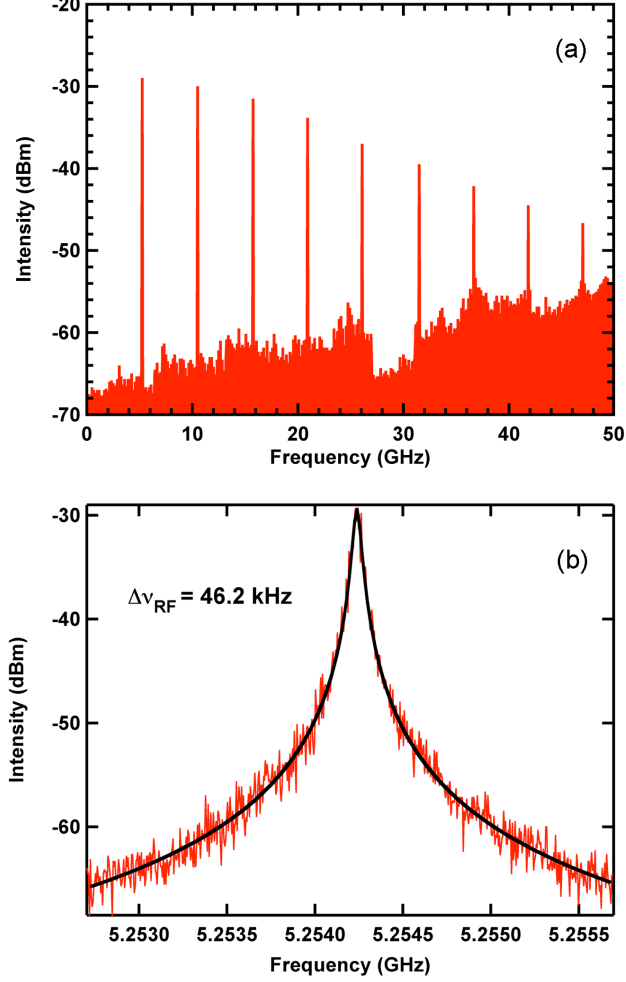


Fig. 4. RF spectrum under 100 mA gain current and -7 V reverse voltage. (a) the full-span condition. (b) 3-dB RF linewidth of 46.2 kHz.

### III. Noise Performance Characterization Integrated rms Timing Jitter Characterization

Conventionally, the noise characterization of an MLL by von der Linde's method uses timing jitter as the figure-of-merit [15]. In particular, the rms timing jitter is calculated by integrating the single-sideband phase noise (SSB-PN) spectral density,  $L(f)$ , from an RFSA using the following expression.

$$\sigma = \frac{1}{2\pi n f_R} \sqrt{2 \int_{f_{\min}}^{f_{\max}} L(f) df} \quad (1)$$

where  $n$  is the number of the harmonic at which the phase noise is measured,  $f_R$  is the repetition frequency, and  $f_{\min}$  and  $f_{\max}$  determine the offset frequency range over which the  $L(f)$  is integrated. Fig. 5(a) displays the SSB-PN spectral density for different harmonics of the 5.25 GHz passive QD MLL device in the free-running case. The relatively low repetition rate of this monolithic passive MLL makes the characterization of a relatively large number of harmonics possible in a standard 50 GHz RFSA.

However, although this technique is suitable for noise characterization in an active MLL that naturally has an

external reference source, it should be applied carefully to a passive MLL. Since the timing-jitter fluctuation in a passively mode-locked laser is a *nonstationary* process, the phase noise does not scale with harmonic number until beyond the corner frequency as clearly seen in Fig. 5(b) [14]. Consequently, it is only appropriate to use the von der Linde's method for offset frequencies above the corner frequency where the phase noise trace shows the typical roll-off with a slope of  $-20$  dBc/Hz per decade. From the phase noise data in Fig. 5(b), we see that a meaningful lower bound to the integration range would be about 1-2 MHz for this particular device.

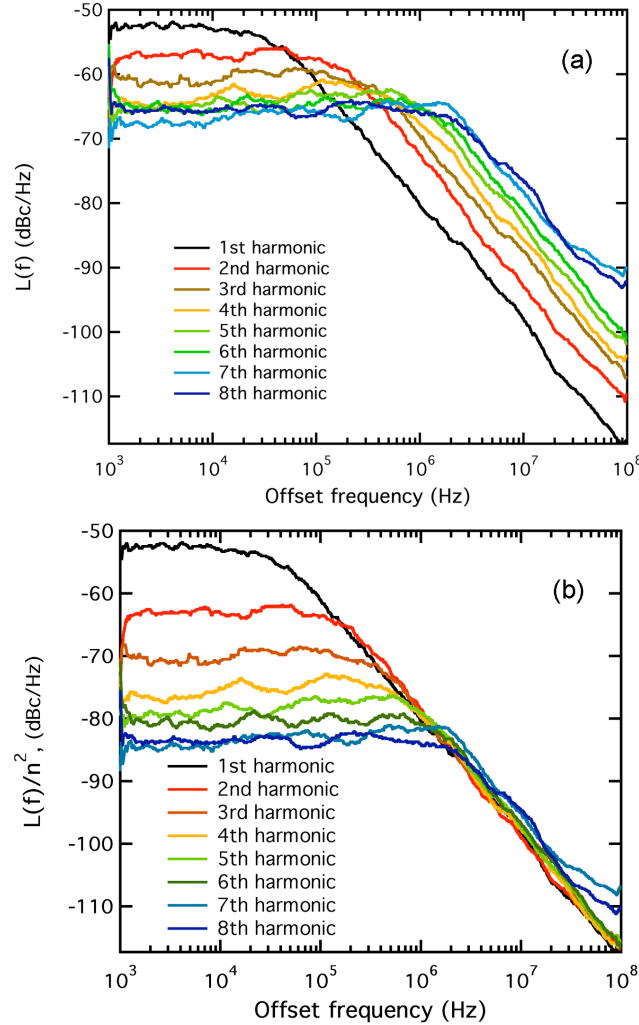


Fig. 5 (a) SSB-PN spectral density for different harmonics under 100 mA gain current and  $-7$  V reverse voltage in the free-running case. (b) SSB-PN spectra density normalized to  $1/n^2$

### Pulse-to-Pulse rms Timing Jitter Characterization

Past research has quoted the integrated rms timing jitter over a variety of different frequency ranges, which can be confusing for comparing devices. Because of the intrinsic phase noise properties of a passive MLL [14,18], it is more straightforward to investigate the noise performance based on the pulse-to-pulse timing fluctuations since the integration range does not have to be specified. The relevant theory for determining the pulse-to-pulse jitter is described next.

Due to the absence of a restoring external force, the timing of each pulse in a passive MLL depends on that of

the previous one, and its fluctuation results from the sum of many assumed independent processes. Thus, the timing-jitter noise can be described by diffusion theory for Gaussian processes whenever fluctuations of timing jitter between successive neighboring pulses are uncorrelated. An analytical model has been derived by Eliyahu *et al.* [14], and the power spectrum in a passive MLL is expressed as the following equation:

$$P_l(\omega) = |F(\omega)|^2 \frac{\sinh(\omega^2 DT / 2)}{\cosh(\omega^2 DT / 2) - \cos(\omega T)} \quad (2)$$

where  $F(\omega)$  is the amplitude term of the pulse,  $\omega$  is the frequency,  $T$  is the pulse repetition period, and  $D$  is the diffusion constant which can be described as:

$$D = \langle (\delta T_n - \delta T_{n \pm 1})^2 \rangle / T \quad (3)$$

Equation (3) represents the timing-jitter fluctuations between successive neighboring pulses and can be rearranged to find the pulse-to-pulse rms timing jitter,  $\sigma_{pp}$ :

$$\sigma_{pp} = \sqrt{DT} \quad (4)$$

The analytical model above provides an appropriate method to characterize the noise performance in a passive MLL that obeys a nonstationary process. Thanks to the relatively low repetition rate of our QD MLL device, there are more harmonics available experimentally to examine this analytical model and to extract the average  $D$  and  $\sigma_{pp}$  values through curve fitting [19]. Table I lists the fitting results that were extracted from the experimental data shown in Fig. 5(a). The experimental results are in good agreement with the analytical model. In the free-running case, an average  $D$  of  $4.59 \cdot 10^{-16}$  (sec) and an average  $\sigma_{pp}$  of 295 (fs/cycle) were obtained with the pulse period  $T$  equal to 190 ps.

Following the same assumption of the noise properties in a semiconductor passive MLL [18], another analytical derivation presented by Kefelian *et al.* [16] explores the RF linewidth of the first harmonic of the photocurrent to characterize the timing stability of a passive MLL. In this approach, the pulse-to-pulse rms timing jitter can be described as follows:

$$\sigma_{pp-K} = T \sqrt{\frac{\Delta \nu_{RF} NT}{2\pi}} \quad (6)$$

where  $\Delta \nu_{RF}$  is the 3-dB RF linewidth and  $N$  is the number of periods between the two compared pulses. According to (6), using the optimum 3-dB RF linewidth of the free-running QD MLL at the fundamental harmonic, 46.2 kHz, corresponds to a pulse-to-pulse rms timing jitter of 225 fs/cycle. This model provides a way to characterize the noise performance in a passive MLL, especially for those devices with a high repetition rate, where it is difficult to measure the SSB-PN spectral density at higher-order harmonics. From our experimental pulse-to-pulse timing jitter calculations, the analytical models of Eliyahu and Kefelian agree with each other reasonably well. Both methods are based on the assumption that the passive MLL operates under the nonstationary process. In Kefelian's method, the RF linewidth is a figure-of-merit to characterize the pulse-to-pulse timing jitter performance while Eliyahu's model can obtain a measured pulse-to-pulse rms timing jitter value from the SSB-PN spectral density.

TABLE I  
TIMING JITTER CHARACTERIZATION IN THE FREE-RUNNING CASE

Harmonic #	D (sec)	$\sigma_{pp}$ (fs/cycle)
1	$4.01 \cdot 10^{-16}$	276
2	$4.01 \cdot 10^{-16}$	276
3	$4.50 \cdot 10^{-16}$	292
4	$4.98 \cdot 10^{-16}$	307
5	$5.14 \cdot 10^{-16}$	312
6	$4.87 \cdot 10^{-16}$	304
7	$4.56 \cdot 10^{-16}$	294
8	$4.67 \cdot 10^{-16}$	298

#### IV. Optical Feedback Stabilization

For further noise performance improvement, external optical feedback can be implemented to lower the phase noise in a passive MLL. This method provides a simple, compact, and cost-effective fiber-based loop compared to the injection locking technique which needs an external CW tunable laser. Under the resonant case (i.e stably-resonant feedback condition) [13], which is obtained when the optical length of the external cavity is about a multiple of that of the solitary laser, an RF linewidth and timing jitter reduction can be expected while the non-resonant case (i.e nearly-exact resonant case) usually leads to a degradation of the mode-locking conditions. Consequently, in the following only the resonant case is considered for the jitter optimization.

##### External Optical Feedback Experimental Setup

The passive QD MLL butterfly package with TEC was investigated under external optical feedback using the experimental setup shown in Fig. 6(a). All measurements were operated with the TEC at 20°C. The emitted light is injected into port 1 of a 50/50 optical fiber coupler. The optical feedback is created from a high-reflectivity ( $R > 95\%$ ) coating applied to the fiber tip at the end of port 2. The feedback power level is controlled via a variable optical attenuator (VOA), and its value is measured by the power meter in port 4. An optical delay line (ODL) that has a step-controlled fine delay stage (resolution: 0.1-mm) is introduced to change the external fiber loop length. In order to maximize the feedback effect, a polarization controller (PC) is used to make the feedback beam polarization identical to that of the emitted wave. The effect of the optical feedback is analyzed in port 3 through a 45 GHz bandwidth photodiode coupled to the RFSA. An optical isolator is used to prevent any unwanted reflection from the RFSA. Fig. 6(b) shows a photograph of the experimental setup including an external enclosure that helps to reduce the environmental noise during the measurement.

The value of the feedback strength is defined as the ratio  $\Gamma = P_l/P_0$  where  $P_l$  is the power returned to the facet and  $P_0$  the emitted value. The amount of the reflected light that effectively returns into the laser can then be expressed as follows:

$$\Gamma(\text{dB}) = P_r(\text{dBm}) - P_0 + C_{dB} \quad (5)$$

where  $P_r$  is the optical power measured from the power meter at port 4,  $C_{dB}$  is the optical coupling loss of the device to the fiber which was estimated to be about -5dB and kept constant during the whole measurement. In this work, the feedback experiment is studied under the long external cavity condition that assumes that  $f_r\tau \gg 1$ , where  $f_r$  is the relaxation frequency (a few GHz) and  $\tau$  is the external round trip time of several hundred nanoseconds. The total fiber length of the feedback arm is approximately 18 meters.

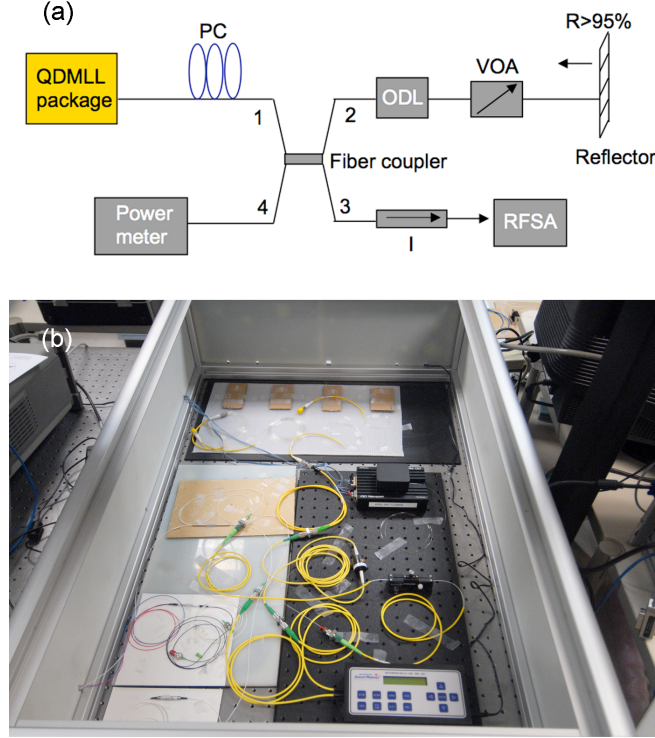


Fig. 6. (a) Schematic drawing of the feedback experimental setup. PC: polarization controller; ODL: optical delay line; VOA: variable optical attenuator; I: isolator; RFSA: RF spectrum analyzer. (b) Photograph of feedback experiment setup within a vibration- and RF-isolated enclosure.

## Experimental Results and Discussion

Under the optimum feedback condition ( $\Gamma = -33$  dB), the RF linewidth was reduced from 46 kHz to 1.1 kHz as shown in Fig. 7, while simultaneously introducing a comb of adjacent modes separated by 5.7 MHz as shown in the inset. Most importantly, as seen from eqn. (6), the reduction of RF linewidth decreases the pulse-to-pulse rms timing jitter. Thus, the 42-fold RF linewidth reduction under optical feedback should decrease  $\sigma_{pp}$  by a factor of  $\sim 6.5$ . Using (6), the RF linewidth under the optimum feedback case, 1.1 kHz, corresponds to a pulse-to-pulse timing jitter of 35 (fs/cycle). This result can be compared to the Eliyahu model calculations using the same approach as for the free-running analysis.

After the RF linewidth characterization, the SSB-PN spectral density at different harmonics was measured under external feedback effect as shown in Fig. 8. Due to the limited dynamic range of the phase noise measurement under feedback, the SSB-PN spectrum at the 5<sup>th</sup> harmonic is the maximum number that can be evaluated in this measurement. Compared to fig. 5(a), optical feedback impacts the SSB-PN spectra by decreasing the corner frequency from 2MHz to about 10kHz while enhancing plateau levels. The explanation of the influence of optical feedback on both the plateau and on the corner frequency is still under investigation and will be discussed in another paper. With the same approach mentioned in section III-B, we can extract the values of the diffusion constant,  $D$ , and the pulse-to-pulse timing jitter,  $\sigma_{pp}$ , at different harmonics under optical feedback. Table II shows the fitting results that were extracted from the experimental data shown in Fig. 8. In the external optical feedback case, an average  $D$  of  $5.53 \cdot 10^{-18}$  (sec) and an average  $\sigma_{pp}$  of 32 (fs/cycle) are obtained. Again, this jitter value agrees well with the one derived from (6).

Conventionally, the rms pulse-to-pulse timing jitter can be measured directly by optical cross-correlation using the second harmonic generation in a nonlinear crystal. However, this measurement needs a particular nonlinear crystal, precise mountings, stable optical alignment, accurate temperature control, and long mechanical scanning. Furthermore, when the timing fluctuation is much smaller than the autocorrelation width, the measurement error becomes very large [20-23]. Compared to the optical cross-correlation method, the all-microwave technique based on Eliyahu's theory provides a simpler way to characterize the average pulse-to-

pulse timing jitter thanks to the family of phase noise spectra at different harmonics.

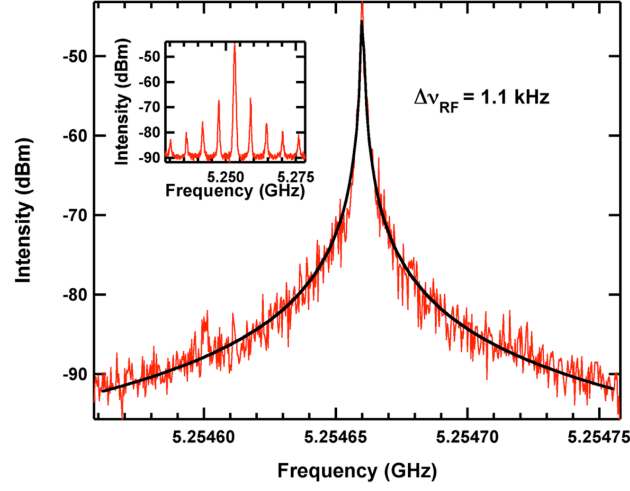


Fig. 7. RF linewidth of 1.1 kHz under optimum feedback condition ( $\Gamma = -33$  dB). Inset: RF spectrum with mode-comb separated by 5.7 MHz.

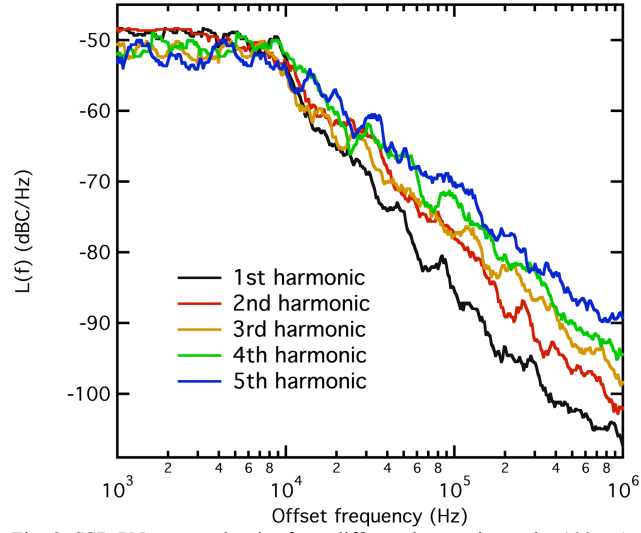


Fig. 8. SSB-PN spectra density from different harmonics under 100 mA gain current and  $-7$  V reverse voltage at the optimum feedback case.

TABLE II  
TIMING JITTER CHARACTERIZATION IN THE OPTICAL FEEDBACK CASE

Harmonic #	D (sec)	$\sigma_{pp}$ (fs/cycle)
1	$4.97 \cdot 10^{-18}$	30.8
2	$6.83 \cdot 10^{-18}$	36.1
3	$6.52 \cdot 10^{-18}$	35.2
4	$4.35 \cdot 10^{-18}$	28.8
5	$4.97 \cdot 10^{-18}$	30.8

## V. Conclusion

The timing jitter performance of a 5.25-GHz passive QD MLL was investigated at different harmonics in the RF spectrum. The relatively low repetition rate of the laser device enables SSB-PN spectra to be measured up to the 8<sup>th</sup> harmonic in the free-running configuration, and up to the 5<sup>th</sup> harmonic under feedback. An all-microwave technique has been used to determine the pulse-to-pulse rms timing jitter. Compared to the conventional optical cross-correlation technique, it provides an alternative and simple method to characterize the timing stability in a passive MLL. To the best of our knowledge, the previously published, diffusion-based model by Eliyahu *et al.* has been validated in the passive QD MLL device for the first time. The experimental findings also demonstrated a good agreement for both analytical approaches from Eliyahu *et al.* and Kefelian *et al.* [14, 16]. As measured by the Eliyahu model, the pulse-to-pulse timing jitter was reduced by nearly an order of magnitude through external optical feedback effect. Thus, the QD MLL packaged module with a simple implementation of an optical feedback arm offers an attractive method for OTDM intra-chip/on-chip communications.

## Acknowledgment

The authors thank Joaquin Gabaldon for designing the vibration- and RF-isolated enclosure in the feedback experiment.

## References

- [1] A. A. Aboketaf, A. W. Elshaari, and S. F. Preble, "Optical time division multiplexer on silicon chip," *Opt. Exp.*, vol. 18, pp. 13529–13535, Jun. 2010.
- [2] B. R. Koch, A. W. Fang, O. Cohen, and J. E. Bowers, "Mode-locked silicon evanescent lasers," *Opt. Exp.*, vol. 15, pp. 11225–11233, Aug. 2007.
- [3] F. Quinlan, S. Ozharar, S. Gee, and P. J. Delfyett, "Harmonically mode-locked semiconductor-based lasers as high repetition rate ultralow noise pulse train and optical frequency comb sources," *J. Opt. A: Pure Appl. Opt.*, vol. 11, no. 10, pp. 103001-1-103001-23, Apr. 2009.
- [4] M. G. Thompson, A. R. Rae, M. Xia, R. V.enty, and I. H. White, "InGaAs quantum-dot mode-locked laser diodes," *IEEE J. Sel. Top. Quantum Electron.*, vol. 15, no. 3, pp. 661–672, May 2009.
- [5] O. Solgaard, and K. Y. Lau, "Optical feedback stabilization of the intensity oscillations in ultrahigh-frequency passively modelocked monolithic quantum-well lasers," *IEEE Photon. Technol. Lett.*, vol. 5, no. 11, pp. 1264-1267, Nov. 1993.
- [6] M. Passerini, G. Giuliani, and M. Sorel, "Effect of Optical Feedback on 60-GHz Colliding-Pulse Semiconductor Mode-Locked Lasers," *IEEE Photon. Technol. Lett.*, vol. 17, no. 5, pp. 965-967, May 2005.
- [7] T. Habruseva, S. O'Donoghue, N. Rebrova, D. A. Reid, L. P. Barry, D. Rachinskii, G. Huyet, and S. P. Hegarty, "Quantum-Dot Mode-Locked Lasers With Dual-Mode Optical Injection," *IEEE Photon. Technol. Lett.*, vol. 22, no. 6, pp. 359–361, Mar. 2010.
- [8] F. Grillot, C.-Y. Lin, N. A. Naderi, M. Pochet, and L. F. Lester, "Optical feedback instabilities in a monolithic InAs/GaAs quantum dot passively mode-locked laser," *Appl. Phys. Lett.*, vol. 94, p. 153503, Apr. 2009.
- [9] C.-Y. Lin, F. Grillot, N. A. Naderi, Y. Li, and L. F. Lester, "rf linewidth reduction in a quantum dot passively mode-locked laser subject to external optical feedback," *Appl. Phys. Lett.*, vol. 96, p. 051118, Feb. 2010.
- [10] S. Breuer, W. Elsaer, J. G. McInerney, K. Yvind, J. Pozo, E. A. J. M. Bente, M. Yousefi, A. Villafranca, N. Vogiatzis, and J. Rorison, "Investigations of Repetition Rate Stability of a Mode-Locked Quantum Dot Semiconductor Laser in an Auxiliary Optical Fiber Cavity," *IEEE J. Quantum Electron.*, vol. 46, no. 2, pp. 150-157, Feb. 2010.
- [11] K. Merghem, R. Rosales, S. Azougui, A. Akrou, A. Martinez, F. Lelarge, G.-H. Duan, G. Aubin, and A. Ramdane, "Low noise performance of passively mode locked quantum-dash-based lasers under external optical feedback," *Appl. Phys. Lett.*, vol. 95, p. 131111, Sep. 2009.
- [12] C. Mesaritis, C. Simos, H. Simos, S. Mikroulis, I. Krestnikov, E. Roditi, and D. Syvridis, "Effect of optical feedback to the ground and excited state emission of a passively mode locked quantum dot laser," *Appl. Phys. Lett.*, vol. 97, p. 061114, Aug. 2010.
- [13] E. A. Avrutin, and B. M. Russell, "Dynamics and spectra of monolithic mode-locked laser diodes under external optical feedback," *IEEE J. Quantum Electron.*, vol. 45, no. 11, pp. 1456-1464, Nov. 2009.
- [14] D. Eliyahu, R. A. Salvatore, and A. Yariv, "Noise characterization of pulse train generated by actively mode-locked lasers," *J. Opt. Soc. Am. B*, vol. 13, no. 7, pp. 1619–1626, Jul. 1996.
- [15] D. von der Linde, "Characterization of the noise in continuously operating mode-locked lasers," *Appl. Phys. B*, vol. 39, pp. 201–217, 1986.
- [16] F. Kefelian, S. O'Donoghue, M. T. Todaro, J. G. McInerney, and G. Huyet, "RF linewidth in monolithic passively mode-locked semiconductor laser," *IEEE Photon. Technol. Lett.*, vol. 20, no. 16, pp. 1405-1407, Aug. 2008.
- [17] Y.-C. Xin, Y. Li, A. Martinez, T. J. Rotter, H. Su, L. Zhang, A. L. Gray, S. Luong, K. Sun, Z. Zou, J. Zilko, P. M. Varangis, and L. F. Lester, "Optical gain and absorption of quantum dots measured using an alternative segmented contact method," *IEEE J. Quantum Electron.*, vol. 42, no. 7, pp. 725–732, Jul. 2006.
- [18] H. A. Haus and A. Mecozzi, "Noise of mode-locked lasers," *IEEE J. Quantum Electron.*, vol. 29, no. 3, pp. 983–996, Mar. 1993.
- [19] C.-Y. Lin, F. Grillot, Y. Li, R. Raghunathan, and L. F. Lester, "Characterization of timing jitter in a 5 GHz quantum dot passively mode-locked laser," *Opt. Exp.*, vol. 18, pp. 21932–21937, Sep. 2010.
- [20] L. A. Jiang, M. E. Grein, H. A. Haus, and E. P. Ippen, "Noise of mode-locked semiconductor lasers," *IEEE J. Sel. Topics Quantum Electron.*, vol. 7, no. 2, pp. 159–167, Mar. 2001.
- [21] M. T. Todaro, J. P. Tourrenc, S. P. Hegarty, C. Kelleher, B. Corbett, G. Huyet, and J. G. McInerney, "Simultaneous achievement of narrow pulsewidth and low pulse-to-pulse timing jitter in 1.3  $\mu\text{m}$  passively mode-locked quantum-dot lasers," *Opt. Lett.*, vol. 31, no. 21, pp. 3107–3109, Nov. 2006.

- [22] J. P. Tourrenc, S. O'Donoghue, M. T. Todaro, S. P. Hegarty, M. B. Flynn, G. Huyet, J. G. McInerney, L. O'Faolain, and T. F. Krauss, "Cross-correlation timing jitter measurement of high power passively mode- locked two-section quantum-dot lasers," *IEEE Photon. Technol. Lett.*, vol. 18, no. 21, pp. 2317-2319, Nov. 2006.
- [23] J. P. Tourrenc, A. Akrou, K. Merghem, A. Martinez, F. Lelarge, A. Shen, G. H. Duan, and A. Ramdane, "Experimental investigation of the timing jitter in self-pulsating quantum-dash lasers operating at 1.55  $\mu\text{m}$ ," *Opt. Exp.*, vol. 16, no. 22, pp. 17706–17713, Oct. 2008.